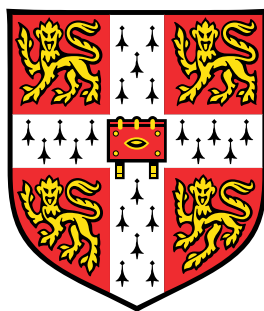# A Unified Framework for Simulating Impact-Induced Detonation of a Combustible Material in an Elasto-Plastic Confiner

Haran Jackson

The Centre for Scientific Computing

University of Cambridge

This probationary review is submitted for the degree of

Doctor of Philosophy in Scientific Computing

Fitzwilliam College   Supervisor: Dr N. Nikiforakis

Contents

1 Acknowledgements

2 Background

2.1 Motivation

A common theme over the course of humanity's uncovering of the Laws of Physics has been the unification of mathematical descriptions of formerly apparently disparate physical phenomena (for example Maxwell's equations in unifying the theories of electromagnetism and optics, or the proposed Grand Unified Theories of the electromagnetic, weak, and strong interactions of the Standard Model). Computational Continuum Mechanics is yet to see ubiquitous adoption of such a unified framework, with separate models used to describe the various states of matter. These models differ not just in terms of the first principles descriptions they posit for the materials that they purport to describe, but also in their mathematical characteristics. For example, the viscous stress terms in the Navier Stokes equations are empirically derived, and the resulting system is parabolic in nature. By contrast, the Godunov Romenski equations of elasto plastic deformation of metals are based on a first principles description of the microscopic material elements of the continuum, and the model is hyperbolic in nature.

Unified models are not just aesthetically pleasing, but also practically useful. The conceptual work required to implement a computational simulation involving many different components is greatly reduced, saving time and allowing for greater specialization of computational techniques.

2.2 Literature Review

The definition of a multiphase system is slightly ambiguous in the literature. Here it will be taken to mean a system consisting of either two or more different materials (possibly in the same phase of matter), or two or more volumes of (possibly the same) material in different phases of matter. There are two aspects of multiphase systems that require attention: multiphase flow, and multiphase heat transfer. The latter becomes important when the phases are at different temperatures. In this study, the different phases will be assumed to be immiscible.

Without a unified model of continuum mechanics, capable of describing all phases in the same framework, different sets of equations may have to be used in the different regions occupied by different phases. These systems arise, for example, in fluid structure interaction, or oil water interfaces. An overview of current approaches to multiphase systems will now be given. The examples here are illustrative but not exhaustive.

There has been a huge amount of research activity in the field over the years, but current approaches can be broadly classified as either monolithic or partitioned [45]. In a monolithic scheme, all phases are described by the same set of nonlinear equations. The evolution of the interfaces is implicit to the equations, unlike in partitioned schemes. See for example [64, 46]. The system is solved by a multivariate Newton type method. It is often ill conditioned, due to the different scales of the state variables of the different phases. Thus, iterative solvers are required, proving inefficient unless good preconditioners are available. Codes tend to be very specialized to the specific problems they solve, and it requires expertise to develop and maintain such methods.

In a partitioned scheme, the states of the different phases are calculated separately at each time step, possibly using different models. See Rossi and Oñate [74] for a recent overview of some of the common algorithmic features of these schemes. The individual systems do not suffer from the scaling induced conditioning prob lems of monolithic schemes, but attention now needs to be payed to the material interfaces. Modeling them can be unstable and relatively computationally expensive (although typically not as expensive as solving the full monolithic systems). One of the great benefits of partitioned schemes is that legacy implementations of common models may be used in the domains occupied by materials that they describe. These implementa tions are often well used and relatively bug free, and tend to be written efficiently for the kinds of problems that the solve. As an example of a software suite taking advantage of this, see the Caltech's Virtual Test Facility [2].

Under both types of schemes, the models describing the different phases may be formulated in either a Lagrangian, an Eulerian, or an ALE framework. Solids models tend to come in Lagrangian form, and often these are combined with ALE forms for the fluid phases, so that the fluid meshes may deform to match the deformation of the solid (see, for example, Pin et al. [69]). These schemes tend to be very accurate, but like all Lagrangian schemes, they fail if the meshes become highly contorted. Thus, adaptive remeshing is often necessary. Some authors have coupled a Lagrangian solid scheme with an Eulerian fluid scheme, but extra care must be taken when applying the boundary conditions to the interface, which corresponds to the intersection of the Eulerian and Lagrangian meshes (see Legay et al. [56] for an implementation using level sets, or Fedkiw [35] for a GFM coupling). Some authors, such as Ryzhakov et al. [75], have found success in using the common Lagrangian formulations for the solid, and a reformulated Lagrangian model for the fluid, implementing the necessary adaptive remeshing. Yet another option is to model both the fluid and the solid in an Eulerian framework, although this now necessitates a level set method or volume of fluid method [44] to track the interfaces. Also, these methods are more prone to losing small scale geometric features of the media, unless methods such as AMR are employed to combat this [45].

In a recently submitted paper, Michael and Nikiforakis [63] (building on the work of Schoch et al. [77]) couple various Eulerian models of reactive and inert fluids and solids by use of a Riemann Ghost Fluid Method, with the ghost states calculated using specialised mixed material Riemann solvers for each interaction (see Section 4.1.1). Whilst these techniques do not suffer from the mesh contortion issues inherent in Lagrangian formulations of continuum mechanics, and the interface coupling tends to be less computationally expensive than the iterative techniques demanded by monolithic schemes, a fair amount of theoretical work needs to be done to derive analytical relations describing the interactions between every pair of models used.

If it were possible to describe all phases with the same Eulerian model, this method could be used, with only one type of Riemann solver needed to cope with any multiphase problem posed. This would effectively

be a partitioned scheme with the same system solved in each domain. The GPR model represents such an opportunity. As will be seen, the model also includes terms for heat conduction, which do not appear in the basic formulations of many of the common models used in multiphase systems (e.g. the Euler equations, or the Navier Stokes equations). Heat conduction is often ignored in multiphase modeling, but such a framework based on the GPR model would almost unavoidably include it. It should be noted, though, that any unified model of continuum mechanics purporting to describe all phases of interest must be at least as descriptive as competing models tailored to each individual phase if the utmost model fidelity is required. Although the results for the GPR model applied to standard test cases have been promising, both here and in other preliminary studies [27, 11], more work is required to determine how faithfully the GPR model reproduces common agreed phenomenological results.

The Godunov Peshkov Romenski (GPR) model, proposed in 2014 by Ilya Peshkov and Eugeny Romenski, purports to describe both fluids and solids in the same mathematical framework. It is described in 2.3. Thus far, the GPR model has been solved with the ADER WENO method, as described in 2.4.

2.3   The GPR Model

The GPR model, first introduced in [68], has its roots in Godunov and Romenski's 1970s model of elasto plastic deformation (see [40]). It was expanded upon in [27] to include thermal conduction. This expanded model takes the following form:

$$\frac{\partial \rho}{\partial t} + \frac{\partial \left(\rho v_k\right)}{\partial x_k} = 0 \tag{1a}$$

$$\frac{\partial \left(\rho v_i\right)}{\partial t} + \frac{\partial (\rho v_i v_k + p\delta_{ik} - \sigma_{ik})}{\partial x_k} = 0 \tag{1b}$$

$$\frac{\partial A_{ij}}{\partial t} + \frac{\partial \left(A_{ik} v_k\right)}{\partial x_j} + v_k \left(\frac{\partial A_{ij}}{\partial x_k} - \frac{\partial A_{ik}}{\partial x_j}\right) = -\frac{\psi_{ij}}{\theta_1(\tau_1)} \tag{1c}$$

$$\frac{\partial \left(\rho J_i\right)}{\partial t} + \frac{\partial \left(\rho J_i v_k + T\delta_{ik}\right)}{\partial x_k} = -\frac{\rho H_i}{\theta_2\left(\tau_2\right)} \tag{1d}$$

$$\frac{\partial \left(\rho E\right)}{\partial t} + \frac{\partial \left(\rho E v_k + \left(p\delta_{ik} - \sigma_{ik}\right) v_i + q_k\right)}{\partial x_k} = 0 \tag{1e}$$

ρ,$\mathbf{v}$,p,δ,σ,T,E,$\boldsymbol{q}$ retain their usual meanings. θ_1 and θ_2 are positive scalar functions, chosen according to the properties of the material being modeled. A is the distortion tensor (containing information about the deformation and rotation of material elements), $\mathbf{J}$ is the thermal impulse vector (a thermal analogue of momentum), τ_1 is the strain dissipation time, and τ_2 is the thermal impulse relaxation time. $\psi = \frac{\partial E}{\partial A}$ and $\boldsymbol{H} = \frac{\partial E}{\partial \boldsymbol{J}}$.

The following definitions are given:

$$p = \rho^2 \frac{\partial E}{\partial \rho} \tag{2a}$$

$$\sigma = -\rho A^T \frac{\partial E}{\partial A} \tag{2b}$$

$$T = \frac{\partial E}{\partial s} \tag{2c}$$

$$\boldsymbol{q} = \frac{\partial E}{\partial s} \frac{\partial E}{\partial \boldsymbol{J}} \tag{2d}$$

To close the system, the equation of state (EOS) must be specified, from which the above quantities and the sources can be derived. E is the sum of the contributions of the energies at the molecular scale (microscale), the material element[1] scale (mesoscale), and the flow scale (macroscale):

$$E = E_1 \left(\rho, p \right) + E_2 \left(A, \boldsymbol{J} \right) + E_3 \left(\boldsymbol{v} \right) \tag{3}$$

The EOS used in this study (and described in the following passages) is taken from [27]. It should be noted, however, that this is just one particular choice, and there are many others that may be used.

For an ideal or stiffened gas, E_1 is given by:

$$E_1 = \frac{p + \gamma p_\infty}{\left(\gamma - 1 \right) \rho} \tag{4}$$

where $p_\infty = 0$ for an ideal gas.

E_2 is chosen to have the following quadratic form:

$$E_2 = \frac{c_s^2}{4} \left\| \text{dev} \left(G \right) \right\|_F^2 + \frac{\alpha^2}{2} \left\| \boldsymbol{J} \right\|^2 \tag{5}$$

c_s is the characteristic velocity of propagation of transverse perturbations. α is a constant related to the characteristic velocity of propagation of heat waves:

$$c_h = \frac{\alpha}{\rho} \sqrt{\frac{T}{c_v}} \tag{6}$$

$G = A^T A$ is the Gramian matrix of the distortion tensor, and $\text{dev} \left(G \right)$ is the deviator (trace free part) of G:

$$\text{dev} \left(G \right) = G - \frac{1}{3} \text{tr} \left(G \right) I \tag{7}$$

---

[1]The concept of a *material element* corresponds to that of a fluid parcel from fluid dynamics, applied to both fluids and solids.

E_3 is the usual specific kinetic energy per unit mass:

$$E_3 = \frac{1}{2} \left\| \boldsymbol{v} \right\|^2 \tag{8}$$

The following forms are chosen:

$$\theta_1 \left(\tau_1 \right) = \frac{\tau_1 c_s^2}{3 \left| A \right|^{\frac{5}{3}}} \tag{9a}$$

$$\theta_2 \left(\tau_2 \right) = \tau_2 \alpha^2 \frac{\rho T_0}{\rho_0 T} \tag{9b}$$

$$\tau_1 = \frac{6\mu}{\rho_0 c_s^2} \tag{10a}$$

$$\tau_2 = \frac{\rho_0 \kappa}{T_0 \alpha^2} \tag{10b}$$

The justification of these choices is that classical Navier–Stokes–Fourier theory is recovered in the stiff limit $\tau_1, \tau_2 \to 0$ (see [27]). This results in the following relations:

$$\sigma = -\rho c_s^2 G \operatorname{dev} \left(G \right) \tag{11a}$$

$$\boldsymbol{q} = \alpha^2 T \boldsymbol{J} \tag{11b}$$

$$-\frac{\psi}{\theta_1 \left(\tau_1 \right)} = -\frac{3}{\tau_1} \left| A \right|^{\frac{5}{3}} A \operatorname{dev} \left(G \right) \tag{11c}$$

$$-\frac{\rho \boldsymbol{H}}{\theta_2 \left(\tau_2 \right)} = -\frac{T \rho_0}{T_0 \tau_2} \boldsymbol{J} \tag{11d}$$

The following constraint also holds (see [68]):

$$\det \left(A \right) = \frac{\rho}{\rho_0} \tag{12}$$

The GPR model and Godunov and Romenski's 1970s model of elastoplastic deformation in fact relie upon the same equations. The realization of Peshkov and Romenski was that these are the equations of motion for an arbitrary continuum   not just a solid   and so the model can be applied to fluids too. Unlike in previous continuum models, material elements have not only finite size, but also internal structure, encoded in the distortion tensor.

The strain dissipation time τ_1 of the GPR model is a continuous analogue of Frenkel's "particle settled life time" [36]; the characteristic time taken for a particle to move by a distance of the same order of magnitude

as the particle's size. Thus, τ_1 characterizes the time taken for a material element to rearrange with its neighbors. $\tau_1 = \infty$ for solids and $\tau_1 = 0$ for inviscid fluids. It is in this way that the GPR model seeks to describe all three major phases of matter, as long as a continuum description is appropriate for the material at hand.

The evolution equation for $\boldsymbol{J}$ and its contribution to the energy of the system are derived from Romenski's model of hyperbolic heat transfer, originally proposed in [60, 73], and implemented in [72, 71]. In this model, $\boldsymbol{J}$ is effectively defined as the variable conjugate to the entropy flux, in the sense that the latter is the derivative of the specific internal energy with respect to $\boldsymbol{J}$. Romenski remarks that it is more convenient to evolve $\boldsymbol{J}$ and E than the heat flux or the entropy flux, and thus the equations take the form given here. τ_2 characterizes the speed of relaxation of the thermal impulse due to heat exchange between material elements.

2.4   The ADER-WENO Method

The GPR model, being non conservative, with stiff source terms, represents a particularly challenging set of PDEs. In this study they are solved by an ADER WENO method. First, the cell wise constant state variable data from the current time step is reconstructed using high order spatial polynomials according to the WENO method. This reconstruction is then extended to a reconstruction in both space and time for each individual cell in the domain, using the Discontinuous Galerkin method. A finite volume solver is then used to couple neighbouring cells and produce the cell wise constant data at the next time step. In this study, all simulations were performed in 1D. The methods presented here are easily extensible to higher dimensions, however.

Although this process has been demonstrated to be effective in solving the GPR system [26, 11], it was originally designed for problems involving moving meshes, and is probably more involved than necessary to perform the simulations in this study. The DG step in particular is relatively computationally taxing. The purpose of this study, however, was not to investigate more efficient solution methods for this particular system (see Sverdrup [80] for the latest work on this problem). It was therefore decided that this procedure would be used, being the only confirmed method of solution publicly available.

The WENO Reconstruction   First introduced by Liu et al. [59] and developed by Jiang and Shu [51], WENO methods are used to produce high order polynomial approximations to piece wise constant data. In this study, the modified method of Dumbser et al. [33] is used.

Consider the domain $[0, L]$. Take $K, N \in \mathbb{N}$. Take the set of grid points $x_i = \frac{i \cdot L}{K}$ for $i = 0, \dots, K$ and let $\Delta x = \frac{L}{K}$. Denote cell $[x_i, x_{i+1}]$ by C_i. Given cell wise constant data u on $[0, L]$, an order $N + 1$ accurate polynomial reconstruction of u in C_i will be performed. Define the scaled space variable:

$$\chi^i = \frac{1}{\Delta x} \left(x - x_i \right) \tag{13}$$

Denoting the Gauss Legendre abscissae on $[0, 1]$ by $\{\chi_0, \dots, \chi_N\}$, define the nodal basis of order N: the Lagrange interpolating polynomials $\{\psi_0, \dots, \psi_N\}$ with the following property:

$$\psi_i\left(\chi_j\right) = \delta_{ij} \tag{14}$$

If N is even, take the stencils:

$$\begin{cases} S_1 &= \left\{ C_{i-\frac{N}{2}}, \ldots, C_{i+\frac{N}{2}} \right\} \\ S_2 &= \{C_{i-N}, \ldots, C_i\} \\ S_3 &= \{C_i, \ldots, C_{i+N}\} \end{cases} \tag{15}$$

If N is odd, take the stencils:

$$\begin{cases} S_1 &= \left\{ C_{i-\left\lfloor\frac{N}{2}\right\rfloor}, \ldots, C_{i+\left\lceil\frac{N}{2}\right\rceil} \right\} \\ S_2 &= \left\{ C_{i-\left\lceil\frac{N}{2}\right\rceil}, \ldots, C_{i+\left\lfloor\frac{N}{2}\right\rfloor} \right\} \\ S_3 &= \{C_{i-N}, \ldots, C_i\} \\ S_4 &= \{C_i, \ldots, C_{i+N}\} \end{cases} \tag{16}$$

The data is reconstructed on S_j as:

$$\sum_p \psi_p\left(\chi^i\left(x\right)\right) \hat{w}_p^{ij} \tag{17}$$

where the $\hat{w}_p^{ij}$ are solutions to the following linear system:

$$\frac{1}{\Delta x} \int_{x_k}^{x_{k+1}} \psi_p\left(\chi^k\left(x\right)\right) \hat{w}_p^{ij} dx = u_k \qquad \forall C_k \in S_j \tag{18}$$

where u_k is the value of u in C_k. Define the oscillation indicator matrix:

$$\Sigma_{mn} = \sum_{\alpha=1}^N \int_0^1 \psi_m^{(\alpha)} \psi_n^{(\alpha)} d\chi \tag{19}$$

and the oscillation indicator for each stencil:

$$o_j = \Sigma_{mn} \hat{w}_m^{ij} \hat{w}_n^{ij} \tag{20}$$

The full reconstruction in C_i is:

$$w_i(x) = \sum_p \psi_p\left(\chi^i(x)\right)\hat{w}_p^i \tag{21}$$

where $\hat{w}_p^i = \omega_j \hat{w}_p^{ij}$ is the weighted coefficient of the pth basis function, with weights:

$$\omega_j = \frac{\tilde{\omega}_j}{\sum_k \tilde{\omega}_k} \qquad \tilde{\omega}_j = \frac{\zeta_j}{(o_s + \varepsilon)^r} \tag{22}$$

In this study, $r = 8$, $\varepsilon = 10^{-14}$, $\zeta_j = 10^5$ if S_j is a central stencil, and $\zeta_j = 1$ if S_j is a side stencil, as in [25].

The Discontinuous Galerkin Predictor   Take a non conservative, hyperbolic system of the form:

$$\frac{\partial \boldsymbol{Q}}{\partial t} + \frac{\partial \boldsymbol{F}(\boldsymbol{Q})}{\partial x} + B(\boldsymbol{Q}) \cdot \frac{\partial \boldsymbol{Q}}{\partial x} = \boldsymbol{S}(\boldsymbol{Q}) \tag{23}$$

where $\boldsymbol{Q}$ is the vector of conserved variables, $\boldsymbol{F}$ is the conservative nonlinear flux, B is the block matrix corresponding to the purely non conservative component of the system, and $\boldsymbol{S}(\boldsymbol{Q})$ is the algebraic source vector. Defining $M = \frac{\partial \boldsymbol{F}}{\partial \boldsymbol{Q}} + B$ this becomes:

$$\frac{\partial \boldsymbol{Q}}{\partial t} + M(\boldsymbol{Q}) \cdot \frac{\partial \boldsymbol{Q}}{\partial x} = \boldsymbol{S}(\boldsymbol{Q}) \tag{24}$$

Take the grid for the previous section, and time steps $t_0 < t_1 < \ldots$ while defining $\Delta t_n = t_{n+1} - t_n$. Combining the techniques presented in [22, 25], the Discontinuous Galerkin method produces at each time step t_n a local polynomial approximation to $\boldsymbol{Q}$ on each space time cell $C_i \times [t_n, t_{n+1}]$.

Define the scaled time variable:

$$\tau^n = \frac{1}{\Delta t_n}(t - t_n) \tag{25}$$

Using these variables gives:

$$\frac{\partial \boldsymbol{Q}}{\partial \tau^n} + \frac{\partial \boldsymbol{F}^*(\boldsymbol{Q})}{\partial \chi^i} + B^*(\boldsymbol{Q}) \cdot \frac{\partial \boldsymbol{Q}}{\partial \chi^i} = \boldsymbol{S}^*(\boldsymbol{Q}) \tag{26}$$

where

$$\boldsymbol{F}^* = \frac{\Delta t_n}{\Delta x}\boldsymbol{F} \qquad B^* = \frac{\Delta t_n}{\Delta x}B \qquad \boldsymbol{S}^* = \Delta t_n \boldsymbol{S} \tag{27}$$

9

The non dimensionalisation notation and spacetime cell indexing notation will be dropped for simplicity in what follows. Using the same nodal basis as in the previous section, define the set of spatio temporal basis functions:

$$\{\theta_k\left(\chi,\tau\right) = \psi_p\left(\chi\right)\psi_s\left(\tau\right) : 0 \leq p, s \leq N\} \tag{28}$$

The *nodal basis representation* is the following set of approximations:

$$\boldsymbol{Q} \approx \boldsymbol{q_h} = \theta_\beta \boldsymbol{q_\beta} \tag{29a}$$

$$\boldsymbol{F}\left(\boldsymbol{Q}\right) \approx \theta_\beta \boldsymbol{F}\left(\boldsymbol{q_\beta}\right) \tag{29b}$$

$$B\left(\boldsymbol{Q}\right) \cdot \frac{\partial \boldsymbol{Q}}{\partial \chi} \approx \theta_\beta B\left(\boldsymbol{q_\beta}\right) \cdot \left(\frac{\partial \theta_\gamma\left(\chi_\beta,\tau_\beta\right)}{\partial \chi} \boldsymbol{q_\gamma}\right) \tag{29c}$$

$$\boldsymbol{S}\left(\boldsymbol{Q}\right) \approx \theta_\beta \boldsymbol{S}\left(\boldsymbol{q_\beta}\right) \tag{29d}$$

where (χ_β, τ_β) are the coordinates of the Legendre node corresponding to basis function θ_β. Define the integral operators:

$$[f,g]^\tau = \int_0^1 f\left(\chi,\tau\right) g\left(\chi,\tau\right) d\chi \tag{30a}$$

$$\langle f,g \rangle = \int_0^1 \int_0^1 f\left(\chi,\tau\right) g\left(\chi,\tau\right) d\chi d\tau \tag{30b}$$

Using the nodal basis representation, multiplying (26) by test function θ_α and integrating over space and time gives:

$$\left\langle \theta_\alpha, \frac{\partial \theta_\beta}{\partial \tau} \right\rangle \boldsymbol{q_\beta} = - \left\langle \theta_\alpha, \frac{\partial \theta_\beta}{\partial \chi} \right\rangle \boldsymbol{F}\left(\boldsymbol{q_\beta}\right) \tag{31}$$
$$+ \langle \theta_\alpha, \theta_\beta \rangle \left(\boldsymbol{S}\left(\boldsymbol{q_\beta}\right) - B\left(\boldsymbol{q_\beta}\right) \cdot \left(\frac{\partial \theta_\gamma\left(\chi_\beta,\tau_\beta\right)}{\partial \chi} \boldsymbol{q_\gamma} \right) \right)$$

Integrating by parts in time gives:

$$\left([\theta_\alpha, \theta_\beta]^1 - \left\langle \frac{\partial \theta_\alpha}{\partial \tau}, \theta_\beta \right\rangle \right) \boldsymbol{q_\beta} = [\theta_\alpha, \boldsymbol{w}]^0 - \left\langle \theta_\alpha, \frac{\partial \theta_\beta}{\partial \chi} \right\rangle \boldsymbol{F}\left(\boldsymbol{q_\beta}\right) \tag{32}$$
$$+ \langle \theta_\alpha, \theta_\beta \rangle \left(\boldsymbol{S}\left(\boldsymbol{q_\beta}\right) - B\left(\boldsymbol{q_\beta}\right) \cdot \left(\frac{\partial \theta_\gamma\left(\chi_\beta,\tau_\beta\right)}{\partial \chi} \boldsymbol{q_\gamma} \right) \right)$$

10

where $\boldsymbol{w} = \boldsymbol{w_\gamma}\psi_\gamma$ is the reconstruction obtained at the start of the time step with the WENO method. Define the following notation:

$$U_{\alpha\beta} = [\theta_\alpha, \theta_\beta]^1 - \left\langle \frac{\partial\theta_\alpha}{\partial\tau}, \theta_\beta \right\rangle \tag{33a}$$

$$V_{\alpha\beta} = \left\langle \theta_\alpha, \frac{\partial\theta_\beta}{\partial\chi} \right\rangle \tag{33b}$$

$$W_{\alpha\gamma} = [\theta_\alpha, \psi_\gamma]^0 \tag{33c}$$

$$Z_{\alpha\beta} = \langle \theta_\alpha, \theta_\beta \rangle \tag{33d}$$

Thus:

$$U_{\alpha\beta}\boldsymbol{q_\beta} = W_{\alpha\gamma}\boldsymbol{w_\gamma} - V_{\alpha\beta}\boldsymbol{F}(\boldsymbol{q_\beta}) + Z_{\alpha\beta}\left(\boldsymbol{S}(\boldsymbol{q_\beta}) - B(\boldsymbol{q_\beta}) \cdot \left(\frac{\partial\theta_\gamma(\chi_\beta, \tau_\beta)}{\partial\chi}\boldsymbol{q_\gamma}\right)\right) \tag{34}$$

This nonlinear system in $\boldsymbol{q_\beta}$ is solved by a Newton method. The source terms must be solved implicitly if they are stiff.

The Predictor Initial Guess

Let the initial guess for the nonlinear system of the DG predictor be $\boldsymbol{q_h^0} = \theta_k\boldsymbol{\hat{q}_k}$. In [24] this is taken to be the WENO reconstruction, i.e. $\boldsymbol{q_h^0}(\chi, \tau) = \boldsymbol{w}(\chi)$ for $\tau \in [0, 1]$. In [43], a more sophisticated initial guess is used for systems of the form (23) with $B = 0$. Denote the Gauss Legendre abscissae on $[0, 1]$ by $\{\tau_0, \ldots, \tau_N\}$. Let $\Delta\tau_j = \tau_{j+1} - \tau_j$. Letting $\boldsymbol{q_h^0} = \psi_i(\chi)\psi_j(\tau)\boldsymbol{\hat{q}_{ij}}$:

$$\boldsymbol{\hat{q}_{i,j+1}} = \boldsymbol{\hat{q}_{ij}} - \Delta\tau_j\frac{\partial\boldsymbol{F}(\boldsymbol{\hat{q}_{ij}})}{\partial x} + \frac{\Delta\tau_j}{2}(\boldsymbol{S}(\boldsymbol{\hat{q}_{i,j+1}}) + \boldsymbol{S}(\boldsymbol{\hat{q}_{ij}})) \tag{35a}$$

$$\boldsymbol{\hat{q}_{i0}} = \boldsymbol{w_i} \tag{35b}$$

An explicit second order Taylor method is used to solve the flux term, combined with a second order Crank–Nicholson scheme for the stiff source term. In this study, this method was adapted to deal with the non conservative terms:

$$\boldsymbol{\hat{q}_{i,j+1}} = \boldsymbol{\hat{q}_{ij}} - \Delta\tau_j M(\boldsymbol{\hat{q}_{ij}}) \cdot \left(\frac{\partial\psi_k}{\partial\chi}\boldsymbol{\hat{q}_{kj}}\right) + \frac{\Delta\tau_j}{2}(\boldsymbol{S}(\boldsymbol{\hat{q}_{i,j+1}}) + \boldsymbol{S}(\boldsymbol{\hat{q}_{ij}})) \tag{36a}$$

$$\boldsymbol{\hat{q}_{i0}} = \boldsymbol{w_i} \tag{36b}$$

11

where M is given in (24). The Taylor method for the flux term is no longer necessary. The system was solved by a Newton method to deal with the stiff source term.

It was found that the more sophisticated initial guess would reduce overall computation times on some problems, owing to a faster convergence of the DG calculation. On other problems, the total computation time would increase, owing to the added cost of calculating the initial guess. See [21, 23, 32] for other choices for the initial guess.

The Finite Volume Scheme   Following the formulation of [25], integrating (23) over $[t_n, t_{n+1}] \times C_i$ gives:

$$\boldsymbol{Q}_i^{n+1} = \boldsymbol{Q}_i^n + \Delta t_n \left(\boldsymbol{S}_i^n - \boldsymbol{P}_i^n\right) - \frac{\Delta t_n}{\Delta x} \left(\boldsymbol{D}_{i+1}^n - \boldsymbol{D}_i^n\right) \tag{37}$$

where

$$\boldsymbol{Q}_i^n = \frac{1}{\Delta x} \int_{x_i}^{x_{i+1}} \boldsymbol{Q}\left(x, t_n\right) dx \tag{38a}$$

$$\boldsymbol{S}_i^n = \frac{1}{\Delta t_n \Delta x} \int_{t_n}^{t_{n+1}} \int_{x_i}^{x_{i+1}} \boldsymbol{S}\left(\boldsymbol{Q}\right) dx dt \tag{38b}$$

$$\boldsymbol{P}_i^n = \frac{1}{\Delta t_n \Delta x} \int_{t_n}^{t_{n+1}} \int_{x_i}^{x_{i+1}} B\left(\boldsymbol{Q}\right) \cdot \frac{\partial \boldsymbol{Q}}{\partial x} dx dt \tag{38c}$$

$$\boldsymbol{D}_i^n = \frac{1}{\Delta t_n} \int_{t_n}^{t_{n+1}} \boldsymbol{\mathcal{D}}\left(\boldsymbol{Q}^-\left(x_i, t\right), \boldsymbol{Q}^+\left(x_i, t\right)\right) dt \tag{38d}$$

$\boldsymbol{Q}^-, \boldsymbol{Q}^+$ are the left and right extrapolated states at the x_i boundary. $\boldsymbol{S}_i^n, \boldsymbol{P}_i^n, \boldsymbol{D}_i^n$ are calculated using an $N + 1$ point Gauss Legendre quadrature, replacing $\boldsymbol{Q}$ with $\boldsymbol{q_h}$.

M, as defined in Section 2.4, is a diagonalisable matrix with decomposition $M = R\Lambda R^{-1}$ where the columns of R are the right eigenvectors and Λ is the diagonal matrix of eigenvalues. Define the following matrix:

$$|M| = R\left|\Lambda\right| R^{-1} \tag{39}$$

Using these definitions, the interface terms arising in the FV formula have the following form:

$$\boldsymbol{\mathcal{D}}\left(\boldsymbol{q}^-, \boldsymbol{q}^+\right) = \frac{1}{2} \left(\boldsymbol{F}\left(\boldsymbol{q}^-\right) + \boldsymbol{F}\left(\boldsymbol{q}^+\right) + \hat{B} \cdot \left(\boldsymbol{q}^+ - \boldsymbol{q}^-\right) - \hat{M} \cdot \left(\boldsymbol{q}^+ - \boldsymbol{q}^-\right)\right) \tag{40}$$

$\hat{M}$ is chosen to either correspond to a Rusanov/Lax Friedrichs flux [82]:

$$\hat{M} = \max\left(\max\left|\Lambda\left(\boldsymbol{q}^-\right)\right|, \max\left|\Lambda\left(\boldsymbol{q}^+\right)\right|\right) \tag{41}$$

12
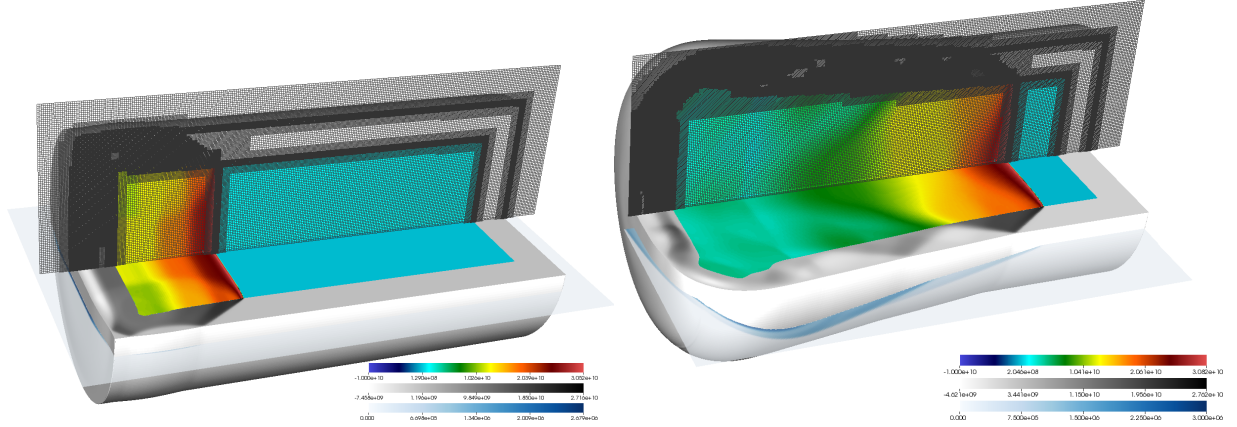
Figure 1: Impact induced detonation of a combustible material in an elasto plastic confiner (at two different points in time). Test taken from [62].

or a simplified Osher–Solomon flux [29, 30]:

$$\hat{M} = \int_0^1 \left| M \left(\boldsymbol{q}^- + z \left(\boldsymbol{q}^+ - \boldsymbol{q}^- \right) \right) \right| dz \tag{42}$$

$\hat{B}$ takes the following form:

$$\hat{B} = \int_0^1 B \left(\boldsymbol{q}^- + z \left(\boldsymbol{q}^+ - \boldsymbol{q}^- \right) \right) dz \tag{43}$$

It was found that the Osher Solomon flux would often produce slightly less diffusive results, but that it was more computationally expensive, and also had a greater tendency to introduce numerical artefacts.

3   Research Objectives

The objective of my PhD project is to develop the GPR model in various specific ways so that it may be used to simulate the problems of impact induced detonation of a combustible material in an elasto plastic confiner. A graphical representation of this problem is shown in Figure 1 on page 13. As can be seen, three states of matter are present (a solid confiner, a liquid combustible confined material, and gaseous surrounding environment). The interfaces between these phases and the exchange of state information between them need to be dealt with in any numerical method employed. The GPR model must also be augmented in some way to capture the kinetics of the chemical reactions present. Up until now, ADER WENO methods have been used to solve the GPR model (as described in paper 2.4). Whilst these are able to provide arbirarily high order accuracy solutions in both space and time, they are too slow for the practical applications that we envisage in our lab, even at second order accuracy; faster numerical solvers are needed.

Thus, there are three main issues that I am addressing in my work:

1. To develop stable and accurate techniques to deal with the interfaces between different materials in multimaterial / multiphase problems

2. To combine the GPR model with the models we use to describe the reactions of a combustible materials

3. To develop numerical methods for solving the GPR model in a reasonable amount of time

4   Work Completed

Addressing the three main issues listed above, I have:

1. Developed a Riemann Ghost Fluid Method for the GPR model to deal with material interfaces. This is described in 4.1.

2. Combined the GPR model with a simple model of arrhenius reaction kinetics. This is described in 4.2.

3. Developed a second order numerical method for solving the GPR model that is significantly faster than existing ADER WENO methods. I have also reformulated the equatons of the GPR model so that the eigendecomposition of the G matrix is evolved, rather than G itself, again speeding up calculations. These advances are described in 4.3 and 4.4, respectively.

The work in 4.1 and 4.2 has been put into two different papers that I will be submitting to the Journal of Computational Physics (JCP) and Combustion and Flame respectively. The work from 4.3 can be found in [47], which has recently been accepted in JCP. See also [48] for a paper I had published earlier this year regarding the convergence properties of the ADER WENO methods used in my project.

I spoke at the Sixteenth International Conference on Numerical Combustion in Orlando in April (presenting the work in 4.2) and at the International Conference in Computational Science in Zurich in early June (presenting the work in 4.3). Additionally, I presented my work this year at the Cavendish Graduate Student Conference, the Maxwell Showcase Day, and the Scientific Computation Day in Cambridge.

I've made publicly available as much of the software that I have produced as possible, for use by others (please see my GitHub page, github.com/haranjackson). Notably, mine is the only publicly available implementation of the popular ADER WENO method (my code is being followed by several researchers internationally), and I have also provided the first Julia implementation of the WENO method. I have also been working on code to potentially replace parts of my lab's commercial software offering.

My own non public code base is extensive, implementing the material provided in this report and many experiemental features, in both Python and C++. A fair amount of my work this year has been spent on this too.
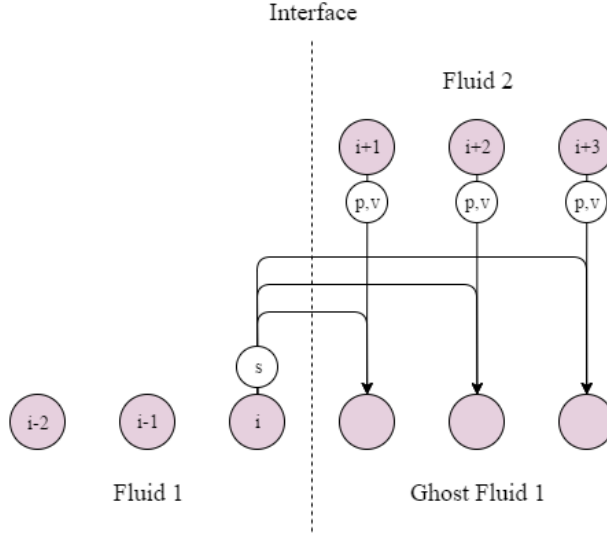
Figure 2: The Original Ghost Fluid Method

4.1 Simulating Material Interfaces

4.1.1 Ghost Fluid Methods

Ghost fluid methods, combined with level set methods, are used to model the evolution of interfaces between different materials. They are detailed here, as it is with such a method that this study proposes to model the interfaces between different materials described by the GPR model.

Level Set Methods Given a function f on $\mathbb{R}$, the level set of f at level c is defined as:

$$\Gamma_c = \{x : f(x) = c\} \tag{44}$$

Given velocity field $v : \mathbb{R} \to \mathbb{R}$, f is advected according to the level set equation [67]:

$$\frac{\partial f}{\partial t} = v \left| \frac{\partial f}{\partial x} \right| \tag{45}$$

The advection of a point in a fluid with velocity v can be modeled by taking $f = x - x_0$ where x_0 is the position of the point at time $t = 0$, and tracking Γ_0. (45) is solved by an appropriate numerical method. The numerical methods used in this study are described in Chapter 4.1.2. f will usually have to be renormalized to resemble a straight line at every time step, to avoid unwanted distortions such as becoming a multivalued function.

15

The Original Ghost Fluid Method   The Original Ghost Fluid Method of Fedkiw et al. [34] (an adap
tation of the work of Glimm et al. [39]) is a numerical method for the Euler equations for simulating
interfaces between multiple materials. The primitive variables for the Euler equations in 1D are given by
$\boldsymbol{P} = \left(\begin{array}{ccc} \rho & v & p \end{array} \right)^T$.

Suppose the interface between two fluids is modeled on spatial domain $[0, 1]$, divided into N cells with width
$\Delta x = \frac{1}{N}$. Let the time step be Δt and let $\boldsymbol{P}_i^n$ be the set of primitive variables in cell i at time $t_n = n\Delta t$.
Let the level set function f have root x_n where $x_n \in \left[(i + \frac{1}{2})\Delta x, (i + \frac{3}{2})\Delta x \right]$. Thus, at time t_n the interface
lies between the cells with primitive variables $\boldsymbol{P}_i^n, \boldsymbol{P}_{i+1}^n$. Define two sets of primitive variables:

$$P_j^{(1)} = \begin{cases} \boldsymbol{P}_j^n & j \leq i \\ \left(\begin{array}{ccc} \rho\left(s_i^n, p_j^n, \gamma_i^n\right) & v_j^n & p_j^n \end{array} \right) & j > i \end{cases} \tag{46}$$

$$P_j^{(2)} = \begin{cases} \boldsymbol{P}_j^n & j \geq i + 1 \\ \left(\begin{array}{ccc} \rho\left(s_{i+1}^n, p_j^n, \gamma_{i+1}^n\right) & v_j^n & p_j^n \end{array} \right) & j < i + 1 \end{cases} \tag{47}$$

where:

$$\rho\left(s, p, \gamma\right) = \left(\frac{p}{s}\right)^{\frac{1}{\gamma}} \tag{48}$$

All cells in $\boldsymbol{P}^{(1)}$ to the left of the interface have the same state variables as those of $\boldsymbol{P}^n$. All cells to the
right have the same pressure and velocity as their counterparts in $\boldsymbol{P}^n$, but the same entropy as $\boldsymbol{P}_i^n$. This
affects their density. The situation is analogous for $\boldsymbol{P}^{(2)}$. This is demonstrated in Figure 2 on page 15.

$\boldsymbol{P}^{(1)}, \boldsymbol{P}^{(2)}$ are stepped forward by time step Δt using a standard Eulerian method. f is advected using (45),
taking the velocity in each cell to be that of $\boldsymbol{P}^n$. Now let $f\left(x_{n+1}\right) = 0$ where $x_{n+1} \in \left[\left(k + \frac{1}{2}\right)\Delta x, \left(k + \frac{3}{2}\right)\Delta x \right]$
for some k. Define:

$$P_j^{n+1} = \begin{cases} P_j^{(1)} & j \leq k \\ P_j^{(2)} & j > k \end{cases} \tag{49}$$

The rationale behind the original GFM is that in most applications, pressure and velocity are continuous
across the interface, and thus the ghost cells may take the real pressure and velocity values. Entropy is
generally discontinuous at a contact discontinuity, resulting in large truncation errors if a standard finite
difference scheme is used to solve the system. Thus, entropy is extrapolated as a constant from the interface
boundary cell into the ghost region.

Fedkiw et al. advised to use the *isobaric fix* technique. This involves setting the entropy of cell i, and all
cells in the right ghost region, to that of cell $i - 1$, and setting the entropy of cell $i + 1$, and all cells in the
left ghost region, to that of cell $i + 2$. This is demonstrated in Figure 3 on page 17.
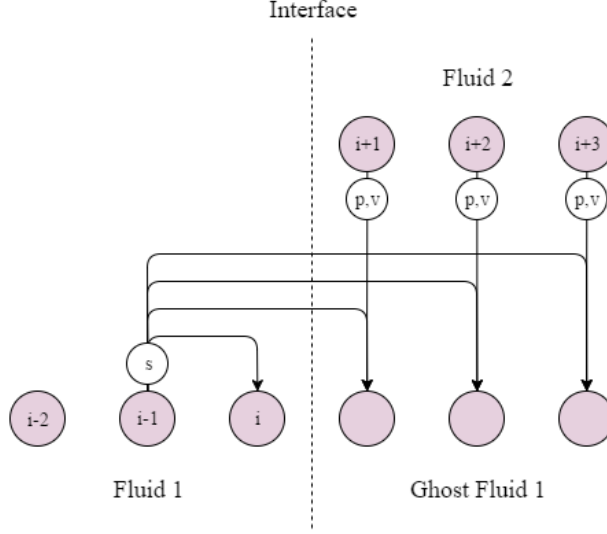
Figure 3: The Original Ghost Fluid Method, with the isobaric fix

Effectively, the ghost regions behave like they are composed of the same fluid as the regions they extend (as they have the same entropy), facilitating calculation of the next time step, but they have the same pressure and velocity profiles as the real fluids they replace, meaning the boundary conditions at the interface are upheld.

The Riemann Ghost Fluid Method   The Riemann Problem in its general form is the solution of the following initial value problem. Given a set of variables $\boldsymbol{P}$ dependent on space and time, and a hyperbolic set of equations which govern their spatio temporal evolution, $\boldsymbol{P}(x,t)$ is sought for $t > 0$, given the initial condition:

$$\boldsymbol{P}(x,0) = \begin{cases} \boldsymbol{P_L} & x < 0 \\ \boldsymbol{P_R} & x > 0 \end{cases} \tag{50}$$

This problem is denoted by $RP(\boldsymbol{P_L}, \boldsymbol{P_R})$. Exact solvers exist for the Riemann Problem for various sets of governing equations, such as the Euler equations [82], the equations of non linear elasticity [7], or the shallow water equations [3], among others. There also exist approximate solvers for general conservative [65, 58] or non conservative [19] hyperbolic systems of PDEs. The references given here form a very small sample of the work that has been done in this area.

The solution of the Riemann Problem usually takes the form of a set of waves, between which $\boldsymbol{P}$ is constant. The waves can either be a contact discontinuity (across which pressure and velocity are continuous), a shock (across which all variables may be discontinuous), or a rarefaction (along which the variables vary continuously between their values on either side of the wave). The number and form of the waves are determined by the governing equations and the initial conditions. The states of the variables either side of
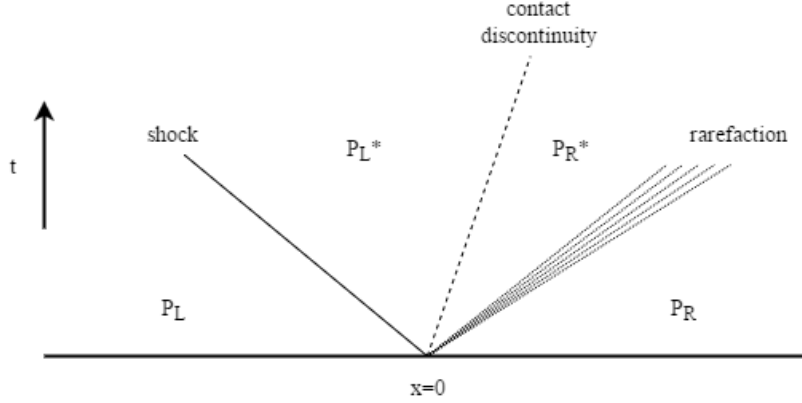
Figure 4: The qualitative structure of the solution to the Riemann Problem, showing the different possible types of waves

the contact discontinuity in the middle are known as the *star states*. This qualitative description is depicted in Figure 4 on page 18.

Liu et al. [57] demonstrated that the original GFM fails to resolve strong shocks at material interfaces. This is because the method effectively solves two separate single fluid Riemann problems. The waves present in these Riemann problems do not necessarily correspond to those in the real Riemann problem across the interface. The Riemann Ghost Fluid Method of Sambasivan et al. [76] aims to rectify this.

Given $\boldsymbol{P^n}$ and $x_n \in \left[\left(i + \frac{1}{2}\right)\Delta x, \left(i + \frac{3}{2}\right)\Delta x\right]$, the ghost cells for fluid 1 are populated with the left star state of $RP\left(\boldsymbol{P_{i-1}^n}, \boldsymbol{P_{i+2}^n}\right)$, and the ghost cells for fluid 2 are populated with the right star state. $RP\left(\boldsymbol{P_{i-1}^n}, \boldsymbol{P_{i+2}^n}\right)$ is solved rather than $RP\left(\boldsymbol{P_i^n}, \boldsymbol{P_{i+1}^n}\right)$, as $\boldsymbol{P_i^n}, \boldsymbol{P_{i+1}^n}$ often contain errors generated by the fact that they lie on the material interface. $\boldsymbol{P^{n+1}}$ is then generated as before from the newly formed $\boldsymbol{P^{(1)}}, \boldsymbol{P^{(2)}}$. This process is demonstrated in Figure 5 on page 19.

4.1.2 A Riemann Ghost Fluid Method for the GPR Model

Eigenstructure of the GPR Model Considering the primitive system matrix M_1 given in Section 6.1, it is clear that the eigenvalues of the GPR system in the first spatial axis consist of v_1 repeated 8 times, along with the roots of:

$$\begin{vmatrix} (v_1 - \lambda)\,I & \Xi_2 \\ \Xi_1 & (v_1 - \lambda)\,I \end{vmatrix} = 0 \tag{51}$$

where
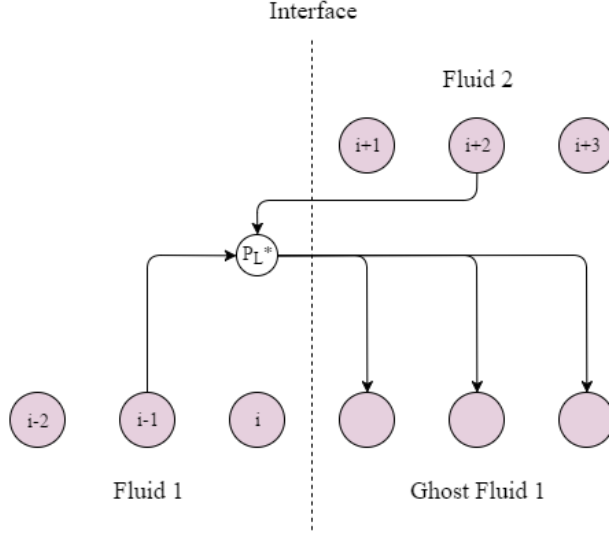
Figure 5: The Riemann Ghost Fluid Method

$$\Xi_1 = \begin{pmatrix} -\frac{\sigma_{11}}{\rho^2} & \frac{1}{\rho} & -\frac{1}{\rho}\frac{\partial \sigma_{11}}{\partial A_{11}} & -\frac{1}{\rho}\frac{\partial \sigma_{11}}{\partial A_{21}} & -\frac{1}{\rho}\frac{\partial \sigma_{11}}{\partial A_{31}} \\ -\frac{\sigma_{21}}{\rho^2} & 0 & -\frac{1}{\rho}\frac{\partial \sigma_{21}}{\partial A_{11}} & -\frac{1}{\rho}\frac{\partial \sigma_{21}}{\partial A_{21}} & -\frac{1}{\rho}\frac{\partial \sigma_{21}}{\partial A_{31}} \\ -\frac{\sigma_{31}}{\rho^2} & 0 & -\frac{1}{\rho}\frac{\partial \sigma_{31}}{\partial A_{11}} & -\frac{1}{\rho}\frac{\partial \sigma_{31}}{\partial A_{21}} & -\frac{1}{\rho}\frac{\partial \sigma_{31}}{\partial A_{31}} \\ -\frac{T}{\rho^2} & \frac{T}{\rho(p+p_\infty)} & 0 & 0 & 0 \end{pmatrix} \quad (52)$$

$$\Xi_2 = \begin{pmatrix} \rho & 0 & 0 & 0 \\ \gamma p & 0 & 0 & (\gamma-1)\alpha^2 T \\ A_{11} & A_{12} & A_{13} & 0 \\ A_{21} & A_{22} & A_{23} & 0 \\ A_{31} & A_{32} & A_{33} & 0 \end{pmatrix} \quad (53)$$

By the properties of block matrices[2], the remaining eigenvalues are v_1 and the roots of $\left| (v_1 - \lambda)^2 I - \Xi_1 \Xi_2 \right| = 0$. Thus, $\lambda_i = v_1 \pm \sqrt{\tilde{\lambda}_i}$ where the $\tilde{\lambda}_i$ are the eigenvalues of the following matrix:

$$\Xi = \Xi_1 \Xi_2 = \begin{pmatrix} \frac{\gamma p}{\rho} + \Omega_{11}^1 & \Omega_{12}^1 & \Omega_{13}^1 & \frac{(\gamma-1)\alpha^2 T}{\rho} \\ \Omega_{21}^1 & \Omega_{22}^1 & \Omega_{23}^1 & 0 \\ \Omega_{31}^1 & \Omega_{32}^1 & \Omega_{33}^1 & 0 \\ \frac{((\gamma-1)p-p_\infty)T}{\rho(p+p_\infty)} & 0 & 0 & \frac{(\gamma-1)\alpha^2 T^2}{\rho(p+p_\infty)} \end{pmatrix} \quad (54)$$

where an analytic form for Ω is given in the next section. Similar results hold for the other two spatial directions. In general it is not possible to express the eigenvalues of Ξ in terms of the eigenvalues of its

---

[2]If A is invertible, $\det \begin{pmatrix} A & B \\ C & D \end{pmatrix} = \det(A)\det\left(D - CA^{-1}B\right)$

submatrices. Note, however, that if $\alpha = 0$ then one of the eigenvalues is 0 and the remaining eigenvalues can be found analytically, using the form given in the appendix of [27].

It is straightforward to verify the following:

$$\frac{\partial \sigma_{ij}}{\partial A_{mn}} = -c_s^2 \rho \left(\delta_{in} \left(A \operatorname{dev}(G) \right)_{mj} + \delta_{jn} \left(A \operatorname{dev}(G) \right)_{mi} + A_{mi}G_{jn} + A_{mj}G_{in} - \frac{2}{3} G_{ij} A_{mn} \right) \tag{55}$$

The quantity Ω is named here the *acoustic tensor*, due to its similarity to the acoustic tensor described in [7]:

$$
\begin{aligned}
\Omega_{ij}^d &= -\frac{1}{\rho} \frac{\partial \sigma_{id}}{\partial A_{kd}} A_{kj} - \frac{\sigma_{id}}{\rho} \delta_{dj} \\
&= c_s^2 \left(\delta_{id} \left(G \operatorname{dev}(G) \right)_{dj} + \left(G \operatorname{dev}(G) \right)_{id} \delta_{dj} + \left(G \operatorname{dev}(G) \right)_{ij} + G_{ij} G_{dd} + \frac{1}{3} G_{dj} G_{id} \right) \\
&= c_s^2 \left(E^d G \operatorname{dev}(G) + G \operatorname{dev}(G) E^d + G \operatorname{dev}(G) + G_{dd} G + \frac{1}{3} G_d G_d^T \right)
\end{aligned}
\tag{56}
$$

where $E_{ij}^d = \delta_{id} \delta_{jd}$.

By hyperbolicity of the system, Ξ can be expressed as:

$$\Xi = Q^{-1} D^2 Q \tag{57}$$

where D is a diagonal matrix with positive diagonal entries. The eigenvectors corresponding to $\lambda_i = v_1 \pm \sqrt{\tilde{\lambda}_i}$ take the form $\begin{pmatrix} \boldsymbol{u_1} & \boldsymbol{0_6} & \boldsymbol{u_2} & \boldsymbol{0_2} \end{pmatrix}^T$ where $\boldsymbol{u_1} \in \mathbb{R}^5$, $\boldsymbol{u_2} \in \mathbb{R}^4$ satisfy:

$$\begin{pmatrix} v_1 I & \Xi_2 \\ \Xi_1 & v_1 I \end{pmatrix} \begin{pmatrix} \boldsymbol{u_1} \\ \boldsymbol{u_2} \end{pmatrix} = \left(v_1 \pm \sqrt{\tilde{\lambda}_i} \right) \begin{pmatrix} \boldsymbol{u_1} \\ \boldsymbol{u_2} \end{pmatrix} \tag{58}$$

Thus, $\Xi_2 \boldsymbol{u_2} = \pm \sqrt{\tilde{\lambda}_i} \boldsymbol{u_1}$ and $\Xi_1 \boldsymbol{u_1} = \pm \sqrt{\tilde{\lambda}_i} \boldsymbol{u_2}$. Combining these results, $\Xi \boldsymbol{u_2} = \tilde{\lambda}_i \boldsymbol{u_2}$. Thus, $\boldsymbol{u_2}$ is a right eigenvector of Ξ and, taking the form $Q^{-1} \boldsymbol{e_i}$ for some $i = 1 \ldots 4$.

Let $\Pi_k^{ij} = \frac{\partial \sigma_{i1}}{\partial A_{jk}}$. Using the result just obtained, the four eigenvectors corresponding to eigenvalues of the form $v_1 + \sqrt{\tilde{\lambda}_i}$ are columns 1 4 of matrix R below. Those corresponding to eigenvalues of the form $v_1 - \sqrt{\tilde{\lambda}_i}$ are columns 5 8. By inspection, it can be verified that the remaining 9 eigenvectors (corresponding to eigenvalue v_1) are the remaining columns.

$$R = \frac{1}{2} \begin{pmatrix} \left(\Xi_2 \left(DQ\right)^{-1}\right)_{1,:} & \left(\Xi_2 \left(DQ\right)^{-1}\right)_{1,:} & c\rho & 0 & 0 & 0 \\ \left(\Xi_2 \left(DQ\right)^{-1}\right)_{2,:} & \left(\Xi_2 \left(DQ\right)^{-1}\right)_{2,:} & c\left(p+p_\infty\right) & 0 & 0 & 0 \\ \left(\Xi_2 \left(DQ\right)^{-1}\right)_{3:5,:} & \left(\Xi_2 \left(DQ\right)^{-1}\right)_{3:5,:} & c\Pi_1^{-1}b & -2\Pi_1^{-1}\Pi_2 & -2\Pi_1^{-1}\Pi_3 & 0 \\ 0 & 0 & 0 & 2I_3 & 0 & 0 \\ 0 & 0 & 0 & 0 & 2I_3 & 0 \\ Q^{-1} & -Q^{-1} & 0 & 0 & 0 & 0 \\ 0 & 0 & 0 & 0 & 0 & 2I_2 \end{pmatrix} \tag{59}$$

where

$$b = \begin{pmatrix} p + p_\infty - \sigma_{11} \\ -\sigma_{12} \\ -\sigma_{13} \end{pmatrix} \tag{60a}$$

$$c = \frac{2}{e_1^T \left(\Pi_1 A\right)^{-1} b - 1} \tag{60b}$$

A similar analysis yields the left eigenvectors as the rows of the following matrix:

$$L = \begin{pmatrix} \left(D^{-1}Q\Xi_1\right)_1 & \left(D^{-1}Q\Xi_1\right)_2 & \left(D^{-1}Q\Xi_1\right)_{3:5} & -\frac{1}{\rho}D^{-1}Q_{1:3}\Pi_2 & -\frac{1}{\rho}D^{-1}Q_{1:3}\Pi_3 & Q & 0 \\ \left(D^{-1}Q\Xi_1\right)_1 & \left(D^{-1}Q\Xi_1\right)_2 & \left(D^{-1}Q\Xi_1\right)_{3:5} & -\frac{1}{\rho}D^{-1}Q_{1:3}\Pi_2 & -\frac{1}{\rho}D^{-1}Q_{1:3}\Pi_3 & -Q & 0 \\ -\frac{1}{\rho} & 0 & e_1^T A^{-1} & e_1^T A^{-1}\Pi_1^{-1}\Pi_2 & e_1^T A^{-1}\Pi_1^{-1}\Pi_3 & 0 & 0 \\ 0 & 0 & 0 & I_3 & 0 & 0 & 0 \\ 0 & 0 & 0 & 0 & I_3 & 0 & 0 \\ 0 & 0 & 0 & 0 & 0 & 0 & I_2 \end{pmatrix} \tag{61}$$

In the form given here, $L = R^{-1}$.

A GPR Riemann Ghost Fluid Method Barton et al. have presented an RGFM for the equations of non linear elasticity [8, 6]. Owing to the similarity of the structure of the non linear elasticity equations to those of the GPR model (differing only in the presence of source terms and the form of the shear stress tensor, and possibly the EOS), their method is built upon here. The resulting method is named *the GPR RGFM*.

The Riemann Problem of the GPR model takes the form demonstrated in Figure 6 on page 22. Assuming all waves are distinct, there are four waves on either side of the contact discontinuity. On each side, one wave corresponds to the thermal impulse (manifesting as a heat wave) and the other three correspond to the distortion components in the axis in which the Riemann Problem is considered (manifesting as two shear waves and one longitudinal pressure wave). In the following the effect of the source terms on the solution to

21
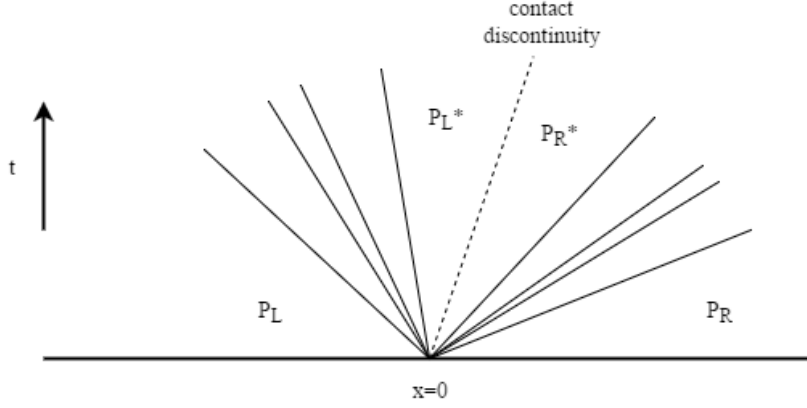
Figure 6: The Riemann Problem for the GPR model, assuming all waves are distinct

the RP is neglected. This is thought to be a reasonable assumption for the problem at hand, as only the star states are required, and the time step over which the RP is taken is very small. The method is presented here along the first spatial axis. It can easily be adapted along any axis.

Denote the vector of primitive variables by $\boldsymbol{P}$. Take the set of left eigenvectors L (61) with eigenvalues $\{\lambda_i\}$. Neglecting the effect of the source terms produces the standard set of relations along characteristics (curves along which $\frac{dx}{dt} = \lambda_i$):[3]

$$L \cdot d\boldsymbol{P} = \boldsymbol{0} \tag{62}$$

$\boldsymbol{P}_K^*$ is now sought, where $K = L$ or $K = R$, denoting the left or right sides of the interface, respectively. Take the following linearisation:

$$d\boldsymbol{P} \approx \boldsymbol{P}_K^* - \boldsymbol{P_K} \tag{63}$$

13 relations from (62) are taken: four regarding the 4 sets of characteristics traveling into the contact discontinuity from side K (with speeds greater or less than v for $K = L$ or $K = R$, respectively), and nine relating to the contact discontinuity itself. This is demonstrated in Figure 7 on page 23. Four more relations must be derived to solve the system for $\boldsymbol{P}_K^*$. Expanding the Taylor series of $q_1^*, \boldsymbol{\sigma_1^*}$:

---

[3]Take the hyperbolic system $\frac{\partial \boldsymbol{P}}{\partial t} + M \frac{\partial \boldsymbol{P}}{\partial x} = \boldsymbol{S}$. Let $\boldsymbol{l_i}^T M = \lambda_i \boldsymbol{l_i}^T$. Along characteristics corresponding to λ_i:

$$\boldsymbol{l_i^T} \left(\frac{\partial \boldsymbol{P}}{\partial t} + M \frac{\partial \boldsymbol{P}}{\partial x} \right) = \boldsymbol{l_i^T} \left(\frac{\partial \boldsymbol{P}}{\partial t} + \frac{dx}{dt} \frac{\partial \boldsymbol{P}}{\partial x} \right)$$

$$= \boldsymbol{l_i^T} \frac{d\boldsymbol{P}}{dt} = \boldsymbol{l_i^T} \boldsymbol{S}$$
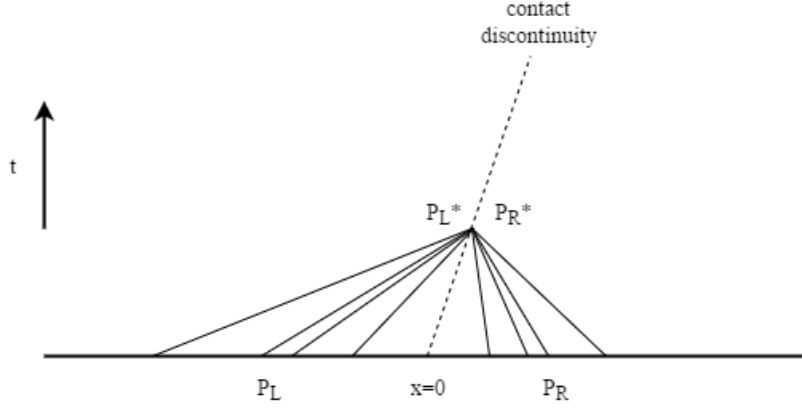
Figure 7: Different sets of characteristic curves, traveling from their respective initial points to the star region

$$q_1^* = q_1 + \frac{\partial q_1}{\partial \rho} \left(\rho^* - \rho\right) + \frac{\partial q_1}{\partial p} \left(p^* - p\right) + \frac{\partial q_1}{\partial J_1} \left(J_1^* - J_1\right) + \cdots \tag{64a}$$

$$\boldsymbol{\sigma_1^*} = \boldsymbol{\sigma_1} + \frac{\partial \boldsymbol{\sigma_1}}{\partial \rho} \left(\rho^* - \rho\right) + \frac{\partial \boldsymbol{\sigma_1}}{\partial A_{mn}} \left(A_{mn}^* - A_{mn}\right) + \cdots \tag{64b}$$

Thus, we have:

$$-\frac{q_1}{\rho} \left(\rho^* - \rho\right) + \frac{q_1}{p + p_\infty} \left(p^* - p\right) + \alpha^2 T \left(J_1^* - J_1\right) \approx q_1^* - q_1 \tag{65a}$$

$$\frac{\boldsymbol{\sigma_1}}{\rho} \left(\rho^* - \rho\right) + \frac{\partial \boldsymbol{\sigma_1}}{\partial A_{mn}} \left(A_{mn}^* - A_{mn}\right) \approx \boldsymbol{\sigma_1^*} - \boldsymbol{\sigma_1} \tag{65b}$$

These are the extra required relations. Thus:

$$\hat{L}_K \cdot \left(\boldsymbol{P_K^*} - \boldsymbol{P_K}\right) = \boldsymbol{c_K} \tag{66}$$

where $\hat{L}_K$ takes the following form, with $\xi = 1$ for $K = R$ and $\xi = -1$ for $K = L$:

23

$$\begin{pmatrix}
-\frac{q_1}{\rho} & \frac{q_1}{p+p_\infty} & 0 & 0 & 0 & 0 & \alpha^2 T & 0 \\
\frac{\sigma_1}{\rho} & 0 & \Pi_1 & \Pi_2 & \Pi_3 & 0 & 0 & 0 \\
\left(D^{-1}Q\Xi_1\right)_1 & \left(D^{-1}Q\Xi_1\right)_2 & \left(D^{-1}Q\Xi_1\right)_{3:5} & -\frac{1}{\rho}D^{-1}Q_{1:3}\Pi_2 & -\frac{1}{\rho}D^{-1}Q_{1:3}\Pi_3 & \xi Q_{1:3} & \xi\left(Q\right)_4 & 0 \\
-\frac{1}{\rho} & 0 & e_1^T A^{-1} & e_1^T A^{-1}\Pi_1^{-1}\Pi_2 & e_1^T A^{-1}\Pi_1^{-1}\Pi_3 & 0 & 0 & 0 \\
0 & 0 & 0 & I_3 & 0 & 0 & 0 & 0 \\
0 & 0 & 0 & 0 & I_3 & 0 & 0 & 0 \\
0 & 0 & 0 & 0 & 0 & 0 & 0 & I_2
\end{pmatrix} \tag{67}$$

$$\boldsymbol{c_K} = \begin{pmatrix} \left(q_1^*\right)_K - \left(q_1\right)_K \\ \left(\boldsymbol{\sigma_1^*}\right)_K - \left(\boldsymbol{\sigma_1}\right)_K \\ \boldsymbol{0} \end{pmatrix} \tag{68}$$

$\hat{L}_K$ is evaluated at $\boldsymbol{P_K}$. It remains to find expressions for $\boldsymbol{\sigma_1^*}$ and q_1^* in terms of $\boldsymbol{P_L}, \boldsymbol{P_R}$ to close the system. The following boundary conditions are used:

$$\left(\boldsymbol{\sigma_1^*}\right)_L = \left(\boldsymbol{\sigma_1^*}\right)_R \tag{69a}$$

$$\left(q_1^*\right)_L = \left(q_1^*\right)_R \tag{69b}$$

$$\boldsymbol{v_L^*} = \boldsymbol{v_R^*} \tag{69c}$$

$$p_L^* = p_R^* \tag{69d}$$

Define $\hat{R} = \hat{L}^{-1}$. The last 8 columns of $\hat{R}$ are equal to the last 8 columns of R, given in Section 4.1.2. Although it is possible to find an analytic form of the remaining columns of $\hat{R}$ in terms of Ξ_1, Ξ_2 and their submatrices, it is highly inelegant and not particularly instructive, so it is not given here. In this study, when $\hat{R}$ was required, it was found numerically. Note that:

$$\boldsymbol{P_K^*} = \boldsymbol{P_K} + \left(\hat{R}_K\right)_1 \left(q_1^* - q_1\right) + \left(\hat{R}_K\right)_{2:4} \left(\boldsymbol{\sigma_1^*} - \boldsymbol{\sigma_1}\right) \tag{70}$$

Thus:

$$p_K^* = p_K + \left(\hat{R}_K\right)_{2,1} \left(q_1^* - \left(q_1\right)_K\right) + \left(\hat{R}_K\right)_{2,2:4} \left(\boldsymbol{\sigma_1^*} - \left(\boldsymbol{\sigma_1}\right)_K\right) \tag{71a}$$

$$\boldsymbol{v_K^*} = \boldsymbol{v_K} + \left(\hat{R}_K\right)_{12:14,1} \left(q_1^* - \left(q_1\right)_K\right) + \left(\hat{R}_K\right)_{12:14,2:4} \left(\boldsymbol{\sigma_1^*} - \left(\boldsymbol{\sigma_1}\right)_K\right) \tag{71b}$$

Define:

$$\Theta_K = \begin{pmatrix} \left(\hat{R}_K\right)_{2,1} & \left(\hat{R}_K\right)_{2,2:4} \\ \left(\hat{R}_K\right)_{12:14,1} & \left(\hat{R}_K\right)_{12:14,2:4} \end{pmatrix} \tag{72}$$

Thus, using the boundary conditions:

$$\begin{pmatrix} p^* \\ \boldsymbol{v^*} \end{pmatrix} = \begin{pmatrix} p_K \\ \boldsymbol{v_K} \end{pmatrix} + \Theta_K \left(\begin{pmatrix} q_1^* \\ \boldsymbol{\sigma_1^*} \end{pmatrix} - \begin{pmatrix} (q_1)_K \\ (\boldsymbol{\sigma_1})_K \end{pmatrix} \right) \tag{73}$$

$$\therefore \begin{pmatrix} q_1^* \\ \boldsymbol{\sigma_1^*} \end{pmatrix} = (\Theta_L - \Theta_R)^{-1} \left(\begin{pmatrix} p_R \\ \boldsymbol{v_R} \end{pmatrix} - \begin{pmatrix} p_L \\ \boldsymbol{v_L} \end{pmatrix} + \Theta_L \begin{pmatrix} (q_1)_L \\ (\boldsymbol{\sigma_1})_L \end{pmatrix} - \Theta_R \begin{pmatrix} (q_1)_R \\ (\boldsymbol{\sigma_1})_R \end{pmatrix} \right) \tag{74}$$

Thus, $\boldsymbol{P_L^*}, \boldsymbol{P_R^*}$ are obtained with (66) and used in the RGFM, as described in Section 4.1.1.

It may be necessary to iterate this process a few times to ensure convergence to star states for which the boundary conditions hold. The convergence properties of this process are unknown, and there may be issues with stability and robustness. No significant issues were encountered in this study, however.

The Temperature Fix　In the original GFM, the entropy in the ghost region is fixed to the value of the interface cell in the real region (or, in the case of the isobaric fix, the second cell away from the interface). This was found to be inadequate in problems in which heat conduction across the material interface was desired, as the temperature in the ghost region then takes on an unrealistic value. Thus, when modeling problems involving intermaterial heat conduction with the GPR RGFM, the density in the ghost region was fixed by a temperature requirement, rather than an entropy requirement. If the temperatures of materials 1 and 2 were T_1, T_2 at the interface, the temperature in both of their ghost regions was set to $T^{ghost} = \frac{T_1 + T_2}{2}$; a simple, intuitive choice to make.

$p^{ghost} = p^*$. Thus, when using a stiffened gas EOS, the ghost density for both fluids is:

$$\rho^{ghost} = \frac{p^* + p_\infty}{(\gamma - 1) c_v T^{ghost}} \tag{75}$$

Let $K = L$ or $K = R$. To ensure condition (12) is satisfied, the following transformation is required:

$$A_K^* \to \left(\frac{\rho^{ghost}}{\rho_K^*} \right)^{\frac{1}{3}} A_K^* \tag{76}$$

To ensure that $q_1^{ghost} = q_1^*$ after the temperature fix, the following transformation is required:

$$J_K^* \to \frac{T_K^*}{T^{ghost}} J_K^* \tag{77}$$

25

	ρ	p	$\boldsymbol{v}$	A	$\boldsymbol{J}$
$x < 0.5$	1	1	$\boldsymbol{0}$	I_3	$\boldsymbol{0}$
$x \geq 0.5$	0.125	0.1	$\boldsymbol{0}$	$0.5 \cdot I_3$	$\boldsymbol{0}$

Table 1: Initial conditions for the viscous Sod shock tube test

	ρ	p	$\boldsymbol{v}$	A	$\boldsymbol{J}$
$x < 0.5$	1000	7×10^8	$\boldsymbol{0}$	I_3	$\boldsymbol{0}$
$x \geq 0.5$	1000	10^8	$\boldsymbol{0}$	I_3	$\boldsymbol{0}$

Table 2: Initial conditions for the water water interface test

4.1.3 Numerical Results

The GPR RGFM is now assessed. The first three tests in this chapter are standard Riemann problems, exact solutions to which exist for the Euler equations. The viscosity of the GPR model smears the solutions in areas in which the solutions to the Euler equations are discontinuous or not smooth. This smearing is not the result of using a low order solver (all results in these sections being calculated to third order). The last two tests assess the ability of the GPR RGFM to correctly model heat conduction across interfaces, using the temperature fix described in Section 4.1.2.

Viscous Sod Shock Tube The purpose of this test is to ensure that the GPR RGFM can maintain a sharp contact discontinuity in the famous shock tube test of Sod [79]. A viscous ideal gas is used with $\gamma = 1.4$, $\mu = 5 \times 10^{-4}$, $P_r = 2/3$, as in Ren et al. [70]. $c_v = 2.5$, $\rho_0 = 1$, $p_0 = 1$, $c_s = 1$, and $\alpha = 1$. The initial conditions are given in Table 1 on page 26. The final time is $t = 0.2$ and all simulations used 200 cells.

The results in Figure 8 on page 27 without the GPR RGFM match those in [70] well. The viscous smearing in the density and the "bump" in the velocity at the contact discontinuity are present, as investigated by Jameson [50]. When applying the GPR RGFM, the contact discontinuity is now maintained, as it should be, as the gases are assumed to be immiscible. Additionally, the bump in the velocity is no longer present. This is correct, as the bump corresponds to a smearing of the density across the contact discontinuity, which should not occur for immiscible gases.

Water-Water Interface This problem tests the GPR RGFM for the stiffened EOS. The test comprises two volumes of water with different pressures, meeting at $x = 0.5$ (as found in Ghaisas et al. [37], Test III.B.2). The initial conditions are found in Table 2 on page 26. Realistic values are chosen for the material parameters: $\gamma = 4.4$, $p_\infty = 6 \times 10^8$, $c_v = 950$, $\mu = 10^{-3}$, $P_r = 7$, $\rho_0 = 1000$, $T_0 = 300$. c_s and α are taken to be 55 and 500, respectively. The final time is $t = 1.5 \times 10^{-4}$ and all simulations used 200 cells.

The results in Figure 9 on page 28 without the GPR RGFM match those in [37] well. The sharp contact discontinuity is preserved by the GPR RGFM.
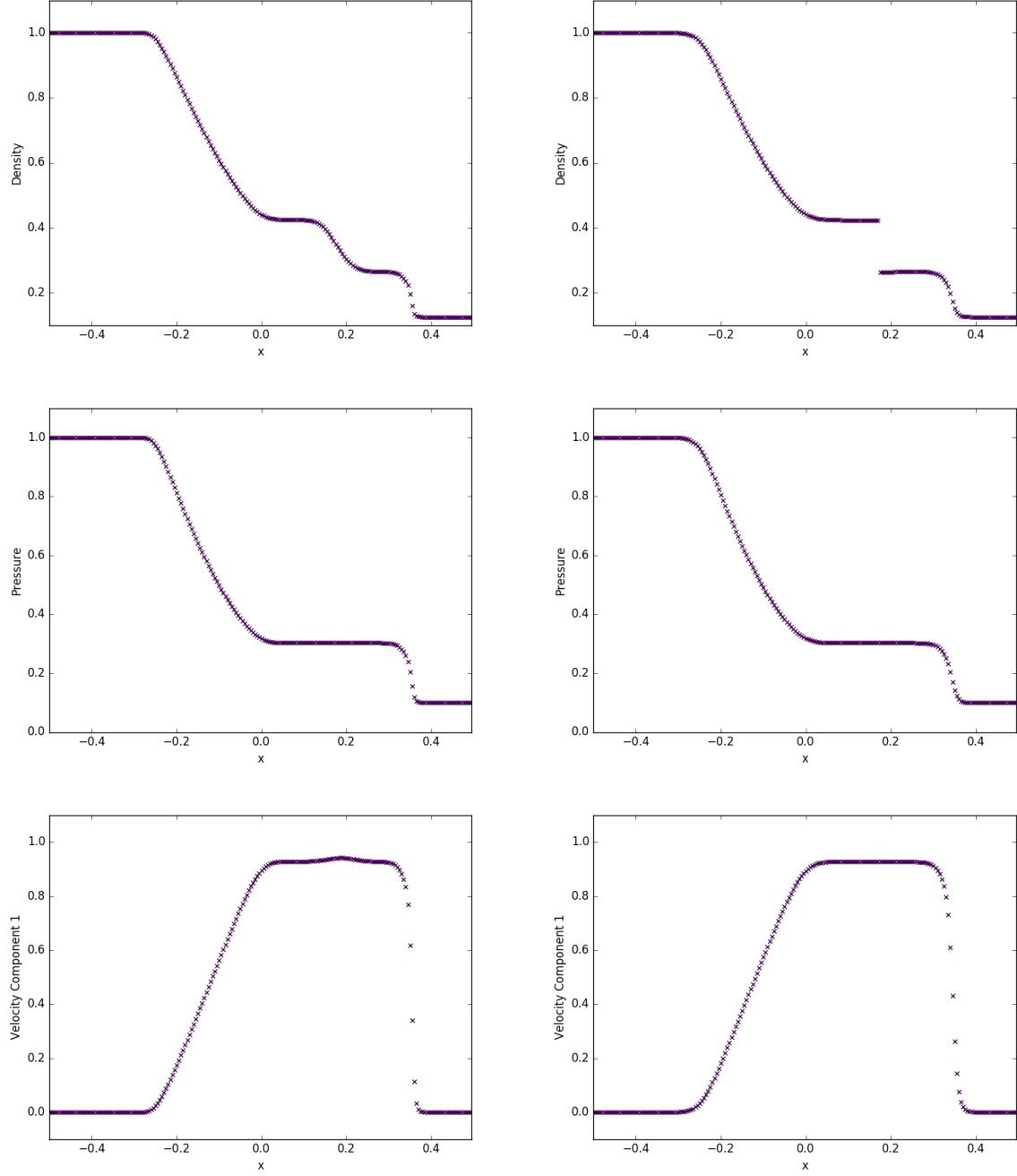
Figure 8: Density, pressure, and velocity for the viscous Sod shock tube test with viscosity $\mu = 5 \times 10^{-4}$ without GPR RGFM (left) / with GPR RGFM (right)
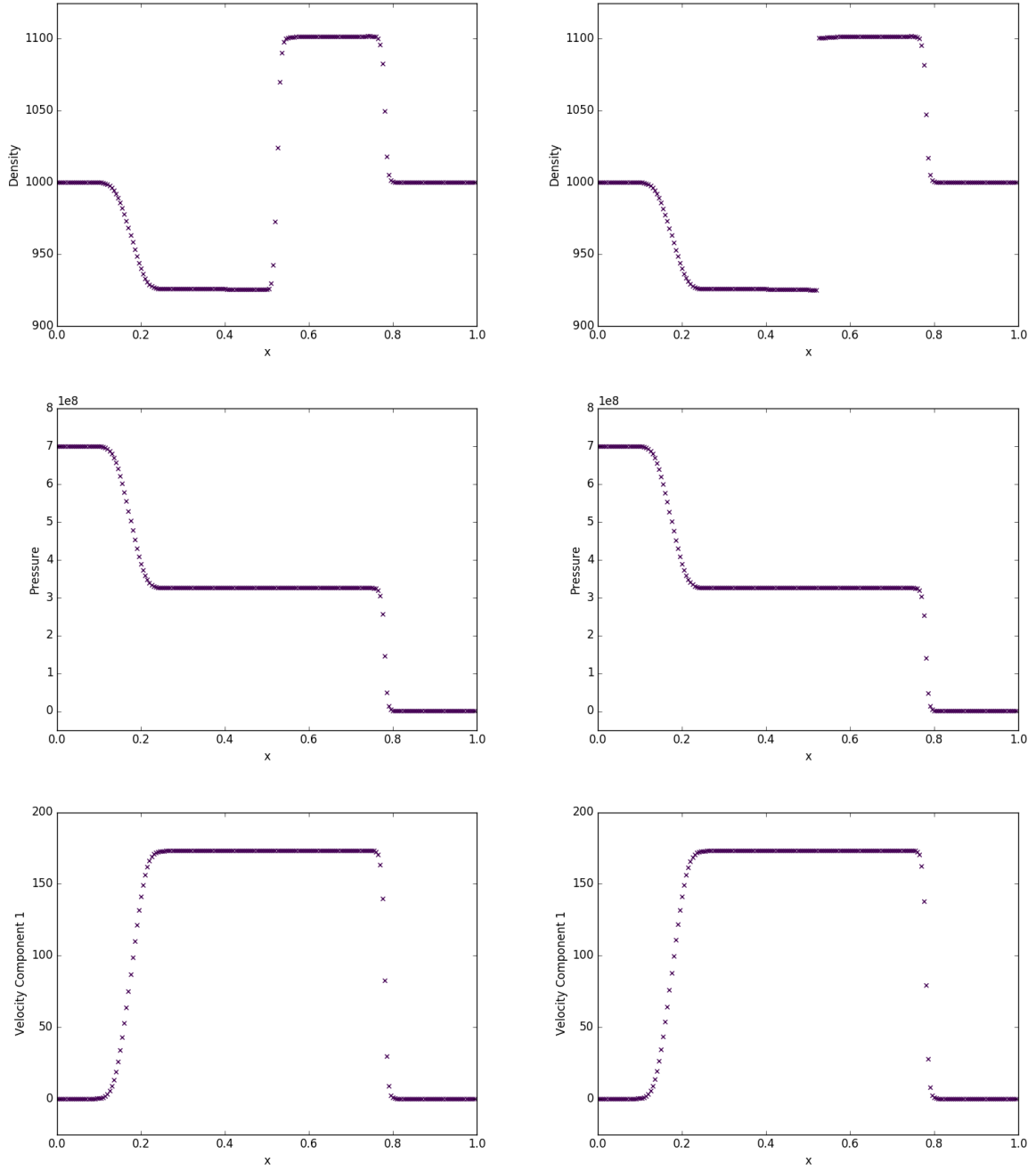
Figure 9: Density, pressure, and velocity for the water water interface test without GPR RGFM (left) / with GPR RGFM (right)

	ρ	p	$\boldsymbol{v}$	A	$\boldsymbol{J}$
$x < 0.05$	1.3333	1.5×10^5	$\left(\begin{array}{ccc} 35.35\sqrt{10} & 0 & 0 \end{array}\right)$	$\left(\frac{1.3333}{1.18}\right)^{\frac{1}{3}} I_3$	$\boldsymbol{0}$
$0.05 \leq x < 0.4$	1	10^5	$\boldsymbol{0}$	$\left(\frac{1}{1.18}\right)^{\frac{1}{3}} I_3$	$\boldsymbol{0}$
$0.4 \leq x < 0.6$	0.1379	10^5	$\boldsymbol{0}$	$\left(\frac{0.1379}{0.163}\right)^{\frac{1}{3}} I_3$	$\boldsymbol{0}$
$0.6 \leq x \leq 1$	1	10^5	$\boldsymbol{0}$	$\left(\frac{1}{1.18}\right)^{\frac{1}{3}} I_3$	$\boldsymbol{0}$

Table 3: Initial conditions for the helium bubble test

Helium Bubble   The interface between two different gases is now modeled. As in Test B of Wang et al. [84], a bubble of helium   surrounded by air   initially occupies the region $x \in [0.4, 0.6]$. A shock front in the air, initially at $x = 0.05$, travels towards the helium bubble. The initial conditions are given in Table 3 on page 29. Realistic material parameters are taken for the helium: $\gamma = 1.66$, $c_v = 3127$, $\rho_0 = 0.163$, $\mu = 1.99 \times 10^{-5}$, $P_r = 0.688$, and for the air: $\gamma = 1.4$, $c_v = 721$, $\rho_0 = 1.18$, $\mu = 1.85 \times 10^{-5}$, $P_r = 0.714$. In both cases, $p_0 = 101325$, $c_s = 55$, and $\alpha = 500$.

200 cells are used. The results for times $t = 7 \times 10^{-4}$ and $t = 14 \times 10^{-4}$ are displayed in Figure 10 on page 30. In the former, the shock is about to hit the helium bubble (corresponding to the region of low density). In the latter, the shock has traveled through the helium bubble, compressing it slightly, and the bubble itself has moved almost 0.1 spatial units to the right. There is good correspondence with the results in [84] and the sharp discontinuity in density is maintained.

Intermaterial Heating-Induced Acoustic Wave   This test is based on that of the Heating Induced Deflagration Test of Jackson & Nikiforakis [49]. The test assesses the ability of the GPR RGFM to conduct heat between two different materials. Take the material parameters for air and helium from Section 4.1.3. Take the scaled spatial variable x^* defined by:

$$x = \frac{\mu^{air} c_0^{air}}{p_0 \gamma^{air}} x^* \tag{78}$$

The domain $x^* \in [0, 90]$ is used. Thermal energy is added at the left boundary at a high power of $\frac{\gamma^{air} p_0 c_0^{air}}{P_r^{air}(\gamma^{air}-1)}$ (around $1.7 \times 10^8 W m^{-2}$). Three scenarios are tested:

1. The domain is filled with air.

2. The domain comprises two volumes of air, initially separated at $x^* = 22.5$.

3. The domain comprises a volume of air (left) and a volume of helium (right), initially separated at $x^* = 22.5$.

The initial conditions for the two gases in all scenarios are given in Table 4 on page 30. The results of the test are shown in Figure 11 on page 32 and Figure 12 on page 33 for various times. The material interface is represented by a dashed vertical line in scenarios 2 and 3. All simulations used 400 cells.
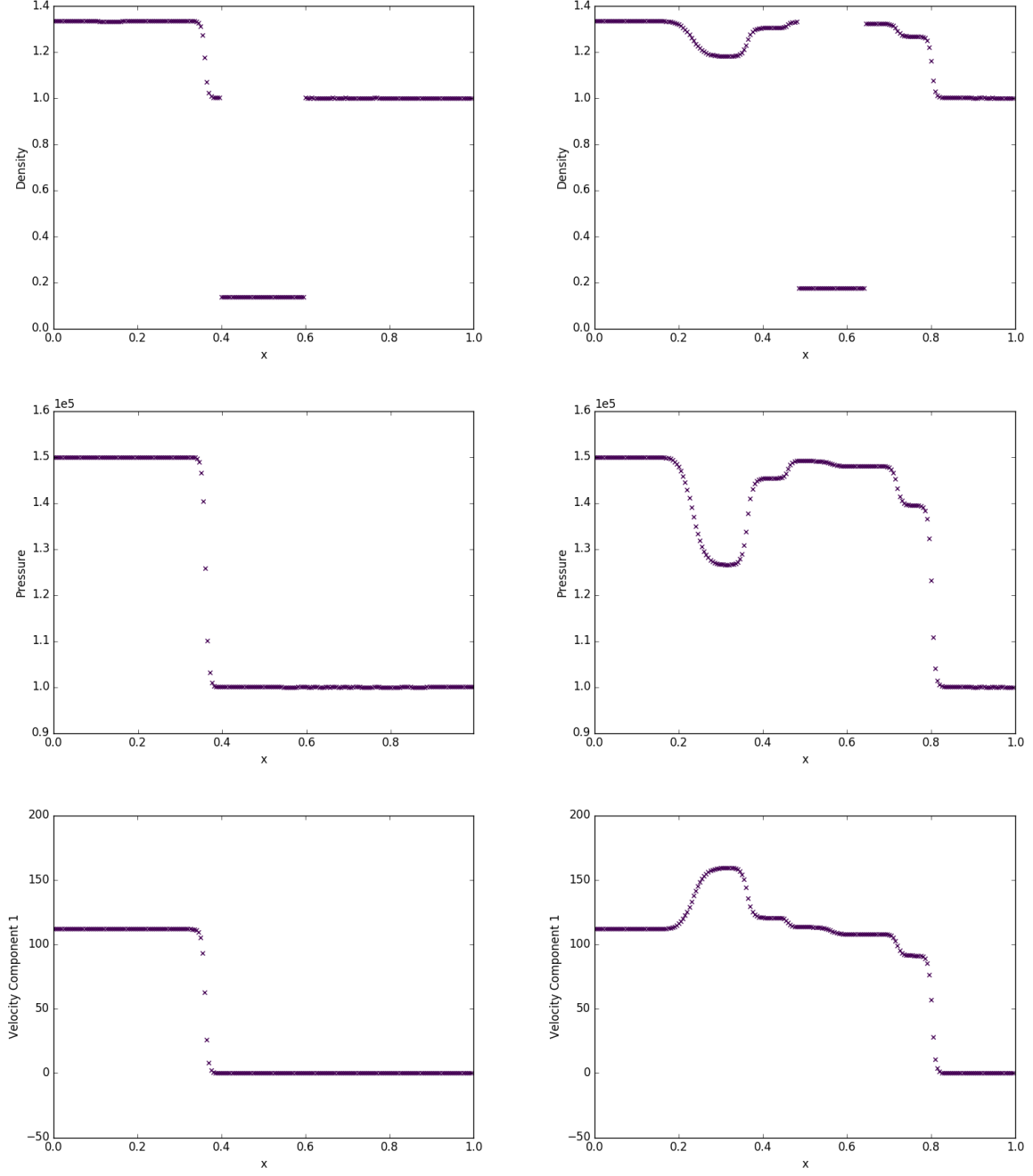
Figure 10: Density, pressure, and velocity for the helium bubble test with GPR RGFM at times $t = 7 \times 10^{-4}$ (left) and $t = 14 \times 10^{-4}$ (right)

	ρ	p	$\boldsymbol{v}$	A	$\boldsymbol{J}$
air	1.18	101325	$\boldsymbol{0}$	I_3	$\boldsymbol{0}$
helium	0.164	101325	$\boldsymbol{0}$	I_3	$\boldsymbol{0}$

Table 4: Initial conditions for the intermaterial heating induced acoustic wave test

Time ($\times 10^{-9}$)	0	1	2	3	4	5
Mass in Scenario 2 ($\times 10^{-6}$)	1.254	1.255	1.253	1.252	1.252	1.253
Mass in Scenario 3 ($\times 10^{-6}$)	1.254	1.253	1.248	1.254	1.255	1.255

Table 5: Mass of the air volume in scenarios 2 and 3 at various times

	ρ	p	$\boldsymbol{v}$	A	$\boldsymbol{J}$
$x < 0$	2	1	$\boldsymbol{0}$	$\sqrt[3]{2} \cdot I_3$	$\boldsymbol{0}$
$x \geq 0$	0.5	1	$\boldsymbol{0}$	$\frac{1}{\sqrt[3]{2}} \cdot I_3$	$\boldsymbol{0}$

Table 6: Initial conditions for the heat conduction test

As the left wall heats up, a temperature gradient develops and the acoustic wave described by Jackson & Nikiforakis [49] appears. The results for scenarios 1 and 2 are indistinguishable, as they should be, and there are no aberrations around the material interface in scenario 2. In scenario 3, the acoustic wave hits the interface at around $t = 2 \times 10^{-9}$ and then speeds up (as it should, the speed of sound in helium being around three times that of air). The heat flux wave increases in intensity after passing into the helium, owing to the fact that the wave is traveling faster. As expected, all variables displayed are continuous across the interface.

In scenarios 2 and 3 the interface moves to the right as the air heats up and expands. The masses of the air volumes in these two scenarios at various times are given in Table 5 on page 31, demonstrating that mass is conserved well as the interface moves.

Intermaterial Heat Conduction This test is based on the Heat Conduction in a Gas Test of Dumbser et al. [27]. Two ideal gases at different temperatures are initially in contact at position $x = 0$. The initial conditions for this problem are given in Table 6 on page 31.

The material parameters are taken to be: $\gamma = 1.4$, $c_v = 2.5$, $\rho_0 = 1$, $p_0 = 1$, $c_s = 1$, $\alpha = 2$, $\mu = 10^{-2}$, $\kappa = 10^{-2}$. An interface is initially placed between the two volumes of air at $x = 0.5$. The final time is taken to be $t = 1$, and 200 cells are used. Results are displayed in Figure 13 on page 34, using the results from [20] as a reference. The material interface is denoted by a dashed vertical line.

The temperature curve generated using the GPR RGFM matches very well the reference solution. The interface has moved to $x = 0.53756$, as is to be expected, as the cooler gas on the left expands as it heats up, and the hotter gas on the right contracts as it cools. Initially, the mass of the left volume is 1 and the right volume is 0.25. At $t = 1$, these masses are 0.9997 and 0.2503, respectively. Thus, mass on either side is conserved to a good approximation. Although the GPR RGFM results for the heat flux match the reference solution well over most of the domain, there are aberrations in a small region around the interface.

The temperature fix is crucial in obtaining these results. Using the traditional entropy fix instead results in a stationary system, with the initial conditions persisting indefinitely. This is because the entropy fix does not allow the system to "see" the temperature difference, meaning that no heat flux is generated across the interface.
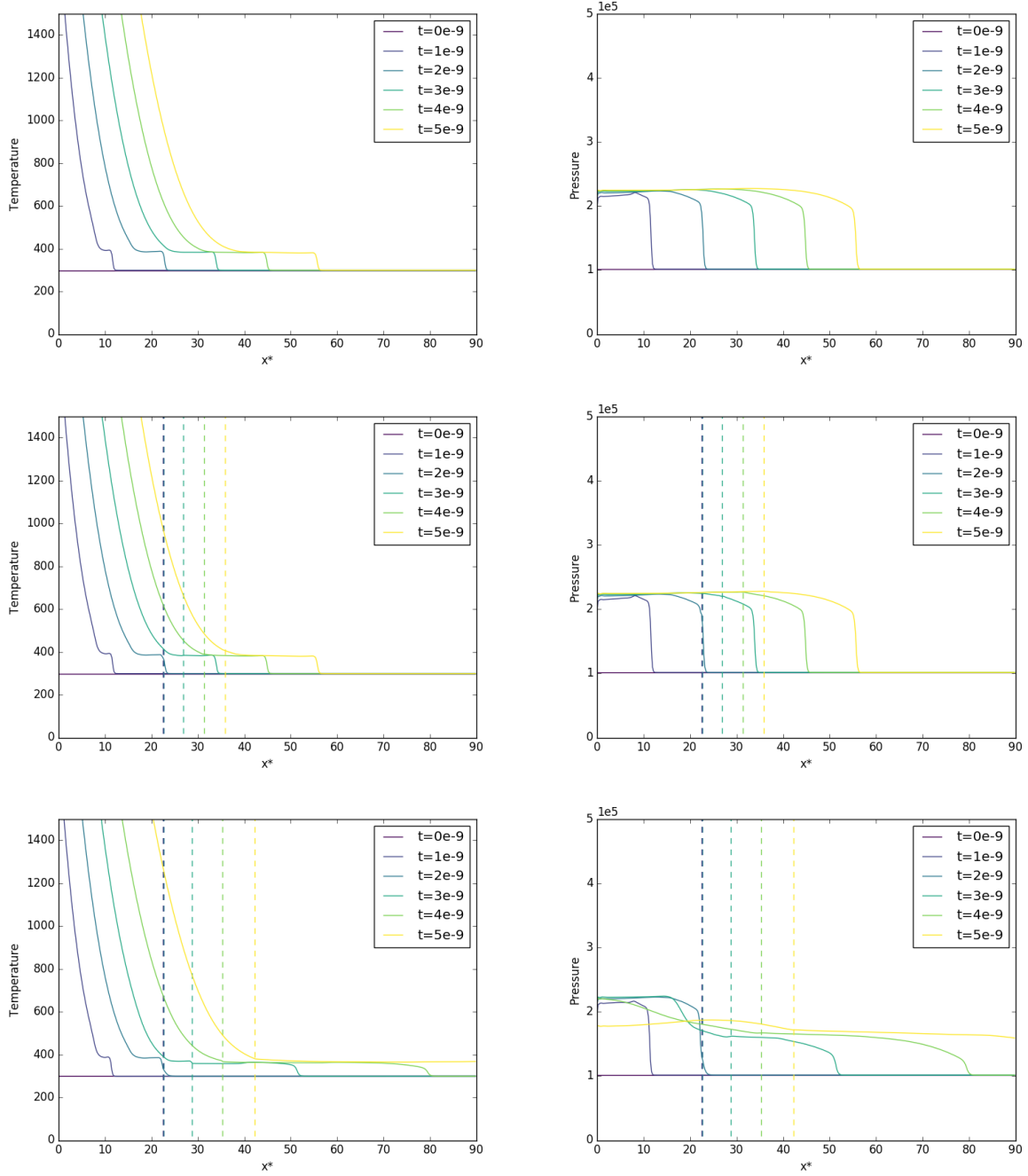
Figure 11: Temperature and pressure for the intermaterial heating induced acoustic wave test with: a single volume of air (top); two volumes of air initially separated at $x^* = 22.5$ (middle); air and helium initially separated at $x^* = 22.5$ (bottom).
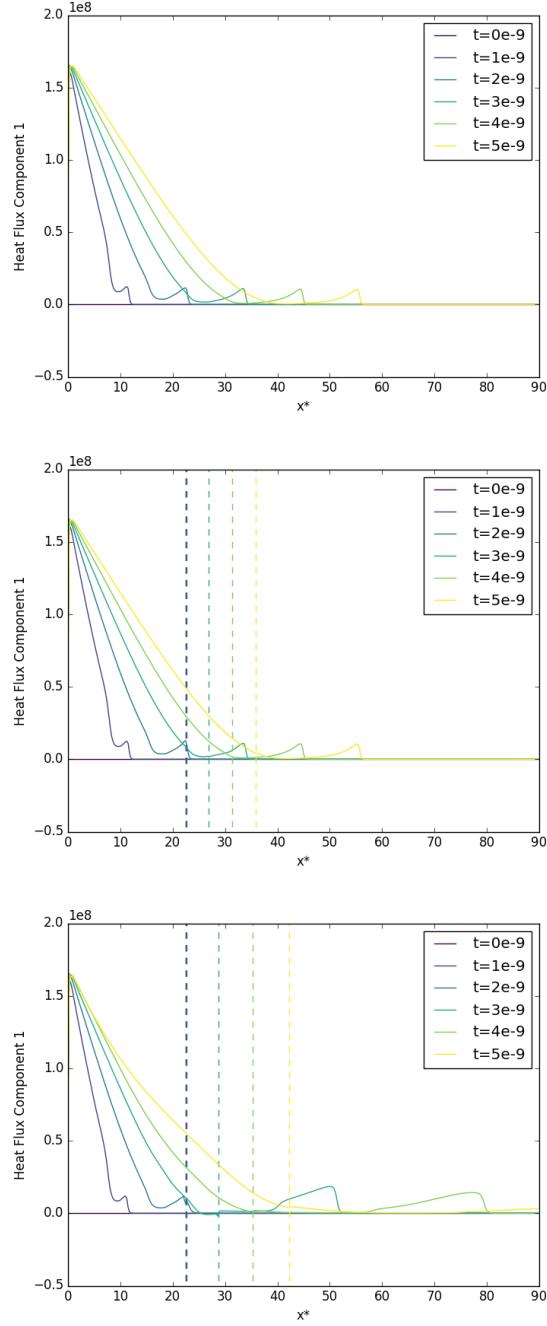
Figure 12: Heat flux for the intermaterial heating induced acoustic wave test with: a single volume of air (top); two volumes of air initially separated at $x^* = 22.5$ (middle); air and helium initially separated at $x^* = 22.5$ (bottom).
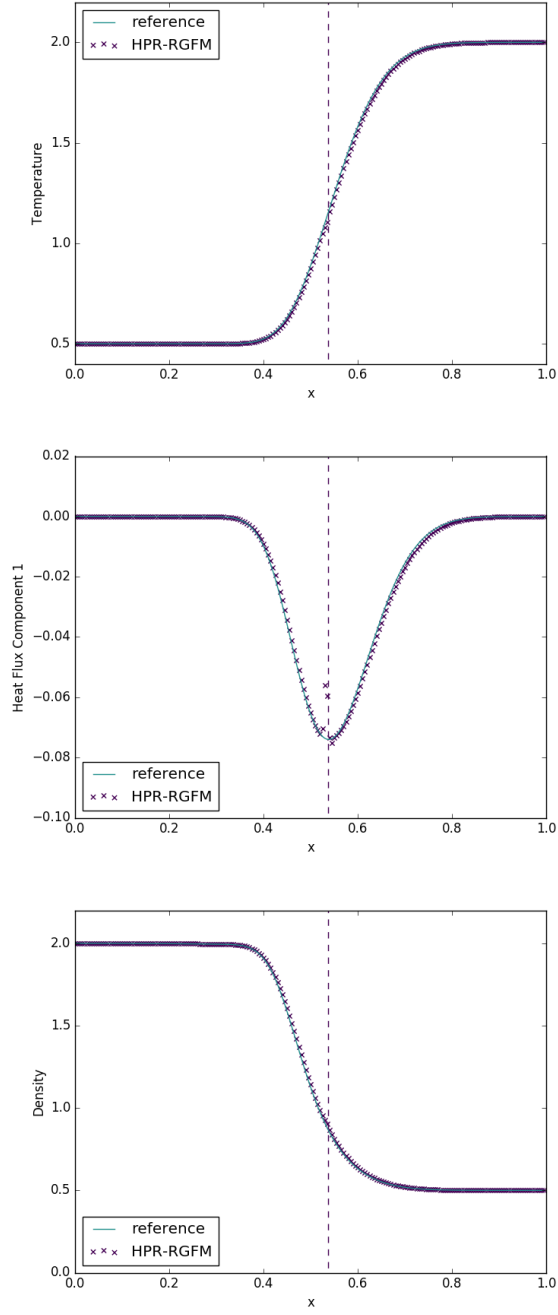
Figure 13: Temperature, heat flux, and density for the intermaterial heat conduction test with GPR RGFM

4.2 Combining the GPR Model with Reactive Models

4.2.1 Modeling Reactive Processes

In this study, when modeling reactive gases, the following equation is introduced alongside (1a), (1b), (1c), (1d), (1e):

$$\frac{\partial\left(\rho\lambda\right)}{\partial t} + \frac{\partial\left(\rho\lambda v_k\right)}{\partial x_k} = -\rho\lambda K\left(T\right) \tag{79}$$

K is the rate of reaction a function of temperature, whose form depends on the type of reaction kinetics used. The EOS (3) is modified to include:

$$E_r\left(\lambda\right) = -Q_c\left(1-\lambda\right) \tag{80}$$

In discrete ignition temperature reaction kinetics, no reaction occurs below the ignition temperature, T_i. Above T_i, the reaction proceeds at a constant rate $K_0 > 0$:

$$K\left(T\right) = \begin{cases} K_0 & T \geq T_i \\ 0 & T < T_i \end{cases} \tag{81}$$

A more sophisticated model of reaction kinetics was devised by Svante Arrhenius in 1889 [5, 4]:

$$K\left(T\right) = B_c e^{-E_a/(R_c T)} \tag{82}$$

where B_c is some pre exponential (with units of frequency), and E_a is the activation energy of the reactive species. Often, the system is characterized by the dimensionless inverse activation energy:

$$\epsilon = \frac{R_c T_0}{E_a} \tag{83}$$

4.2.2 Numerical Results

Viscous Shock-Induced Detonation   The GPR model is now combined with discrete ignition tempera ture reaction kinetics to model a ZND detonation wave[4] in a viscous, reactive, ideal gas. There is currently

---

[4]Zel'dovich [85], von Neumann [83], and Döring [18] independently proposed this detonation model, whereby reactive gas is compressed to high pressure by an infinitely thin shock wave into a *von Neumann spike*, initiating the reaction. The reaction zone is located behind the spike. In the reference frame of the shock, the gas moves supersonically ahead of the shock, subsonically in the reaction zone, and sonically in the region behind the reaction zone (which is described by the Chapman Jouget state [12, 54]. The energy released in the reaction is transported acoustically to the shock to support it.

no published work in which the GPR model is integrated with a combustion model, and this test case serves to demonstrate that this combination reproduces well established results.

The test consists of a Chapman Jouget wave with speed 1, traveling into a region of totally unburnt gas. The initial conditions are taken from Helzel et al. [42]. On $x < 0.25$ we have $\rho = 1.4$, $p = 1$, $\boldsymbol{v} = \boldsymbol{0}$, $A = \sqrt[3]{1.4} \cdot I_3$, $\boldsymbol{J} = \boldsymbol{0}$, $\lambda = 0$. On $x \geq 0.25$ we have $\rho = 0.887565$, $p = 0.191709$, $\boldsymbol{v} = (-0.577350, 0, 0)$, $A = \sqrt[3]{0.887565} \cdot I_3$, $\boldsymbol{J} = \boldsymbol{0}$, $\lambda = 1$.

The material parameters are taken to be: $\gamma = 1.4$, $c_v = 2.5$, $\rho_0 = 1$, $p_0 = 1$, $c_s = 1$, $\alpha = 1$, $\mu = 10^{-4}$, $P_r = 0.75$, $Q_c = 1$, $K_0 = 250$, $T_i = 0.25$. The results for grids of 400 and 1600 cells at time $t = 0.5$ are found in Figure 14 on page 37. They are to be compared with those by Hidalgo and Dumbser [43]. The simulation with 400 cells corresponds well with that found in [43], and the simulation with 1600 cells is very close to Hidalgo's total variation diminishing reference solution calculated with 10,000 cells.

The von Neumann spike is well resolved, with the thin reaction zone behind it (corresponding to the region in which the concentration decreases from 1 to 0). The CJ state is maintained correctly behind the reaction zone. The spurious wave in the density is explained in [43] as being due to initialization errors occurring as a result of using exact algebraic conditions for an ideal (infinitely thin) CJ detonation wave, which are solved with a viscous model with finite reaction rate.

Heating-Induced Deflagration   As a step towards modeling the slow cooking off problem, the GPR model is now applied to the situation presented by Clarke, Kassoy and Riley [14, 15, 16]. Here, the domain $x \in \left[0, 8.5 \times 10^{-6}\right]$ is occupied by an ideal gas with initial conditions $\rho = \rho_0 = 1.176$, $p = p_0 = 101325$, $\boldsymbol{v} = \boldsymbol{0}$, $A = I_3$, $\boldsymbol{J} = \boldsymbol{0}$ and material parameters $\gamma = 1.4$, $c_v = 718$, $c_s = 55$, $\alpha = 500$, $\mu = 1.98 \times 10^{-5}$, $P_r = 0.72$. These values are chosen to be similar to air at room temperature.

Thermal energy is added at the left boundary at a high power of $\frac{\gamma p_0 c_0}{P_r(\gamma - 1)}$ (around $1.7 \times 10^8 W m^{-2}$). The test is performed with both a combustible and an inert gas. In the former case, the initial concentration is set to $\lambda = 1$. Arrhenius reaction kinetics are used, with $Q_c = 6\gamma c_v T_0$, $B_c = 7 \times 10^{10}$, $\epsilon = \frac{1}{20}$. The subsequent evolutions of the systems for 400 cells are shown in Figure 15 on page 38. Nondimensionalized time and length variables t^*, x^* are used, as in [15]:

$$t = \frac{\mu}{p_0 \gamma} t^* \tag{84a}$$

$$x = \frac{\mu c_0}{p_0 \gamma} x^* \tag{84b}$$

There are no analogues for α and c_s in the models used by Clarke et al. c_s is given the experimentally derived value for CH_3Cl at 30˚C given in [27]. α is chosen so that the GPR results corresponded with those in [15]. The results presented here are thus close, but not identical to those of Clarke et al.

Note that heating the inert gas produces an acoustic wave of constant pressure, propagating ahead of the temperature curve. This pressure wave is also present in the heating of the combustible gas, where it proceeds
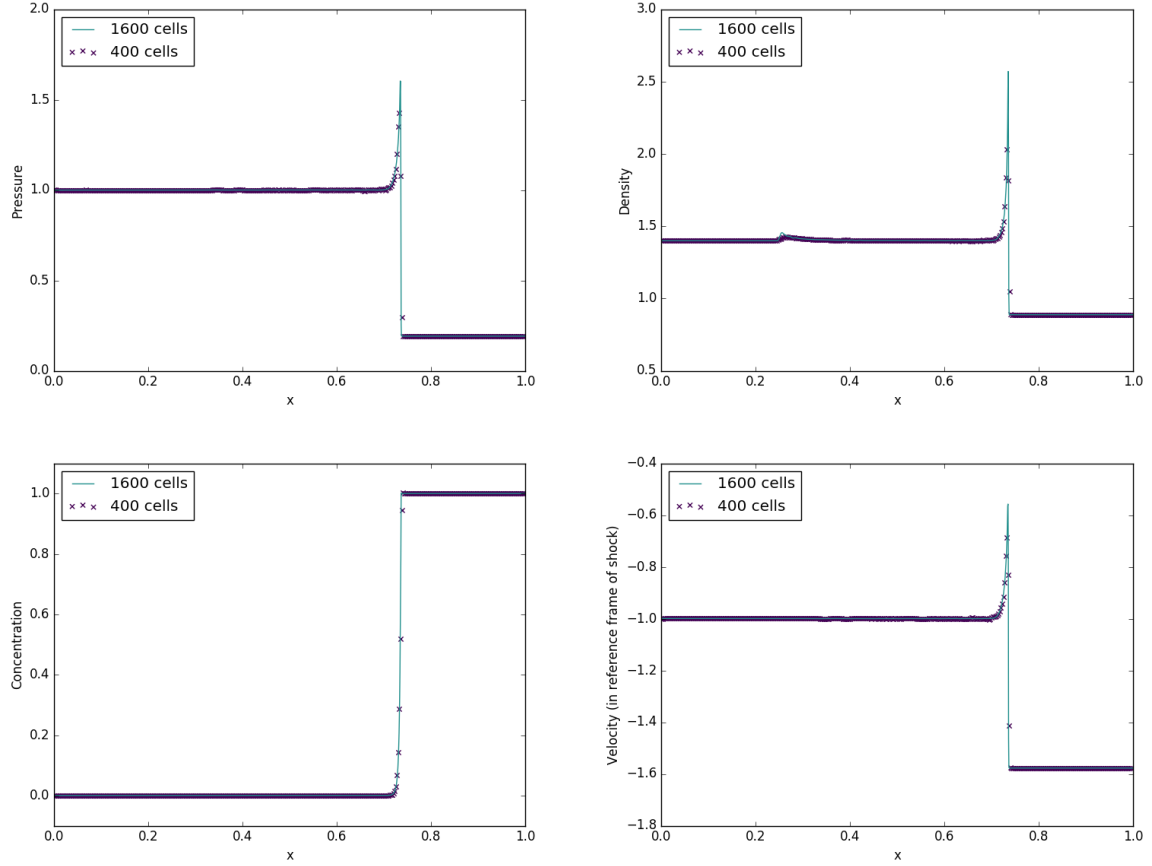
Figure 14: Pressure, density, concentration of reactant, and velocity (in the reference frame of the shock) in the viscous shock induced detonation test

in front of the combustion wave. The temperature increase accompanying this acoustic wave is not enough to ignite the reactive gas, and the thin reaction zone lags behind the acoustic wavefront. Although the combustion wave is referred to as a detonation wave in [15], it would now commonly be called a deflagration wave, as it travels subsonically and is not coincident with the shock wave. This phenomenon of a second, faster shock overtaking the combustion wave demonstrated experimentally by Kapila et al. [55], with a full mathematical analysis provided by Short [78], where it is shown to result from the steep temperature gradient at the time of ignition.

Heating-Induced Detonation   It is now demonstrated that the heating induced deflagration test can result in detonation if the temperature gradient upon ignition is less steep. This test is identical to the previous test, with one exception: ϵ is given the higher value of $\frac{1}{15}$. Thus, the activation energy is effectively lower, or equivalently, the whole gas volume is relatively closer to the ignition temperature when the gas at the left boundary ignites. The results of this test are shown in Figure 16 on page 40.

The von Neumann spike is present and well resolved, with a thin reaction zone appearing behind it in the concentration plot. Unlike in Section 4.2.2, the system does not relax to the CJ state behind the detonation

37
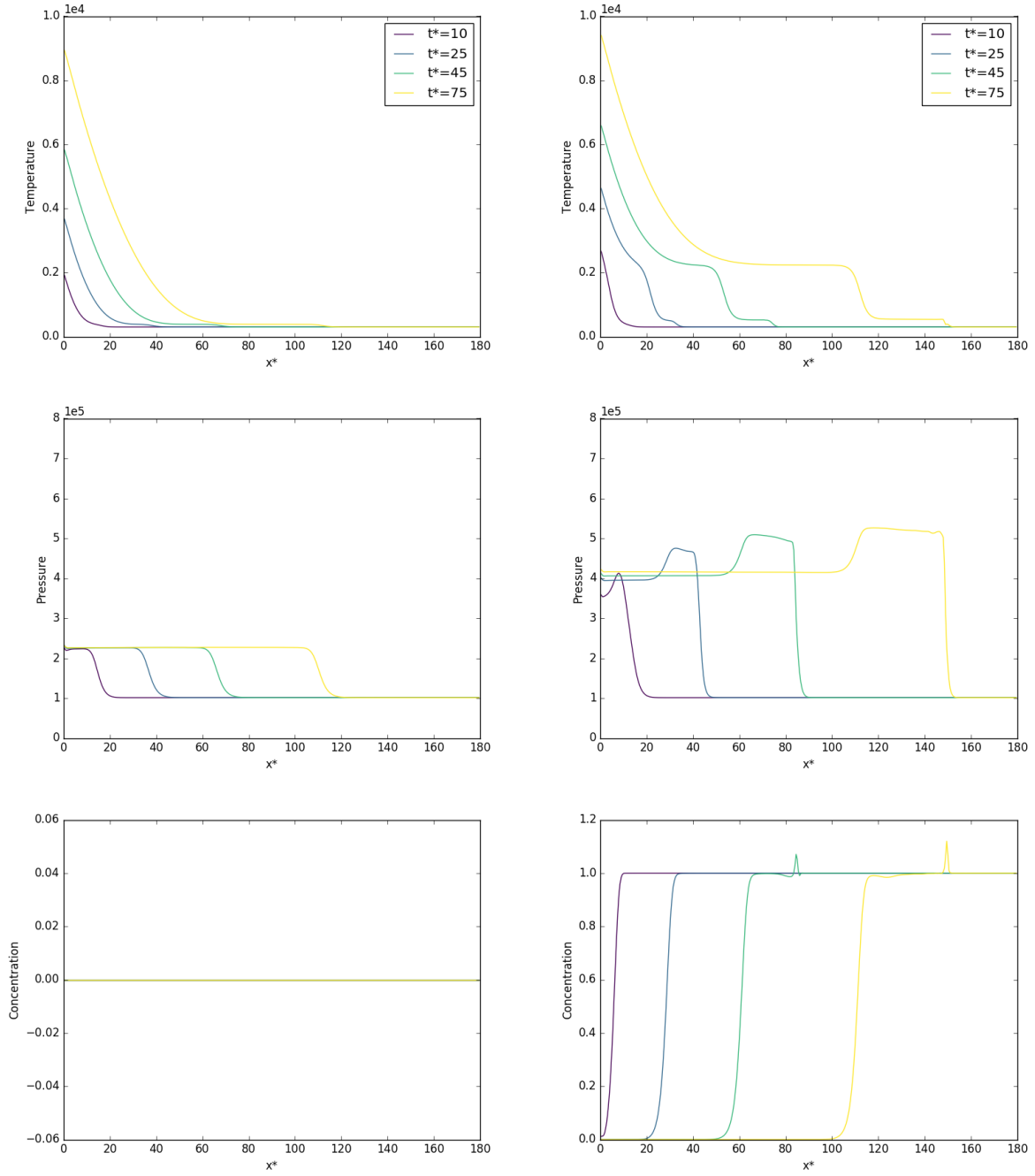
Figure 15: Temperature, pressure, and concentration of reactant in the heating induced deflagration test with inert gas (left) / reactive gas (right)

wave, as thermal energy is continually added to the reflective left boundary. The region behind the reaction zone is thus complex.

4.3 New Numerical Methods: Operator Splitting

Note that (1a), (1b), (1c), (1d), (1e) can be written in the following form:

$$\frac{\partial \boldsymbol{Q}}{\partial t} + \boldsymbol{\nabla} \cdot \boldsymbol{F}(\boldsymbol{Q}) + \boldsymbol{B}(\boldsymbol{Q}) \cdot \nabla \boldsymbol{Q} = \boldsymbol{S}(\boldsymbol{Q}) \tag{85}$$

As described in [82], a viable way to solve inhomogeneous systems of PDEs is to employ an operator splitting. That is, the following subsystems are solved:

$$\frac{\partial \boldsymbol{Q}}{\partial t} + \boldsymbol{\nabla} \cdot \boldsymbol{F}(\boldsymbol{Q}) + \boldsymbol{B}(\boldsymbol{Q}) \cdot \nabla \boldsymbol{Q} = \boldsymbol{0} \tag{86a}$$

$$\frac{d\boldsymbol{Q}}{dt} = \boldsymbol{S}(\boldsymbol{Q}) \tag{86b}$$

The advantage of this approach is that specialized solvers can be employed to compute the results of the different subsystems. Let $H^{\delta t}, S^{\delta t}$ be the operators that take data $\boldsymbol{Q}(x, t)$ to $\boldsymbol{Q}(x, t + \delta t)$ under systems (86a) and (86b) respectively. A second order scheme (in time) for solving the full set of PDEs over time step $[0, \Delta t]$ is obtained by calculating $\boldsymbol{Q}_{\boldsymbol{\Delta t}}$ using a Strang splitting:

$$\boldsymbol{Q}_{\boldsymbol{\Delta t}} = S^{\frac{\Delta t}{2}} H^{\Delta t} S^{\frac{\Delta t}{2}} \boldsymbol{Q_0} \tag{87}$$

In the scheme proposed here, the homogeneous subsystem will be solved using a WENO reconstruction of the data, followed by a finite volume update, and the temporal ODEs will be solved with appropriate ODE solvers. This new scheme will be referred to here as *the Split WENO method*.

4.3.1 The Homogeneous System

A WENO reconstruction of the cell averaged data is performed at the start of the time step (as described in 2.4). Focusing on a single cell C_i at time t_n, we have $\boldsymbol{w^n}(\boldsymbol{x}) = \boldsymbol{w^n}_p \Psi_p(\boldsymbol{\chi}(\boldsymbol{x}))$ in C_i where Ψ_p is a tensor product of basis functions in each of the spatial dimensions. The flux in C is approximated by $\boldsymbol{F}(\boldsymbol{x}) \approx \boldsymbol{F}(\boldsymbol{w}_p) \Psi_p(\boldsymbol{\chi}(\boldsymbol{x}))$. $\boldsymbol{w}_p$ are stepped forwards half a time step using the update formula:

$$\frac{\boldsymbol{w_p^{n+\frac{1}{2}}} - \boldsymbol{w_p^n}}{\Delta t/2} + \boldsymbol{F}(\boldsymbol{w_k^n}) \cdot \nabla \Psi_k(\boldsymbol{\chi_p}) + \boldsymbol{B}(\boldsymbol{w_p^n}) \cdot (\boldsymbol{w_k^n} \nabla \Psi_k(\boldsymbol{\chi_p})) = \boldsymbol{0} \tag{88}$$
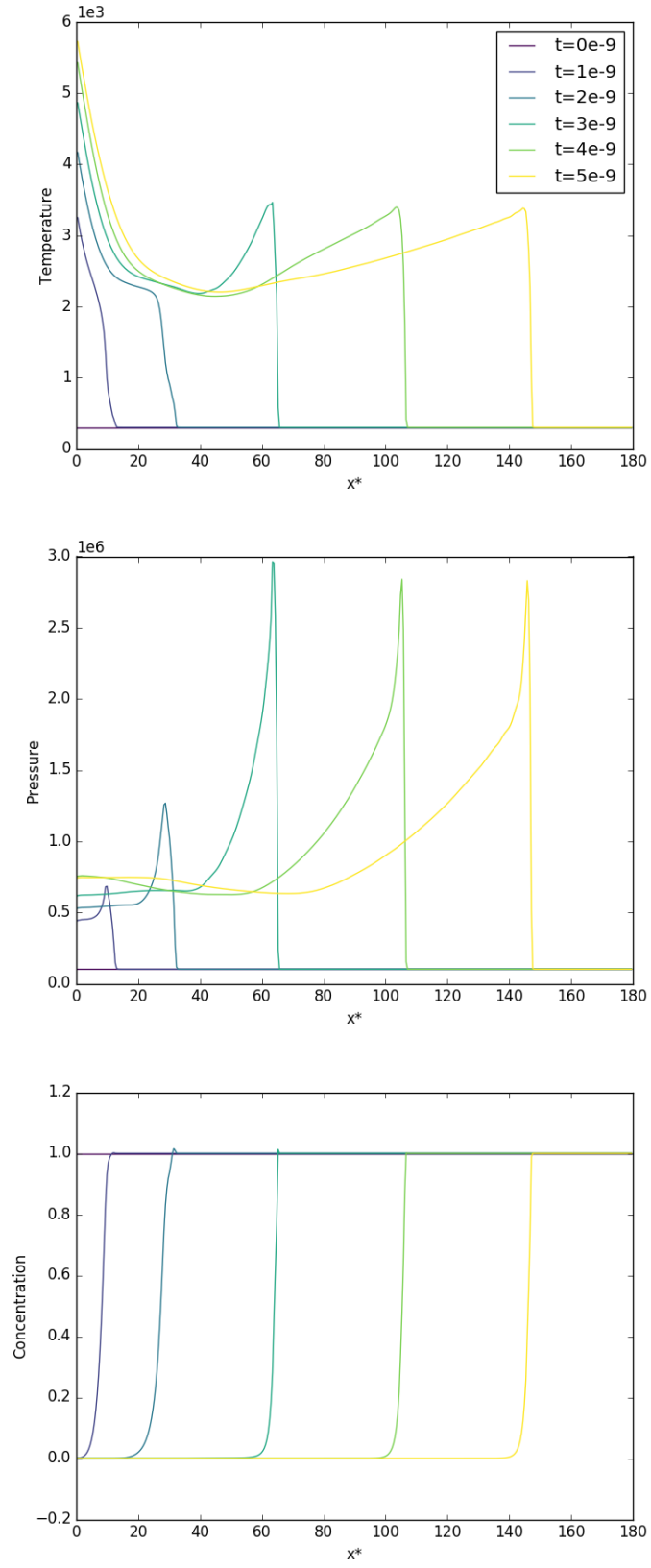
Figure 16: Temperature, pressure, and concentration of reactant in the heating induced detonation test

i.e.

$$w_{\boldsymbol{p}}^{n+\frac{1}{2}} = w_{\boldsymbol{p}}^{n} - \frac{\Delta t}{2\Delta x} \left(\boldsymbol{F}\left(w_{\boldsymbol{k}}^{n}\right) \cdot \nabla \Psi_k \left(\boldsymbol{\chi_p}\right) + \boldsymbol{B}\left(w_{\boldsymbol{p}}^{n}\right) \cdot \left(w_{\boldsymbol{k}}^{n} \nabla \Psi_k \left(\boldsymbol{\chi_p}\right)\right) \right) \tag{89}$$

where $\boldsymbol{\chi_p}$ is the node corresponding to Ψ_p. This evolution to the middle of the time step is similar to that used in the second order MUSCL and SLIC schemes (see [82]) and, as with those schemes, it is integral to giving the method presented here its second order accuracy.

Integrating (86a) over C gives:

$$\boldsymbol{Q}_i^{n+1} = \boldsymbol{Q}_i^n - \Delta t_n \left(\boldsymbol{P}_i^{n+\frac{1}{2}} + \boldsymbol{D}_i^{n+\frac{1}{2}} \right) \tag{90}$$

where

$$\boldsymbol{Q}_i^n = \frac{1}{V} \int_C \boldsymbol{Q}\left(\boldsymbol{x}, t_n\right) d\boldsymbol{x} \tag{91a}$$

$$\boldsymbol{P}_i^{n+\frac{1}{2}} = \frac{1}{V} \int_C \boldsymbol{B}\left(\boldsymbol{Q}\left(\boldsymbol{x}, t_{n+\frac{1}{2}}\right)\right) \cdot \nabla \boldsymbol{Q}\left(\boldsymbol{x}, t_{n+\frac{1}{2}}\right) d\boldsymbol{x} \tag{91b}$$

$$\boldsymbol{D}_i^{n+\frac{1}{2}} = \frac{1}{V} \oint_{\partial C} \boldsymbol{\mathcal{D}}\left(\boldsymbol{Q}^-\left(\boldsymbol{s}, t_{n+\frac{1}{2}}\right), \boldsymbol{Q}^+\left(\boldsymbol{s}, t_{n+\frac{1}{2}}\right)\right) d\boldsymbol{s} \tag{91c}$$

where V is the volume of C and $\boldsymbol{Q}^-, \boldsymbol{Q}^+$ are the interior and exterior extrapolated states at the boundary of C, respectively.

Note that (86a) can be rewritten as:

$$\frac{\partial \boldsymbol{Q}}{\partial t} + \boldsymbol{M}\left(\boldsymbol{Q}\right) \cdot \nabla \boldsymbol{Q} = \boldsymbol{0} \tag{92}$$

where $\boldsymbol{M} = \frac{\partial \boldsymbol{F}}{\partial \boldsymbol{Q}} + \boldsymbol{B}$. Let $\boldsymbol{n}$ be the normal to the boundary at point $\boldsymbol{s} \in \partial C$. For the GPR model, $\hat{M} = \boldsymbol{M}\left(\boldsymbol{Q}\left(\boldsymbol{s}\right)\right) \cdot \boldsymbol{n}$ is a diagonalizable matrix with decomposition $\hat{M} = \hat{R}\hat{\Lambda}\hat{R}^{-1}$ where the columns of $\hat{R}$ are the right eigenvectors and $\hat{\Lambda}$ is the diagonal matrix of eigenvalues. Define also $\hat{\boldsymbol{F}} = \boldsymbol{F} \cdot \boldsymbol{n}$ and $\hat{B} = \boldsymbol{B} \cdot \boldsymbol{n}$. Using these definitions, the interface terms arising in the FV formula have the following form:

$$\boldsymbol{\mathcal{D}}\left(\boldsymbol{Q}^-, \boldsymbol{Q}^+\right) = \frac{1}{2} \left(\hat{\boldsymbol{F}}\left(\boldsymbol{Q}^+\right) + \hat{\boldsymbol{F}}\left(\boldsymbol{Q}^-\right) + \tilde{B}\left(\boldsymbol{Q}^+ - \boldsymbol{Q}^-\right) + \tilde{M}\left(\boldsymbol{Q}^+ - \boldsymbol{Q}^-\right) \right) \tag{93}$$

$\tilde{M}$ is chosen to either correspond to a Rusanov/Lax Friedrichs flux (see [82]):

$$\tilde{M} = \max \left(\max \left| \hat{\Lambda}\left(\boldsymbol{Q}^+\right) \right|, \max \left| \hat{\Lambda}\left(\boldsymbol{Q}^-\right) \right| \right) \tag{94}$$

41

or a simplified Osher–Solomon flux (see [30, 31]):

$$\tilde{M} = \int_0^1 \left| \hat{M} \left(\boldsymbol{Q}^- + z \left(\boldsymbol{Q}^+ - \boldsymbol{Q}^- \right) \right) \right| dz \tag{95}$$

where

$$\left| \hat{M} \right| = \hat{R} \left| \hat{\Lambda} \right| \hat{R}^{-1} \tag{96}$$

$\tilde{B}$ takes the following form:

$$\tilde{B} = \int_0^1 \hat{B} \left(\boldsymbol{Q}^- + z \left(\boldsymbol{Q}^+ - \boldsymbol{Q}^- \right) \right) dz \tag{97}$$

It was found that the Osher Solomon flux would often produce slightly less diffusive results, but that it was more computationally expensive, and also had a greater tendency to introduce numerical artefacts.

$\boldsymbol{P}_{\boldsymbol{i}}^{n+\frac{1}{2}}, \boldsymbol{D}_{\boldsymbol{i}}^{n+\frac{1}{2}}$ are calculated using an $N+1$ point Gauss Legendre quadrature, replacing $\boldsymbol{Q}\left(\boldsymbol{x}, t_{n+\frac{1}{2}}\right)$ with $\boldsymbol{w}^{n+\frac{1}{2}}\left(\boldsymbol{x}\right)$.

4.3.2   The Temporal ODEs

Noting that $\frac{d\rho}{dt} = 0$ over the ODE time step, the operator S entails solving the following systems:

$$\frac{dA}{dt} = \frac{-3}{\tau_1} \left| A \right|^{\frac{5}{3}} A \operatorname{dev}(G) \tag{98a}$$

$$\frac{d\boldsymbol{J}}{dt} = -\frac{1}{\tau_2} \frac{T\rho_0}{T_0\rho} \boldsymbol{J} \tag{98b}$$

These systems can be solved concurrently with a stiff ODE solver. The Jacobians of these two systems to be used in an ODE solver are given in 6.2 and 6.3. However, these systems can also be solved separately, using the analytical results presented in the following sections, under specific assumptions. The second order Strang splitting is then:

$$\boldsymbol{Q_{\Delta t}} = D^{\frac{\Delta t}{2}} T^{\frac{\Delta t}{2}} H^{\Delta t} T^{\frac{\Delta t}{2}} D^{\frac{\Delta t}{2}} \boldsymbol{Q_0} \tag{99}$$

where $D^{\delta t}, T^{\delta t}$ are the operators solving the distortion and thermal impulse ODEs respectively, over timestep δt. This allows us to bypass the relatively computationally costly process of solving these systems numerically.

The Thermal Impulse ODEs Taking the EOS for the GPR model (3) and denoting by $E_2^{(A)}, E_2^{(J)}$ the components of E_2 depending on A and J respectively, we have:

$$
\begin{aligned}
T &= \frac{E_1}{c_v} \\
&= \frac{E - E_2^{(A)}(A) - E_3(\boldsymbol{v})}{c_v} - \frac{1}{c_v} E_2^{(J)}(\boldsymbol{J}) \\
&= c_1 - c_2 \|\boldsymbol{J}\|^2
\end{aligned}
\tag{100}
$$

where:

$$
c_1 = \frac{E - E_2^{(A)}(A) - E_3(\boldsymbol{v})}{c_v} \tag{101a}
$$

$$
c_2 = \frac{\alpha^2}{2c_v} \tag{101b}
$$

Over the time period of the ODE (98b), $c_1, c_2 > 0$ are constant. We have:

$$
\frac{dJ_i}{dt} = -\left(\frac{1}{\tau_2} \frac{\rho_0}{T_0 \rho}\right) J_i \left(c_1 - c_2 \|\boldsymbol{J}\|^2\right) \tag{102}
$$

Therefore:

$$
\frac{d}{dt}\left(J_i^2\right) = J_i^2 \left(-a + b\left(J_1^2 + J_2^2 + J_3^2\right)\right) \tag{103}
$$

where

$$
a = \frac{2\rho_0}{\tau_2 T_0 \rho c_v}\left(E - E_2^{(A)}(A) - E_3(\boldsymbol{v})\right) \tag{104a}
$$

$$
b = \frac{\rho_0 \alpha^2}{\tau_2 T_0 \rho c_v} \tag{104b}
$$

Note that this is a generalized Lotka Volterra system in $\left\{J_1^2, J_2^2, J_3^2\right\}$. It has the following analytical solution:

$$
\boldsymbol{J}(t) = \boldsymbol{J}(0)\sqrt{\frac{1}{e^{at} - \frac{b}{a}\left(e^{at} - 1\right)\|\boldsymbol{J}(0)\|^2}} \tag{105}
$$

The Distortion ODEs Let $k_0 = \frac{3}{\tau_1} \left(\frac{\rho}{\rho_0} \right)^{\frac{5}{3}} > 0$ and let A have singular value decomposition $U\Sigma V^T$. Then:

$$G = \left(U\Sigma V^T \right)^T U\Sigma V^T = V\Sigma^2 V^T \tag{106}$$

$$\mathrm{tr}\,(G) = \mathrm{tr}\left(V\Sigma^2 V^T \right) = \mathrm{tr}\left(\Sigma^2 V^T V \right) = \mathrm{tr}\left(\Sigma^2 \right) \tag{107}$$

Therefore:

$$\begin{aligned}
\frac{dA}{dt} &= -k_0 U\Sigma V^T \left(V\Sigma^2 V^T - \frac{\mathrm{tr}\left(\Sigma^2 \right)}{3} I \right) \\
&= -k_0 U\Sigma \left(\Sigma^2 - \frac{\mathrm{tr}\left(\Sigma^2 \right)}{3} \right) V^T \\
&= -k_0 U\Sigma\,\mathrm{dev}\left(\Sigma^2 \right) V^T
\end{aligned} \tag{108}$$

It is a common result (see [38]) that:

$$d\Sigma = U^T dA V \tag{109}$$

and thus:

$$\frac{d\Sigma}{dt} = -k_0 \Sigma\,\mathrm{dev}\left(\Sigma^2 \right) \tag{110}$$

Using a fast 3×3 SVD algorithm (such as in [61]), U, V, Σ can be obtained, after which the following procedure is applied to Σ, giving $A(t) = U\Sigma(t)V^T$.

Denote the singular values of A by a_1, a_2, a_3. Then:

$$\Sigma\,\mathrm{dev}\left(\Sigma^2 \right) = \begin{pmatrix} a_1 \left(a_1^2 - \frac{a_1^2 + a_2^2 + a_3^2}{3} \right) & 0 & 0 \\ 0 & a_1 \left(a_1^2 - \frac{a_1^2 + a_2^2 + a_3^2}{3} \right) & 0 \\ 0 & 0 & a_1 \left(a_1^2 - \frac{a_1^2 + a_2^2 + a_3^2}{3} \right) \end{pmatrix} \tag{111}$$

Letting $x_i = \frac{a_i^2}{\det(A)^{\frac{2}{3}}} = \frac{a_i^2}{\left(\frac{\rho}{\rho_0} \right)^{\frac{2}{3}}}$ we have:

$$\frac{dx_i}{d\tau} = -3x_i \left(x_i - \bar{x} \right) \tag{112}$$

44

where $\tau = \frac{2}{\tau_1} \left(\frac{\rho}{\rho_0} \right)^{\frac{7}{3}} t$ and $\bar{x}$ is the arithmetic mean of x_1, x_2, x_3. This ODE system travels along the surface $\Psi = \{x_1, x_2, x_3 > 0, x_1 x_2 x_3 = 1\}$ to the point $x_1, x_2, x_3 = 1$. This surface is symmetrical in the planes $x_1 = x_2$, $x_1 = x_3$, $x_2 = x_3$. As such, given that the system is autonomous, the paths of evolution of the x_i cannot cross the intersections of these planes with Ψ. Thus, any non strict inequality of the form $x_i \geq x_j \geq x_k$ is maintained for the whole history of the system. By considering (112) it is clear that in this case x_i is monotone decreasing, x_k is monotone increasing, and the time derivative of x_j may switch sign.

Note that we have:

$$\begin{cases} \frac{dx_i}{d\tau} = -x_i \left(2x_i - x_j - x_k \right) = -x_i \left(2x_i - x_j - \frac{1}{x_i x_j} \right) \\ \frac{dx_j}{d\tau} = -x_j \left(2x_j - x_k - x_i \right) = -x_j \left(2x_j - x_i - \frac{1}{x_i x_j} \right) \end{cases} \tag{113}$$

Thus, an ODE solver can be used on these two equations to effectively solve the ODEs for all 9 components of A. Note that:

$$\frac{dx_j}{dx_i} = \frac{x_j}{x_i} \frac{2x_j - x_i - \frac{1}{x_i x_j}}{2x_i - x_j - \frac{1}{x_i x_j}} \tag{114}$$

This has solution:

$$x_j = \frac{c + \sqrt{c^2 + 4(1-c)x_i^3}}{2x_i^2} \tag{115}$$

where

$$c = -\frac{x_{i,0} \left(x_{i,0} x_{j,0}^2 - 1 \right)}{x_{i,0} - x_{j,0}} \in (-\infty, 0] \tag{116}$$

In the case that $x_{i,0} = x_{j,0}$, we have $x_i = x_j$ for all time. Thus, the ODE system for A has been reduced to a single ODE, as $x_j(x_i)$ can be inserted into the RHS of the equation for $\frac{dx_i}{d\tau}$. However, it is less computationally expensive to evolve the system presented in (113).

Bounds on Reduced Distortion ODEs If any of the relations in $x_i \geq x_j \geq x_k$ are in fact equalities, equality is maintained throughout the history of the system. This can be seen by noting that the time derivatives of the equal variables are in this case equal. If $x_j = x_k$ then $x_i = \frac{1}{x_j^2}$. Combining these results, the path of the system in (x_i, x_j) coordinates is in fact confined to the curved triangular region:

$$\left\{ (x_i, x_j) : x_i \leq x_i^0 \cap x_i \geq x_j \cap x_i \geq \frac{1}{x_j^2} \right\} \tag{117}$$

45
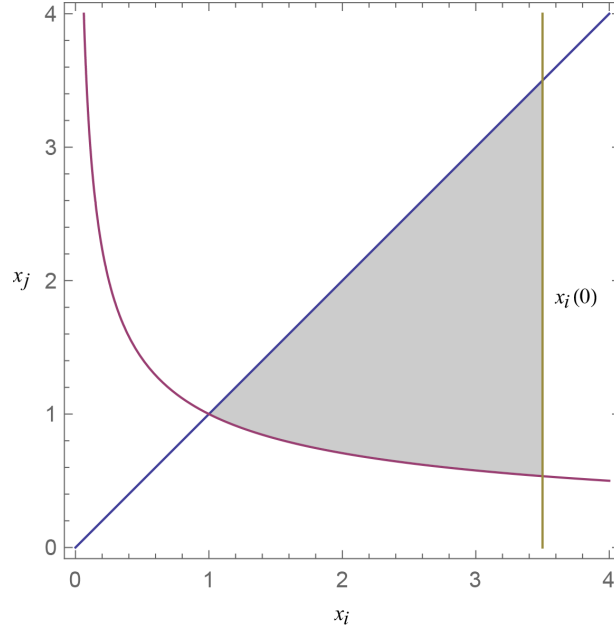
Figure 17: The (shaded) region to which x_i, x_j are confined in the evolution of the distortion ODEs

This is demonstrated in Figure 17 on page 46. By (113), the rate of change of x_i at a particular value $x_i = x_i^*$ is given by:

$$-x_i^* \left(2x_i^* - x_j - \frac{1}{x_i^* x_j} \right) \tag{118}$$

Note that:

$$\frac{d}{dx_j} \left(2x_i^* - x_j - \frac{1}{x_i^* x_j} \right) = -1 + \frac{1}{x_i^* x_j^2} = 0 \tag{119}$$

$$\Rightarrow x_j = \frac{1}{\sqrt{x_i^*}}$$

$$\frac{d^2}{dx_j^2} \left(2x_i^* - x_j - \frac{1}{x_i^* x_j} \right) = \frac{-2}{x_i^* x_j^3} < 0 \tag{120}$$

Thus, x_i decreases fastest on the line $x_i = \frac{1}{x_j^2}$ (the bottom boundary of the region given in Figure 17 on page 46), and slowest on the line $x_i = x_j$. The rates of change of x_i along these two lines are given respectively by:

$$\frac{dx_i}{d\tau} = -2x_i \left(x_i - \sqrt{\frac{1}{x_i}} \right) \tag{121a}$$

$$\frac{dx_i}{d\tau} = -x_i \left(x_i - \frac{1}{x_i^2} \right) \tag{121b}$$

These have implicit solutions:

$$\tau = (f\left(\sqrt{x_i}\right) + g\left(\sqrt{x_i}\right)) - \left(f\left(\sqrt{x_i^0}\right) + g\left(\sqrt{x_i^0}\right) \right) \equiv F_1\left(x_i; x_i^0\right) \tag{122a}$$

$$\tau = (f\left(x_i\right) - g\left(x_i\right)) - \left(f\left(x_i^0\right) - g\left(x_i^0\right) \right) \equiv F_2\left(x_i; x_i^0\right) \tag{122b}$$

where

$$f\left(x_i\right) = \frac{1}{6} \log \left(\frac{x_i^2 + x_i + 1}{\left(x_i - 1\right)^2} \right) \tag{123a}$$

$$g\left(x_i\right) = \frac{1}{\sqrt{3}} \tan^{-1} \left(\frac{2x_i + 1}{\sqrt{3}} \right) \tag{123b}$$

As (112) is an autonomous system of ODEs, it has the property that its limit $x_1 = x_2 = x_3 = 1$ is never obtained in finite time, in precise arithmetic. In floating point arithmetic we may say that the system has converged when $x_i - 1 < \epsilon$ (machine epsilon) for each i. This happens when:

$$\tau > F_2\left(1 + \epsilon; x_i^0\right) \tag{124}$$

This provides a quick method to check whether it is necessary to run the ODE solver in a particular cell. If the following condition is satisfied then we know the system in that cell converges to the ground state over the time interval in which the ODE system is calculated:

$$\frac{2}{\tau_1} \left(\frac{\rho}{\rho_0} \right)^{\frac{7}{3}} \Delta t > F_2\left(1 + \epsilon; \max\left\{x_i^0\right\}\right) \tag{125}$$

If the fluid is very inviscid, resulting in a stiff ODE, the critical time is lower, and there is more chance that the ODE system in the cell reaches its limit in Δt. This check potentially saves a lot of computationally expensive stiff ODE solves. The same goes for if the flow is slow moving, as the system will be closer to its ground state at the start of the time step and is more likely to converge over Δt. Similarly, if the following condition is satisfied then we know for sure that an ODE solver is necessary, as the system certainly will not have converged over the timestep:

$$\frac{2}{\tau_1}\left(\frac{\rho}{\rho_0}\right)^{\frac{7}{3}}\Delta t < F_1\left(1+\epsilon; \max\left\{x_i^0\right\}\right) \tag{126}$$

Analytical Approximation   We now explore cases when even the reduced ODE system (113) need not be solved numerically. Define the following variables:

$$m = \frac{x_1 + x_2 + x_3}{3} \tag{127a}$$

$$u = \frac{(x_1 - x_2)^2 + (x_2 - x_3)^2 + (x_3 - x_1)^2}{3} \tag{127b}$$

It is a standard result that $m \geq \sqrt[3]{x_1 x_2 x_3}$. Thus, $m \geq 1$. Note that u is proportional to the internal energy contribution from the distortion. From (112) we have:

$$\frac{du}{d\tau} = -18\left(1 - m\left(m^2 - \frac{5}{6}u\right)\right) \tag{128a}$$

$$\frac{dm}{d\tau} = -u \tag{128b}$$

Combining these equations, we have:

$$\frac{d^2 m}{d\tau^2} = -\frac{du}{d\tau} = 18\left(1 - m\left(m^2 - \frac{5}{6}u\right)\right) \tag{129}$$

Therefore:

$$\begin{cases} \frac{d^2 m}{d\tau^2} + 15m\frac{dm}{d\tau} + 18\left(m^3 - 1\right) = 0 \\ m\left(0\right) = m_0 \\ m^{'}\left(0\right) = -u_0 \end{cases} \tag{130}$$

We make the following assumption, noting that it is true in all physical situations tested in this study:

$$m\left(t\right) = 1 + \eta\left(t\right), \quad \eta \ll 1 \ \forall t \geq 0 \tag{131}$$

Thus, we have the linearized ODE:

$$\begin{cases} \frac{d^2 \eta}{d\tau^2} + 15\frac{d\eta}{d\tau} + 54\eta = 0 \\ \eta\left(0\right) = m_0 - 1 \\ \eta^{'}\left(0\right) = -u_0 \end{cases} \tag{132}$$

This is a Sturm Liouville equation with solution:

$$\eta\left(\tau\right) = \frac{e^{-9\tau}}{3}\left(\left(9m_0 - u_0 - 9\right)e^{3\tau} - \left(6m_0 - u_0 - 6\right)\right) \tag{133}$$

Thus, we also have:

$$u\left(\tau\right) = e^{-9\tau}\left(e^{3\tau}\left(18m_0 - 2u_0 - 18\right) - \left(18m_0 - 3u_0 - 18\right)\right) \tag{134}$$

Once $m_{\Delta t} = 1 + \eta\left(\frac{2}{\tau_1}\left(\frac{\rho}{\rho_0}\right)^{\frac{7}{3}}\Delta t\right)$ and $u_{\Delta t} = u\left(\frac{2}{\tau_1}\left(\frac{\rho}{\rho_0}\right)^{\frac{7}{3}}\Delta t\right)$ have been found, we have:

$$\frac{x_i + x_j + x_k}{3} = m_{\Delta t} \tag{135a}$$

$$\frac{\left(x_i - x_j\right)^2 + \left(x_j - x_k\right)^2 + \left(x_k - x_i\right)^2}{3} = u_{\Delta t} \tag{135b}$$

$$x_i x_j x_k = 1 \tag{135c}$$

This gives:

$$x_i = \frac{\sqrt[3]{6\left(\sqrt{81\Delta^2 - 6u_{\Delta t}^3} + 9\Delta\right)}}{6} + \frac{u_{\Delta t}}{\sqrt[3]{6\left(\sqrt{81\Delta^2 - 6u_{\Delta t}^3} + 9\Delta\right)}} + m_{\Delta t} \tag{136a}$$

$$x_j = \frac{1}{2}\left(\sqrt{\frac{x_i\left(3m_{\Delta t} - x_i\right)^2 - 4}{x_i}} + 3m_{\Delta t} - x_i\right) \tag{136b}$$

$$x_k = \frac{1}{x_i x_j} \tag{136c}$$

where

$$\Delta = -2m_{\Delta t}^3 + m_{\Delta t}u_{\Delta t} + 2 \tag{137}$$

Note that taking the real parts of the above expression for x_i gives:

$$x_i = \frac{\sqrt{6u_{\Delta t}}}{3}\cos\left(\frac{\theta}{3}\right) + m_{\Delta t} \tag{138a}$$

$$\theta = \tan^{-1}\left(\frac{\sqrt{6u_{\Delta t}^3 - 81\Delta^2}}{9\Delta}\right) \tag{138b}$$

49

	ρ	p	$\boldsymbol{v}$	A	$\boldsymbol{J}$
$x < 0$	1	$1/\gamma$	$(0, -0.1, 0)$	I_3	$\mathbf{0}$
$x \geq 0$	1	$1/\gamma$	$(0, 0.1, 0)$	I_3	$\mathbf{0}$

Table 7: Initial conditions for the slow opposing shear flow test

At this point it is not clear which values of $\{x_i, x_j, x_k\}$ are taken by x_1, x_2, x_3. However, this can be inferred from the fact that any relation $x_i \geq x_j \geq x_k$ is maintained over the lifetime of the system. Thus, the stiff ODE solver has been obviated by a few arithmetic operations.

4.3.3 Numerical Results

Strain Relaxation In this section, the approximate analytic solver for the distortion ODEs, presented in 4.3.2, is compared with a numerical ODE solver. Initial data was taken from [6]:

$$A = \begin{pmatrix} 1 & 0 & 0 \\ -0.01 & 0.95 & 0.02 \\ -0.015 & 0 & 0.9 \end{pmatrix}^{-1} \tag{139}$$

Additionally, the following parameter values were used: $\rho_0 = 1, c_s = 1, \mu = 10^{-2}$, giving $\tau_1 = 0.06$. As can be seen in Figure 18 on page 51, Figure 19 on page 51, and Figure 20 on page 51, the approximate analytic solver compares well with the numerical solver in its results for the distortion tensor A, and thus also the internal energy and stress tensor. The numerical ODE solver was the odeint solver from SciPy 0.18.1, based on the LSODA solver from the FORTRAN library ODEPACK (see [53]).

Stokes' First Problem This problem is one of the few test cases with an analytic solution for the Navier Stokes equations. It consists of two ideal gases in an infinite domain, meeting at the plane $x = 0$, initially flowing with equal and opposite velocity ± 0.1 in the y axis. The initial conditions are given in Table 7 on page 50.

The flow has a low Mach number of 0.1, and this test case is designed to demonstrate the efficacy of the numerical methods in this flow regime. The exact solution to the Navier Stokes equations is given by[5]:

$$v = v_0 \operatorname{erf}\left(\frac{x}{2\sqrt{\mu t}}\right) \tag{140}$$

Heat conduction is neglected, and $\gamma = 1.4$, $c_v = 1$, $\rho_0 = 1$, $c_s = 1$. The viscosity is variously taken to be $\mu = 10^{-2}$, $\mu = 10^{-3}$, $\mu = 10^{-4}$ (resulting in $\tau_1 = 0.06$, $\tau_1 = 0.006$, $\tau_1 = 0.0006$, respectively). Due to

---

[5]In this problem, the Navier Stokes equations reduce to $v_t = \mu v_{xx}$. Defining $\eta = \frac{x}{2\sqrt{\mu t}}$, and assuming $v = f(\eta)$, this becomes $f'' + 2\eta f' = 0$. The result follows by solving this equation with the boundary conditions $v(\pm\infty) = \pm v_0$.
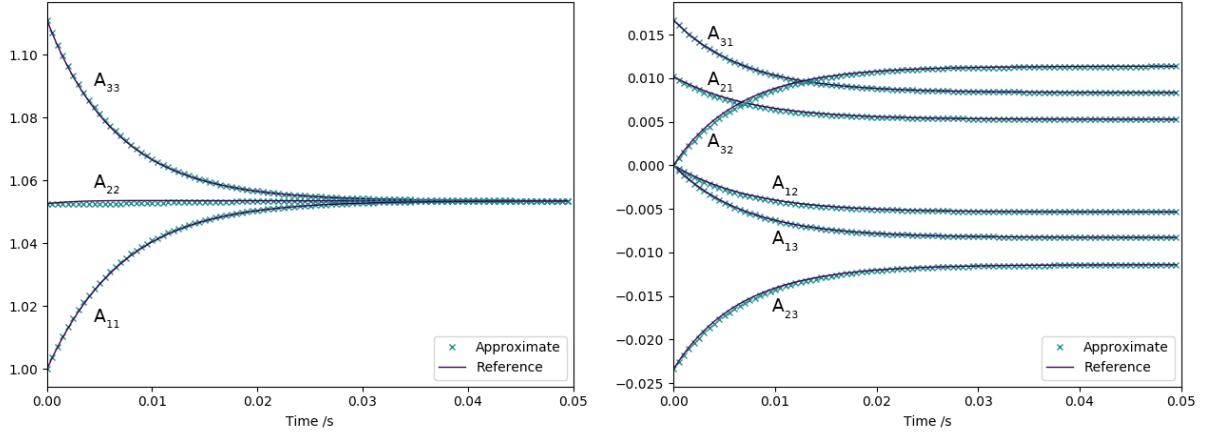
Figure 18: The components of the distortion tensor in the Strain Relaxation Test
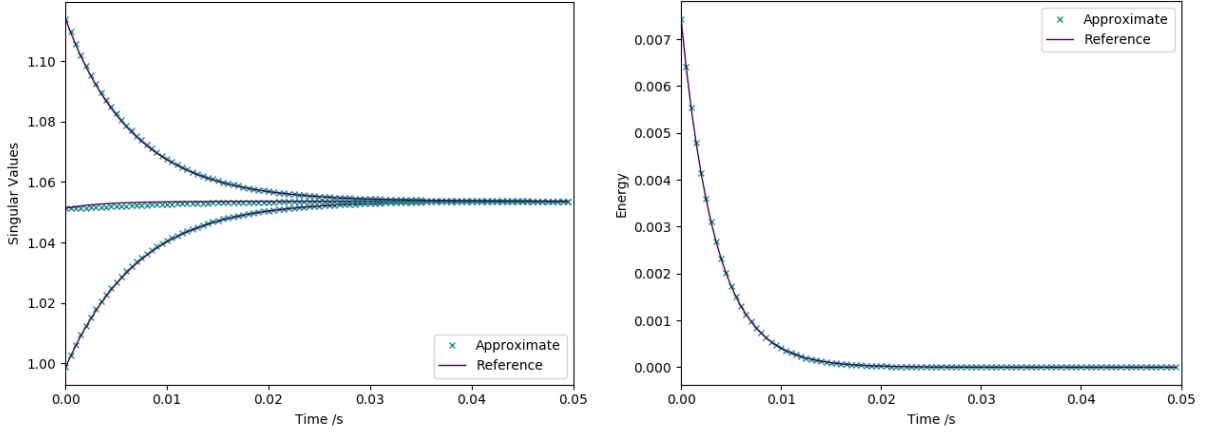
Figure 19: The singular values of the distortion tensor and the energy in the Strain Relaxation Test
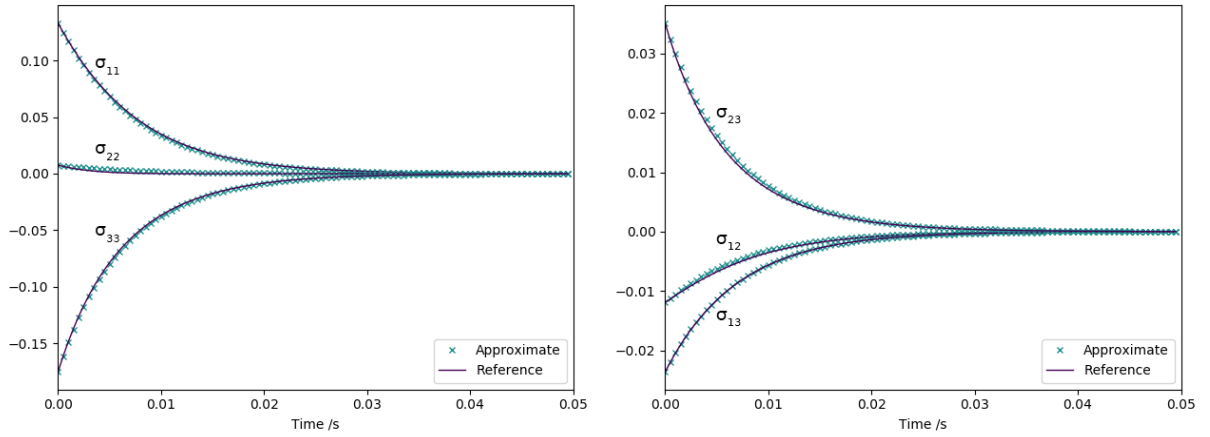
Figure 20: The components of the stress tensor in the Strain Relaxation Test

51

the stiffness of the source terms in the equations governing A in the case that $\mu = 10^{-4}$, the step (89) in the WENO reconstruction under the Split WENO method was not performed, and $\boldsymbol{w_p^{n+\frac{1}{2}}} \equiv \boldsymbol{w_p^n}$ was taken instead. This avoided the numerical diffusion that otherwise would have emerged at the interface at $x = 0$.

The results of simulations with 200 cells at time $t = 1$, using reconstruction polynomials of order $N = 2$, are presented in Figure 21 on page 53. The GPR model solved with both the ADER WENO and Split WENO methods closely matches the exact Navier Stokes solution. Note that at $\mu = 10^{-2}$ and $\mu = 10^{-3}$, the ADER WENO and Split WENO methods are almost indistinguishable. At $\mu = 10^{-4}$ the Split WENO method matches the curve of the velocity profile more closely, but overshoots slightly at the boundaries of the center region. This overshoot phenomenon is not visible in the ADER WENO results.

Viscous Shock This test is designed to demonstrate that the numerical methods used are also able to cope with fast flows. First demonstrated by Becker [9], the Navier Stokes equations have an analytic solution for $P_r = 0.75$ (see Johnson [52] for a full analysis). As noted by Dumbser [27], if the wave has nondimensionalised upstream velocity $\bar{v} = 1$ and Mach number M_c, then its nondimensionalised downstream velocity is:

$$a = \frac{1 + \frac{\gamma-1}{2}M_c^2}{\frac{\gamma+1}{2}M_c^2} \tag{141}$$

The wave's velocity profile $\bar{v}(x)$ is given by the roots of the following equation:

$$\frac{1-\bar{v}}{(\bar{v}-a)^a} = c_1 \exp\left(-c_2 x\right) \tag{142a}$$

$$c_1 = \left(\frac{1-a}{2}\right)^{1-a} \tag{142b}$$

$$c_2 = \frac{3}{4}R_e \frac{M_c^2 - 1}{\gamma M_c^2} \tag{142c}$$

c_1, c_2 are constants that affect the position of the center of the wave, and its stretch factor, respectively. Following the analysis of Morduchow and Libby [66], the nondimensional pressure and density profiles are given by:

$$\bar{p} = \frac{1}{\bar{v}}\left(1 + \frac{\gamma-1}{2}M_c^2\left(1 - \bar{v}^2\right)\right) \tag{143}$$

$$\bar{\rho} = \frac{1}{\bar{v}} \tag{144}$$

To obtain an unsteady shock traveling into a region at rest, a constant velocity field $v = M_c c_0$ is imposed on the traveling wave solution presented here (where c_0 is the adiabatic sound speed). Thus, if p_0, ρ_0 are the downstream (reference) values for pressure and density:
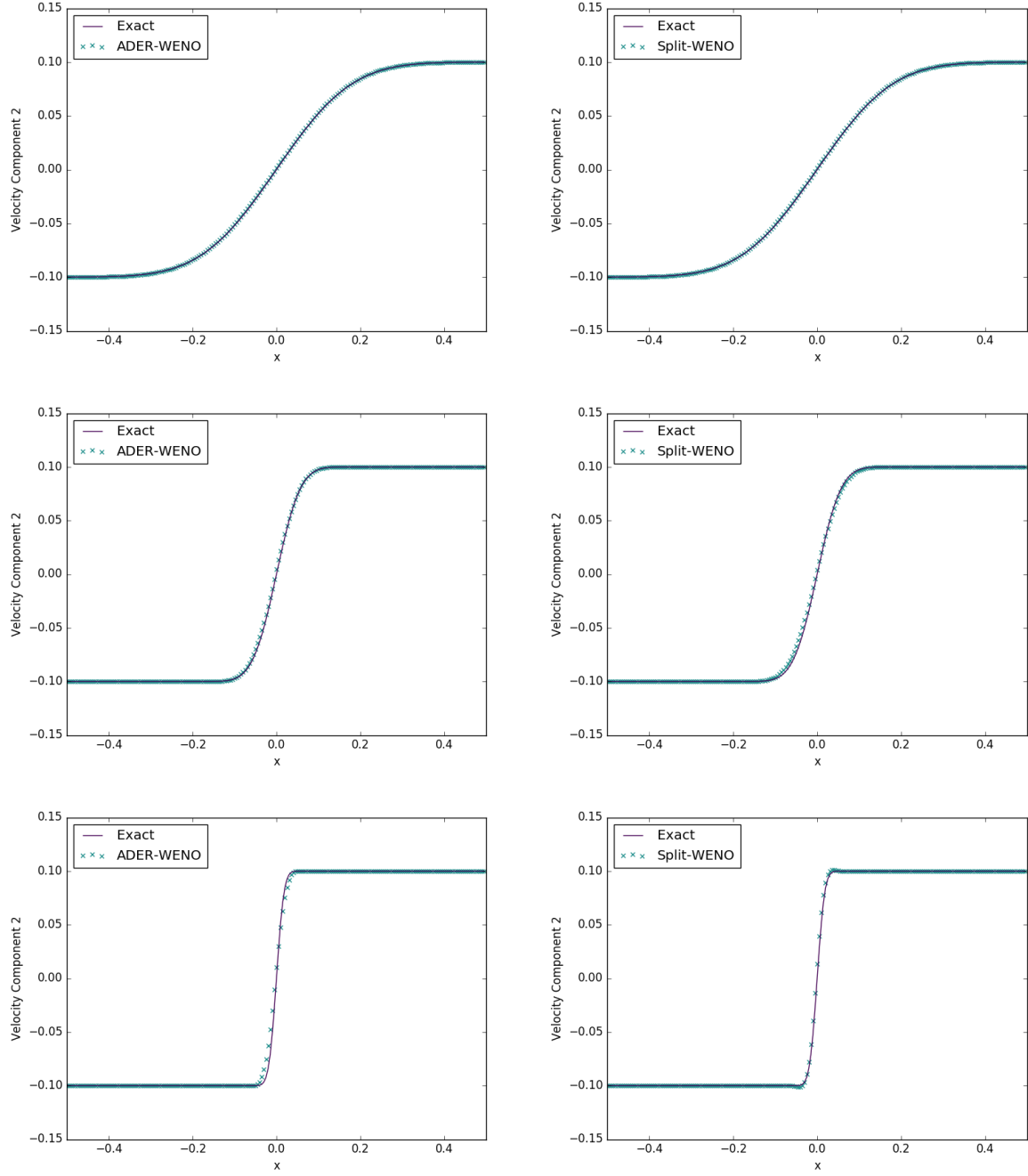
Figure 21: Results of solving Stokes' First Problem ($\mu = 10^{-2}, \mu = 10^{-3}, \mu = 10^{-4}$) with an ADER WENO scheme and a Split WENO scheme ($N = 2$)

	ρ	p	$\boldsymbol{v}$	A	$\boldsymbol{J}$
$x < 0$	2	1	$\boldsymbol{0}$	$\sqrt[3]{2} \cdot I_3$	$\boldsymbol{0}$
$x \geq 0$	0.5	1	$\boldsymbol{0}$	$\frac{1}{\sqrt[3]{2}} \cdot I_3$	$\boldsymbol{0}$

Table 8: Initial conditions for the heat conduction test

$$v = Mc_0 \left(1 - \bar{v}\right) \tag{145a}$$

$$p = p_0 \bar{p} \tag{145b}$$

$$\rho = \rho_0 \bar{\rho} \tag{145c}$$

These functions are used as initial conditions, along with $A = \sqrt[3]{\bar{\rho}} I$ and $\boldsymbol{J} = \boldsymbol{0}$. The downstream density and pressure are taken to be $\rho_0 = 1$ and $p_0 = \frac{1}{\gamma}$ (so that $c_0 = 1$). $M_c = 2$ and $R_e = 100$. The material parameters are taken to be: $\gamma = 1.4$, $p_\infty = 0$, $c_v = 2.5$, $c_s = 5$, $\alpha = 5$, $\mu = 2 \times 10^{-2}$, $\kappa = \frac{28}{3} \times 10^{-2}$ (resulting in $\tau_1 = 0.0048$, $\tau_2 = 0.005226\dot{6}$).

The results of a simulation with 200 cells at time $t = 0.2$, using reconstruction polynomials of order $N = 2$, are presented in Figure 22 on page 55 and Figure 23 on page 56. The shock was initially centered at $x = 0.25$, reaching $x = 0.65$ at the final time. Note that the density, velocity, and pressure results for both methods match the exact solution well, with the ADER WENO method appearing to produce a slightly more accurate solution. The results for the two methods for the stress tensor and heat flux are close.

Heat Conduction in a Gas   This is a simple test case to ensure that the heat transfer terms in the implementation are working correctly. Two ideal gases at different temperatures are initially in contact at position $x = 0$. The initial conditions for this problem are given in Table 8 on page 54.

The material parameters are taken to be: $\gamma = 1.4$, $c_v = 2.5$, $\rho_0 = 1$, $p_0 = 1$, $c_s = 1$, $\alpha = 2$, $\mu = 10^{-2}$, $\kappa = 10^{-2}$ (resulting in $\tau_1 = 0.06$, $\tau_2 = 0.0025$). The results of a simulation with 200 cells at time $t = 1$, using reconstruction polynomials of order $N = 2$, are presented in Figure 24 on page 56. The ADER WENO and Split WENO methods are in perfect agreement for both the temperature and heat flux profiles. As demonstrated in [27], this means that they in turn agree very well with a reference Navier Stokes Fourier solution.

Speed   Both the ADER WENO scheme and the Split WENO scheme used in this study were implemented in Python3. All array functions were precompiled with Numba's JIT capabilities and the root finding procedure in the Galerkin predictor was performed using SciPy's Newton Krylov solver, compiled against the Intel MKL. Clear differences in computational cost between the ADER WENO and Split WENO methods were apparent, as is to be expected, owing to the lack of Galerkin method in the Split WENO scheme. The wall times for the various tests undertaken in this study are given in Table 9 on page 58, comparing the combined WENO and Galerkin methods of the ADER WENO scheme to the combined WENO and ODE
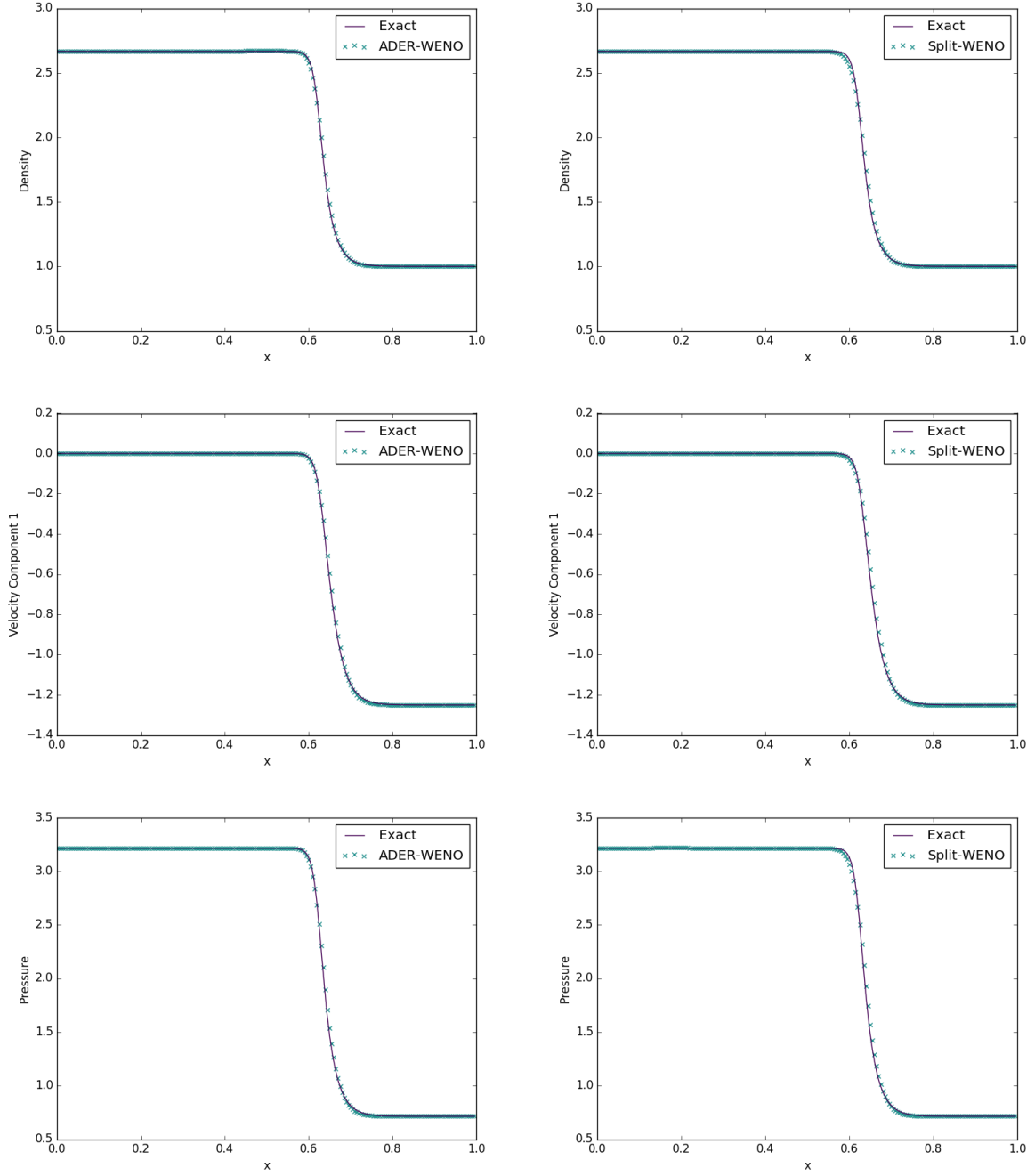
Figure 22: Density, velocity, and pressure for the Viscous Shock problem, solved with an ADER WENO scheme and a Split WENO scheme ($N = 2$)
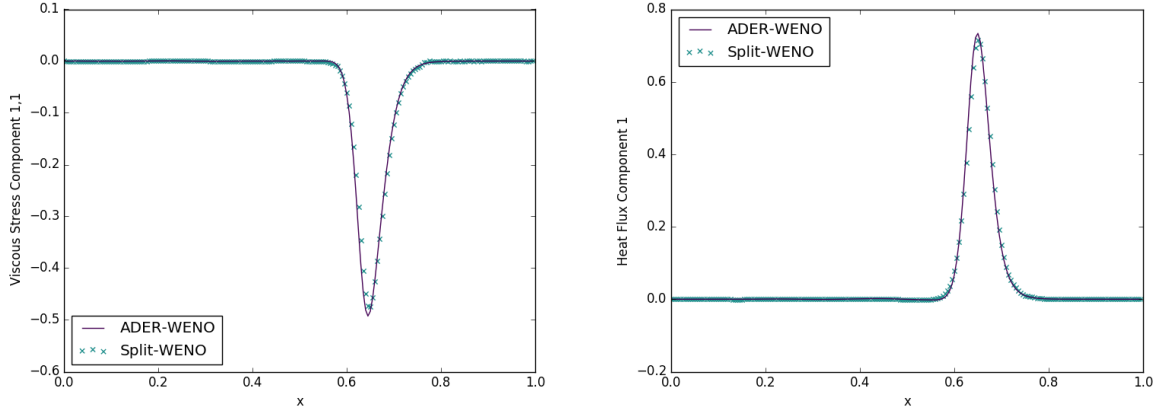
Figure 23: Viscous stress and heat flux for the Viscous Shock problem, solved with both an ADER WENO scheme and a Split WENO scheme ($N = 2$)
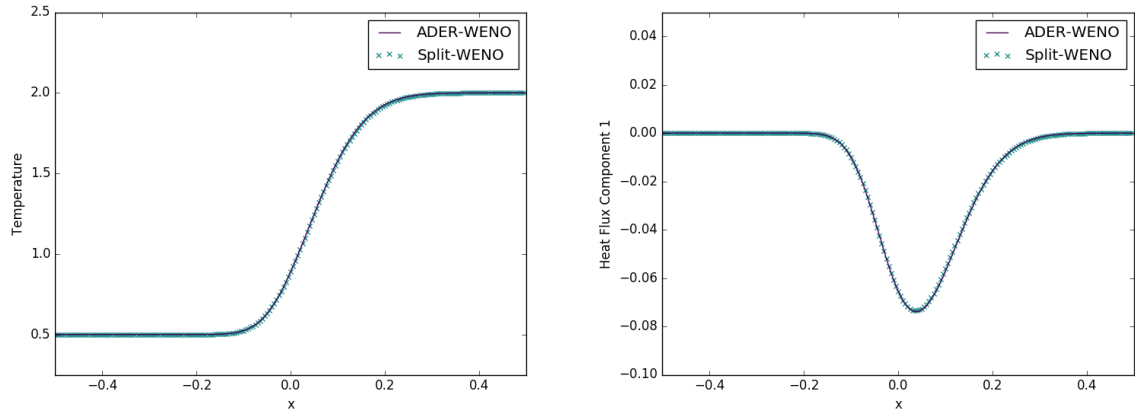
Figure 24: Results of solving the problem of Heat Conduction in Gas with both an ADER WENO scheme and a Split WENO scheme ($N = 2$)

methods of the Split WENO scheme. All computations were performed using an Intel Core i7 4910MQ, on a single core. The number of time steps taken are given in Table 10 on page 58. The differences between the methods in terms of the number of time steps taken in each test result from the fact that, for numerical stability, CFL numbers of 0.8 and 0.7 were required by the ADER WENO method and the Split WENO method, respectively.

Note that, unlike with the ADER WENO scheme, the wall time for the Split WENO scheme is unaffected by a decrease in the viscosity in Stokes' First Problem (and the corresponding increase in the stiffness of the source terms). This is because the analytic approximation to the distortion ODEs obviates the need for a stiff solver. The large difference in ADER WENO solver times between the $\mu = 10^{-3}$ and $\mu = 10^{-4}$ cases is due to the fact that, in the latter case, a stiff solver must be employed for the initial guess to the root of the nonlinear system produced by the Discontinuous Galerkin method (as described in [43]).

Convergence   To assess the rate of convergence of the Split WENO method, the convected isentropic vortex convergence study from [27] was performed. The initial conditions are given as $\rho = 1 + \delta\rho$, $p = 1 + \delta p$, $\boldsymbol{v} = (1, 1, 0) + \delta\boldsymbol{v}$, $A = \sqrt[3]{\rho}I$, $\boldsymbol{J} = \boldsymbol{0}$, where:

$$\delta T = -\frac{(\gamma - 1)\,\epsilon^2}{8\gamma\pi^2}e^{1-r^2} \tag{146a}$$

$$\delta\rho = (1 + \delta T)^{\frac{1}{\gamma-1}} - 1 \tag{146b}$$

$$\delta p = (1 + \delta T)^{\frac{\gamma}{\gamma-1}} - 1 \tag{146c}$$

$$\delta\boldsymbol{v} = \frac{\epsilon}{2\pi}e^{\frac{1-r^2}{2}}\begin{pmatrix} -(y-5) \\ x-5 \\ 0 \end{pmatrix} \tag{146d}$$

The 2D domain is taken to be $[0, 10]^2$. ϵ is taken to be 5. The material parameters are taken to be: $\gamma = 1.4$, $c_v = 2.5$, $\rho_0 = 1$, $p_0 = 1$, $c_s = 0.5$, $\alpha = 1$, $\mu = 10^{-6}$, $\kappa = 10^{-6}$ (resulting in $\tau_1 = 2.4 \times 10^{-5}$, $\tau_2 = 10^{-6}$). Thus, this can be considered to be a stiff test case.

The convergence rates in the L_1, L_2, L_∞ norms for the density variable are given in Table 11 on page 58 and Table 12 on page 58 for WENO reconstruction polynomial orders of $N = 2$ and $N = 3$, respectively. As expected, both sets of tests attain roughly second order convergence. For comparison, the corresponding results for this test from [27]   solved using a third order P2P2 scheme   are given in Table 13 on page 58 for comparison.

4.4   New Numerical Methods: Eigendecomposition of the Cauchy Tensor

It is noted by [68]:

	ADER WENO	Split WENO	Speed up
Stokes' First Problem ($\mu = 10^{-2}$)	265s	38s	7.0
Stokes' First Problem ($\mu = 10^{-3}$)	294s	38s	7.7
Stokes' First Problem ($\mu = 10^{-4}$)	536s	38s	14.1
Viscous Shock	297s	56s	5.3
Heat Conduction in a Gas	544s	94s	5.8

Table 9: Wall time for various tests (all with 200 cells) under the ADER WENO method and the Split WENO method

	Timesteps (ADER WENO)	Timesteps (Split WENO)
Stokes' First Problem ($\mu = 10^{-2}$)	385	442
Stokes' First Problem ($\mu = 10^{-3}$)	386	443
Stokes' First Problem ($\mu = 10^{-4}$)	385	442
Viscous Shock	562	645
Heat Conduction in a Gas	942	1077

Table 10: Time steps taken for various tests (all with 200 cells) under the ADER WENO method and the Split WENO method

Grid Size	$\epsilon(L_1)$	$\epsilon(L_2)$	$\epsilon(L_\infty)$	$\mathcal{O}(L_1)$	$\mathcal{O}(L_2)$	$\mathcal{O}(L_\infty)$
20	2.87×10^{-3}	7.15×10^{-3}	6.21×10^{-2}			
40	5.81×10^{-4}	1.62×10^{-3}	1.73×10^{-2}	2.30	2.14	1.85
60	1.98×10^{-4}	5.39×10^{-4}	5.94×10^{-3}	2.65	2.70	2.63
80	1.23×10^{-4}	3.47×10^{-4}	3.41×10^{-3}	1.67	1.52	1.92

Table 11: Convergence rates for the Split WENO method ($N = 2$)

Grid Size	$\epsilon(L_1)$	$\epsilon(L_2)$	$\epsilon(L_\infty)$	$\mathcal{O}(L_1)$	$\mathcal{O}(L_2)$	$\mathcal{O}(L_\infty)$
10	1.01×10^{-2}	2.58×10^{-2}	1.27×10^{-1}			
20	1.68×10^{-3}	4.02×10^{-3}	2.93×10^{-2}	2.59	2.68	2.11
30	5.34×10^{-4}	1.57×10^{-3}	1.70×10^{-2}	2.83	2.32	1.34
40	3.32×10^{-4}	8.94×10^{-4}	7.55×10^{-3}	1.65	1.95	2.82

Table 12: Convergence rates for the Split WENO method ($N = 3$)

Grid Size	$\epsilon(L_1)$	$\epsilon(L_2)$	$\epsilon(L_\infty)$	$\mathcal{O}(L_1)$	$\mathcal{O}(L_2)$	$\mathcal{O}(L_\infty)$
20	9.44×10^{-3}	2.20×10^{-3}	2.16×10^{-3}			
40	1.95×10^{-3}	4.50×10^{-4}	4.27×10^{-4}	2.27	2.29	2.34
60	7.52×10^{-4}	1.74×10^{-4}	1.48×10^{-4}	2.35	2.35	2.61
80	3.72×10^{-4}	8.66×10^{-5}	7.40×10^{-5}	2.45	2.42	2.41

Table 13: Convergence rates for the ADER DG PNPM method ($N, M = 2$)

As long as a fluid under consideration is simple and a flow is laminar, the information about rotations of fluid particles stored in the distortion A can be ignored and, for example, the [Cauchy] deformation tensor $G = A^T A$ can be used as the state variable instead of A. The situation becomes quite different if we consider complex fluids, e.g., liquid crystals, where the orientation of particles plays an important role, and therefore, particle rotations cannot be ignored. One may expect that the same is true for turbulent flows of simple Newtonian fluid.

Thus, for simple laminar flows, (1c) can be replaced with the following evolution equation for G, which is easily derived from (1c):

$$\frac{\partial G_{ij}}{\partial t} + v_k \frac{\partial G_{ij}}{\partial x_k} + G_{ik} \frac{\partial v_k}{\partial x_j} + G_{jk} \frac{\partial v_k}{\partial x_i} = \frac{2\sigma_{ij}}{\rho \theta_1(\tau_1)} \tag{147}$$

4.4.1 Evolution Equations for the Eigenvalues and Eigenvectors

As G is symmetric positive definite, it has the following eigendecomposition:

$$G = U\Lambda U^T \tag{148}$$

where Λ is the diagonal matrix of eigenvalues and U is orthonormal. Note that:

$$G \operatorname{dev}(G) = U\Lambda U^T \left(U\Lambda U^T - \frac{\operatorname{tr}\left(U\Lambda U^T \right)}{3} I \right) = U\Lambda \operatorname{dev}(\Lambda) U^T \tag{149}$$

Thus, (147) becomes:

$$\dot{U}\Lambda U^T + U\dot{\Lambda}U + U\Lambda \dot{U}^T + U\Lambda U^T \nabla \boldsymbol{v} + \nabla \boldsymbol{v}^T U\Lambda U^T = \frac{-2c_s^2}{\theta_1(\tau_1)} U\Lambda \operatorname{dev}(\Lambda) U^T \tag{150}$$

where $\dot{X}$ is the material derivative of quantity X. Therefore:

$$U^T \dot{U}\Lambda + \dot{\Lambda} + \Lambda \dot{U}^T U + \Lambda U^T \nabla \boldsymbol{v} U + U^T \nabla \boldsymbol{v}^T U\Lambda = \frac{-2c_s^2}{\theta_1(\tau_1)} \Lambda \operatorname{dev}(\Lambda) \tag{151}$$

Let $\boldsymbol{q} = s + x\boldsymbol{i} + y\boldsymbol{j} + z\boldsymbol{k}$ be the unit quaternion (so that $s^2 + x^2 + y^2 + z^2 = 1$) corresponding to the rotation matrix U. Then we have:

$$U = \begin{pmatrix} 1 - 2y^2 - 2z^2 & 2xy - 2sz & 2zx + 2sy \\ 2xy + 2sz & 1 - 2z^2 - 2x^2 & 2yz - 2sx \\ 2zx - 2sy & 2yz + 2sx & 1 - 2x^2 - 2y^2 \end{pmatrix} \tag{152}$$

Noting that $s\dot{s} + x\dot{x} + y\dot{y} + z\dot{z} = 0$, it is straightforward to confirm that we have:

$$U^T\dot{U}\Lambda + \Lambda\dot{U}^TU = 2\begin{pmatrix} 0 & (s\dot{z} - z\dot{s} + y\dot{x} - x\dot{y})(\lambda_1 - \lambda_2) & (s\dot{y} - y\dot{s} + x\dot{z} - z\dot{x})(\lambda_3 - \lambda_1) \\ (s\dot{z} - z\dot{s} + y\dot{x} - x\dot{y})(\lambda_1 - \lambda_2) & 0 & (s\dot{x} - x\dot{s} + z\dot{y} - y\dot{z})(\lambda_2 - \lambda_3) \\ (s\dot{y} - y\dot{s} + x\dot{z} - z\dot{x})(\lambda_3 - \lambda_1) & (s\dot{x} - x\dot{s} + z\dot{y} - y\dot{z})(\lambda_2 - \lambda_3) & 0 \end{pmatrix}$$
(153)

Thus, (151) is equivalent to the set of six equations:

$$\dot{\Lambda}_{ii} + \left(\Lambda U^T\nabla\boldsymbol{v}U + U^T\nabla\boldsymbol{v}^TU\Lambda\right)_{ii} = \frac{-2c_s^2}{\theta_1(\tau_1)}\left(\Lambda\,\mathrm{dev}\,(\Lambda)\right)_{ii}$$
(154a)

$$\left(U^T\dot{U}\Lambda + \Lambda\dot{U}^TU\right)_{jk} + \left(\Lambda U^T\nabla\boldsymbol{v}U + U^T\nabla\boldsymbol{v}^TU\Lambda\right)_{jk} = 0$$
(154b)

where $i = 1, 2, 3$ and $(j, k) = (1, 2), (1, 3), (2, 3)$. Note that these equations can be written in the more succinct form:

$$\dot{\lambda}_i + \lambda_i\,\|\boldsymbol{u_i}\|^2_{\mathrm{sym}(\nabla\boldsymbol{v})} = \frac{-2c_s^2}{\theta_1(\tau_1)}\lambda_i\left(\lambda_i - \bar{\lambda}\right)$$
(155a)

$$\mathrm{sym}\left(U^T\dot{U}\Lambda\right)_{jk} + \mathrm{sym}\left(\Lambda U^T\nabla\boldsymbol{v}U\right)_{jk} = 0$$
(155b)

where:

$$\bar{x} = \frac{x_1 + x_2 + x_3}{3}$$
(156a)

$$\mathrm{sym}\,(X) = X + X^T$$
(156b)

$$\|\boldsymbol{u}\|^2_X = \boldsymbol{u}^T X \boldsymbol{u}$$
(156c)

Elements $(2, 3), (1, 3), (1, 2)$ of $\mathrm{sym}\left(U^T\dot{U}\Lambda\right)$ can be written in the following form:

$$2\begin{pmatrix} (s\dot{x} - x\dot{s} + z\dot{y} - y\dot{z})(\lambda_2 - \lambda_3) \\ (s\dot{y} - y\dot{s} + x\dot{z} - z\dot{x})(\lambda_3 - \lambda_1) \\ (s\dot{z} - z\dot{s} + y\dot{x} - x\dot{y})(\lambda_1 - \lambda_2) \end{pmatrix} = 2\begin{pmatrix} \left(s\dot{x} + x\frac{x\dot{x}+y\dot{y}+z\dot{z}}{s} + z\dot{y} - y\dot{z}\right)(\lambda_2 - \lambda_3) \\ \left(s\dot{y} + y\frac{x\dot{x}+y\dot{y}+z\dot{z}}{s} + x\dot{z} - z\dot{x}\right)(\lambda_3 - \lambda_1) \\ \left(s\dot{z} + z\frac{x\dot{x}+y\dot{y}+z\dot{z}}{s} + y\dot{x} - x\dot{y}\right)(\lambda_1 - \lambda_2) \end{pmatrix}$$
(157)

Denoting elements $(2, 3), (1, 3), (1, 2)$ of $\mathrm{sym}\left(\Lambda U^T\nabla\boldsymbol{v}U\right)$ by $\boldsymbol{b}$, this in turn is equal to:

$$2 \begin{pmatrix} \lambda_2 - \lambda_3 & 0 & 0 \\ 0 & \lambda_3 - \lambda_1 & 0 \\ 0 & 0 & \lambda_1 - \lambda_2 \end{pmatrix} \begin{pmatrix} \frac{x^2}{s} + s & \frac{xy}{s} + z & \frac{xz}{s} - y \\ \frac{yx}{s} - z & \frac{y^2}{s} + s & \frac{yz}{s} + x \\ \frac{zx}{s} + y & \frac{zy}{s} - x & \frac{z^2}{s} + s \end{pmatrix} \begin{pmatrix} \dot{x} \\ \dot{y} \\ \dot{z} \end{pmatrix} = \boldsymbol{b} \qquad (158)$$

Thus, using the fact that $s^2 + x^2 + y^2 + z^2 = 1$:

$$\begin{pmatrix} \dot{x} \\ \dot{y} \\ \dot{z} \end{pmatrix} = -\frac{1}{2} \begin{pmatrix} s & -z & y \\ z & s & -x \\ -y & x & s \end{pmatrix} \begin{pmatrix} \frac{1}{\lambda_2 - \lambda_3} & 0 & 0 \\ 0 & \frac{1}{\lambda_3 - \lambda_1} & 0 \\ 0 & 0 & \frac{1}{\lambda_1 - \lambda_2} \end{pmatrix} \boldsymbol{b} \qquad (159)$$

The six equations contained in (155a), (159) will in this study be used to replace the nine equations contained in (1c). The advantage of this is that the eigendecomposition of G is readily calculated as part of the evolution of the system, rather than having to be calculated separately at each time step.

It should be noted that the right hand side of (159) is undefined when $\lambda_i = \lambda_j$ for some $i \neq j$. This is because the eigenvectors of G are not uniquely defined when one or more eigenvalues take the same value (as the corresponding eigenspaces have dimension $d > 1$). This issue is treated numerically by taking:

$$\frac{1}{\lambda_i - \lambda_j} \approx \text{sign}\left(\frac{1}{\lambda_i - \lambda_j}\right) \times \min\left(\left|\frac{1}{\lambda_i - \lambda_j}\right|, \Theta\right) \qquad (160)$$

where Θ is a large number, less than or equal to the largest representable number available on the computational platform being used.

4.4.2 Validation of the Eigendecomposition ODEs

This test case is undertaken to determine the results of using the split evolution equations for the eigenvalues and eigenvectors of G (as given in 4.4.1), under a flow with a constant strain rate tensor. The value of the strain rate tensor was taken from [68]:

$$\frac{\partial v_i}{\partial x_j} = \begin{pmatrix} 0.62 & 0.40 & 1.14 \\ -0.28 & -1.41 & 0.59 \\ -0.19 & -0.72 & -1.28 \end{pmatrix} \qquad (161)$$

These values were determined randomly in the cited paper, and they are used here only for comparability. The particle settled life time was $\tau = 1.45 \times 10^{-9} s$. The results of this test are presented in Figure 25 on page 62. As can be seen, the obtained values for the eigenvalues exactly match those obtained with the original ODEs. Under the original formulation, as soon as the flow starts, the eigenvectors "snap" to their constant values after the first time step. Under the new formulation, the eigenvectors relax to their true values in a continuous manner. The larger the parameter Θ in (160), the faster this relaxation occurs, but the stiffer the ODEs that need to be solved become.
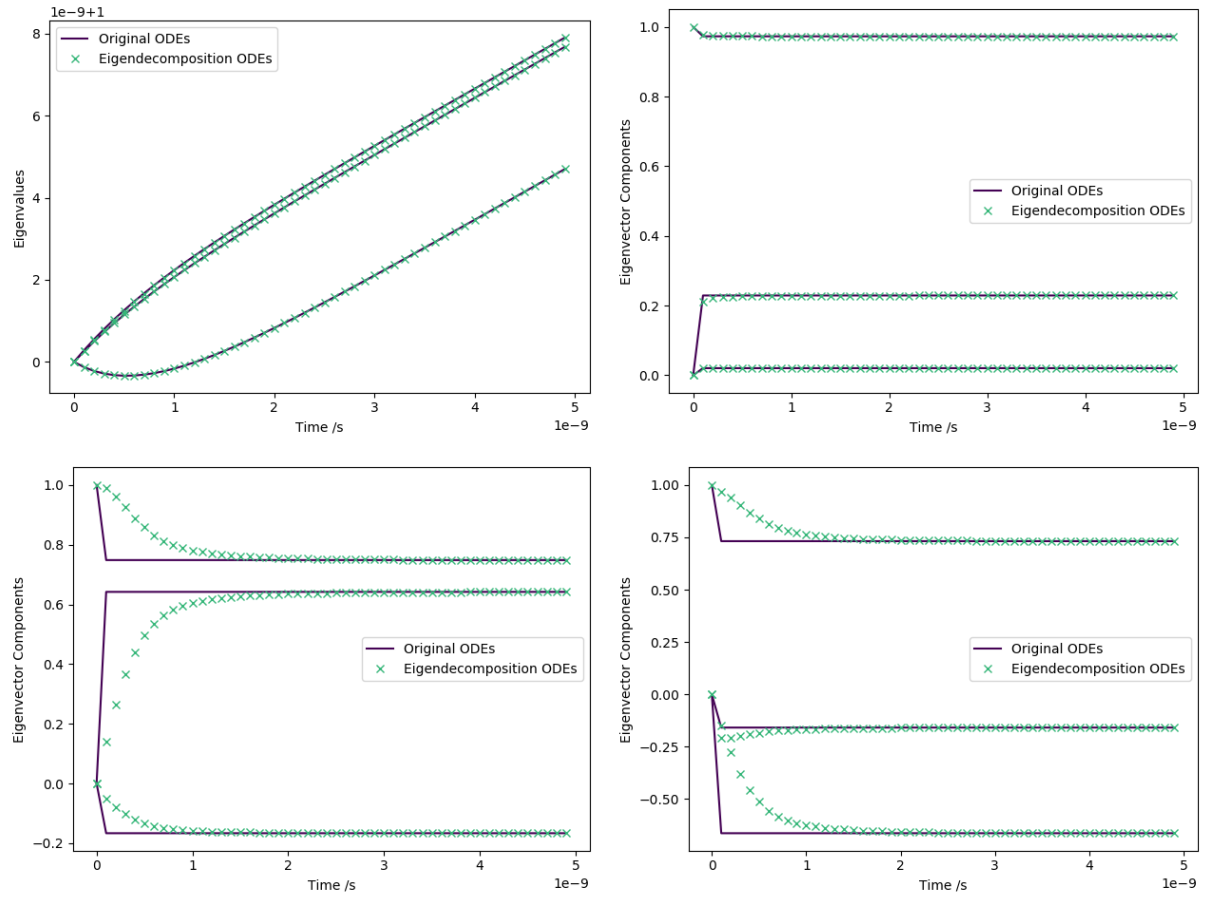
Figure 25: The evolution of the eigenvalues and eigenvectors of the Cauchy Deformation Tensor using the canonical ODEs and the new ODEs

5 Outline for Future Work

To restate the research objectives given in Section 3, my PhD project consists of the following components:

1. To develop stable and accurate techniques to deal with the interfaces between different materials in multimaterial / multiphase problems

2. To combine the GPR model with the models we use to describe the reactions of a combustible materials

3. To develop numerical methods for solving the GPR model in a reasonable amount of time

To address each of these objectives one by one:

1. As was seen in 4.1, I have developed a stable numerical method for dealing with material interfaces under the GPR model. This has only been tested in one dimension, however. It is well know that in multiple dimensions issues with accuracy and stability can arise in ghost fluid methods and their accompanying methods of evolution of the position the interface (in this study, level set methods) [17, 81]. This extension to multiple dimensions and consequent analysis remains to be done for the ghost fluid method I have developed, and I will also be comparing it with the more recent cut cell methods (see [10, 41] for an overview), as they have been demonstrated to outperform ghost fluid methods in some situations.

2. Although I have combined the GPR model with simple Arrhenius reaction kinetics terms, as seen in 4.2, there remains a great deal of work to incorporate more complicated reaction pathways (for example, see [71]), and extra terms to keep track of the state information of both reactants and products (e.g. see [62]). Although this should be straightforward, there may be unforseen difficulties in accomplishing this with the GPR model, and in any case this work will be time consuming.

3. As seen in 4.3, I have developed a new numerical method for the GPR model that is significantly faster than the currently available ADER WENO methods (achieving over an order of magnitude speed up on stiff test cases), but still able to attain second order accurate solutions. The theoretical work I have presented in 4.4 to improve further upon this method needs to be validated with further test cases, and I will perform this for the test cases presented in 4.3.

Except in the case of unforseen difficulties in any of these noted extensions to the work I have already performed, it is reasonable to expect that I will be able to complete these tasks over the course of my second year, given the pace of my research output in my first year. My third year will consist of the full implementation and testing of these features in optimized C++ code, in a form compatible with my group's current codebase, and possible integration into this codebase, followed by full documentation in my doctoral thesis of all results obtained.

As it is difficult at this stage to judge exactly how long each of these stages may take, I note another possible extension of this work in the case that I have some spare time at the end of my course. The GPR model was recently modified to include magnetohydrodynamic effects [28] and the problem case given in Section 3

could be extended in a form that necessitates this modification. For example, instead of inducing detonation in the combustible liquid by mechanical impact, it is possible to produce this effect by lighting strike (see [1, 13] for similar to the problems). A fourth state of matter (plasma) can be incorporated into this problem. I do not expect to have time to perform this extension, and I will have fulfilled the requirements of my PhD project if I complete the tasks detailed that come before it. However its inclusion here guarantees that there will be no point at which I am without working needing to be performed.

References

[1] G. F. ABDELAL AND A. MURPHY, *A Multiphysics simulation approach for efficient modelling of a waveform B lightning strike on aircraft structures*, 45 (2017), pp. 1–21.

[2] M. AIVAZIS, W. GODDARD, D. MEIRON, M. ORTIZ, J. POOL, AND J. SHEPHERD, *A virtual test facility for simulating the dynamic response of materials*, Computing in Science & Engineering, 2 (2000), pp. 39–50.

[3] F. ALCRUDO AND F. BENKHALDOUN, *Exact solutions to the Riemann problem of the shallow water equations with a bottom step*, Computers & Fluids, 30 (2001), pp. 643–671.

[4] S. ARRHENIUS, *On the Reaction Velocity of the Inversion of Cane Sugar by Acids*, Zeitschrift für Physikalische Chemie, 4 (1889), pp. 226–248.

[5] ——, *The heat of dissociation of electrolytes and the influence of temperature on the degree of dissociation*, Wilhelm Engelmann, 1889.

[6] P. T. BARTON AND D. DRIKAKIS, *An Eulerian method for multi component problems in non linear elasticity with sliding interfaces*, Journal of Computational Physics, 229 (2010), pp. 5518–5540.

[7] P. T. BARTON, D. DRIKAKIS, E. ROMENSKI, AND V. A. TITAREV, *Exact and approximate solutions of Riemann problems in non linear elasticity*, Journal of Computational Physics, 228 (2009), pp. 7046–7068.

[8] P. T. BARTON, B. OBADIA, AND D. DRIKAKIS, *A conservative level set based method for compressible solid/fluid problems on fixed grids*, Journal of Computational Physics, 230 (2011), pp. 7867–7890.

[9] R. BECKER, *Impact Waves and Detonation*, Zeitschrift für Physik, 8 (1929), p. 381.

[10] M. BERGER, M. ST, M. J. AFTOSMIS, N. AMES, AND S. R. ALLMARAS, *Progress Towards a Cartesian Cut Cell Method for Viscous Compressible Flow*.

[11] W. BOSCHERI, M. DUMBSER, AND R. LOUBERE, *Cell centered direct Arbitrary Lagrangian Eulerian ADER WENO finite volume schemes for nonlinear hyperelasticity*, International Journal for Numerical Methods in Fluids, 135 (2016), pp. 111–129.

[12] D. L. CHAPMAN, *On the Rate of Explosion in Gases*, Philosophical Magazine Series 5, 47 (1899), pp. 90–104.

[13] C. Chen, W. B. Li, and J. Liu, *Numerical Simulation of Cook Off for Passive RDX*, Advanced Materials Research, 989 994 (2014), pp. 2679–2683.

[14] J. F. Clarke, D. R. Kassoy, and N. Riley, *Shocks generated in a confined gas due to rapid heat addition at the boundary*, Proceedings of the Royal Society of London A, 393 (1984), pp. 309–329.

[15] ——, *On the direct initiation of a plane detonation wave*, Proceedings of the Royal Society of London A, 408 (1986), pp. 129–148.

[16] ——, *On the evolution of plane detonations*, Proceedings of the Royal Society of London A, 429 (1990), pp. 259–283.

[17] O. Desjardins, V. Moureau, and H. Pitsch, *An accurate conservative level set / ghost fluid method for simulating turbulent atomization*, 227 (2008), pp. 8395–8416.

[18] W. Doring, *On detonation processes in gases*, Annalen der Physik, 43 (1943), pp. 421–436.

[19] M. Dumbser and D. S. Balsara, *A new efficient formulation of the HLLEM Riemann solver for general conservative and non conservative hyperbolic systems*, Journal of Computational Physics, 304 (2016), pp. 275–319.

[20] M. Dumbser and D. S. Balsara, *A new efficient formulation of the HLLEM Riemann solver for general conservative and non conservative hyperbolic systems*, Journal of Computational Physics, 304 (2016), pp. 275–319.

[21] M. Dumbser, D. S. Balsara, E. F. Toro, and C. D. Munz, *A unified framework for the construc tion of one step finite volume and discontinuous Galerkin schemes on unstructured meshes*, Journal of Computational Physics, 227 (2008), pp. 8209–8253.

[22] M. Dumbser, M. Castro, C. Pares, and E. F. Toro, *ADER schemes on unstructured meshes for nonconservative hyperbolic systems: Applications to geophysical flows*, Computers & Fluids, 38 (2009), pp. 1731–1748.

[23] M. Dumbser, C. Enaux, and E. F. Toro, *Finite volume schemes of very high order of accuracy for stiff hyperbolic balance laws*, Journal of Computational Physics, 227 (2008), pp. 3971–4001.

[24] M. Dumbser, A. Hidalgo, M. Castro, C. Pares, and E. F. Toro, *FORCE schemes on un structured meshes II: Non conservative hyperbolic systems*, Computer Methods in Applied Mechanics & Engineering, 199 (2010), pp. 625–647.

[25] M. Dumbser, A. Hidalgo, and O. Zanotti, *High order space time adaptive ADER WENO finite volume schemes for non conservative hyperbolic systems*, Computer Methods in Applied Mechanics & Engineering, 268 (2014), pp. 359–387.

[26] M. Dumbser, I. Peshkov, E. Romenski, and O. Zanotti, *High order ADER schemes for a unified first order hyperbolic formulation of continuum mechanics: viscous heat conducting fluids and elastic solids*, Journal of Computational Physics, 314 (2015), pp. 824–862.

[27] ——, *High order ADER schemes for a unified first order hyperbolic formulation of continuum mechan ics: Viscous heat conducting fluids and elastic solids*, Journal of Computational Physics, 314 (2016), pp. 824–862.

65

[28] ——, *High order ADER schemes for a unified first order hyperbolic formulation of Newtonian continuum mechanics coupled with electro dynamics*, (2016).

[29] M. DUMBSER AND E. F. TORO, *A simple extension of the Osher Riemann solver to non conservative hyperbolic systems*, Journal of Scientific Computing, 48 (2011), pp. 70–88.

[30] ——, *On universal Osher type schemes for general nonlinear hyperbolic conservation laws*, Communications in Computational Physics, 10 (2011), pp. 635–671.

[31] ——, *On universal Osher type schemes for general nonlinear hyperbolic conservation laws*, Communications in Computational Physics, 10 (2011), pp. 635–671.

[32] M. DUMBSER AND O. ZANOTTI, *Very high order PNPM schemes on unstructured meshes for the resistive relativistic MHD equations*, Journal of Computational Physics, 228 (2009), pp. 6991–7006.

[33] M. DUMBSER, O. ZANOTTI, A. HIDALGO, AND D. S. BALSARA, *ADER WENO finite volume schemes with space time adaptive mesh refinement*, Journal of Computational Physics, 248 (2013), pp. 257–286.

[34] R. FEDKIW, T. ASLAM, B. MERRIMAN, AND S. OSHER, *A Non oscillatory Eulerian Approach to Interfaces in Multimaterial Flows (the Ghost Fluid Method)*, Journal of Computational Physics, 152 (1999), pp. 457–492.

[35] R. P. FEDKIW, *Coupling an Eulerian Fluid Calculation to a Lagrangian Solid Calculation with the Ghost Fluid Method*, Journal of Computational Physics, 175 (2002), pp. 200–224.

[36] J. FRENKEL, *Kinetic Theory of Liquids*, Oxford University Press, 1947.

[37] N. S. GHAISAS, A. SUBRAMANIAM, AND S. K. LELE, *High Order Eulerian Methods for Elastic Plastic Flow in Solids and Coupling with Fluid Flows*, 46th AIAA Fluid Dynamics Conference, (2016), pp. 1–17.

[38] M. B. GILES, *An extended collection of matrix derivative results for forward and reverse mode algorithmic differentiation*, tech. rep., University of Oxford, 2008.

[39] J. GLIMM AND D. MARCHESIN, *A Numerical Method for Two Phase Flow with an Unstable Interface*, Journal of Computational Physics, 39 (1981), pp. 179–200.

[40] S. K. GODUNOV AND E. ROMENSKI, *Elements of continuum mechanics and conservation laws*, 2003.

[41] D. HARTMANN, M. MEINKE, AND W. SCHRÖDER, *A strictly conservative Cartesian cut cell method for compressible viscous flows on adaptive grids*, Computer Methods in Applied Mechanics and Engineering, 200 (2011), pp. 1038–1052.

[42] C. HELZEL, R. J. LEVEQUE, AND G. WARNECKE, *A Modified Fractional Step Method for the Accurate Approximation of Detonation Waves*, SIAM Journal on Scientific Computing, 22 (2000), pp. 1489–1510.

[43] A. HIDALGO AND M. DUMBSER, *ADER schemes for nonlinear systems of stiff advection diffusion reaction equations*, Journal of Scientific Computing, 48 (2011), pp. 173–189.

[44] C. W. HIRT AND B. D. NICHOLS, *Volume of fluid (VOF) method for the dynamics of free boundaries*, Journal of Computational Physics, 39 (1981), pp. 201–225.

[45] G. Hou, J. Wang, and A. Layton, *Numerical methods for fluid structure interaction — A review*, Communications in Computational Physics, 12 (2012), pp. 337–377.

[46] B. Hübner, E. Walhorn, and D. Dinkler, *A monolithic approach to fluid structure interaction using space time finite elements*, Computer Methods in Applied Mechanics & Engineering, 193 (2004), pp. 2087–2104.

[47] H. Jackson, *A Fast Numerical Scheme for the Godunov Peshkov Romenski Model of Continuum Mechanics*, (2017).

[48] ——, *On the Eigenvalues of the ADER WENO Galerkin Predictor*, Journal of Computational Physics, 333 (2017), pp. 409–413.

[49] H. Jackson and N. Nikiforakis, *A New Method for Simulating Gaseous Cookoff on Short Bounded Domains*, (in preparation), (2017).

[50] A. Jameson, *Formulation of Kinetic Energy Preserving Conservative Schemes for Gas Dynamics and Direct Numerical Simulation of One Dimensional Viscous Compressible Flow in a Shock Tube Using Entropy and Kinetic Energy Preserving Schemes*, Journal of Scientific Computing, 34 (2008), pp. 188–208.

[51] G. S. Jiang and C. W. Shu, *Efficient implementation of weighted WENO schemes*, Journal of Computational Physics, 126 (1996), pp. 202–228.

[52] B. M. Johnson, *Analytical shock solutions at large and small Prandtl number*, Journal of Fluid Mechanics, 726 (2013), pp. 1–12.

[53] E. Jones, T. Oliphant, P. Peterson, and Others, *{SciPy}: Open source scientific tools for {Python}*.

[54] E. Jouget, *On the Propagation of Chemical Reactions in Gases*, Journal de Mathématiques Pures et Appliquées, 1 (1905), pp. 347–425.

[55] A. Kapila, D. W. Schwendeman, J. J. Quirk, and T. Hawa, *Mechanisms of detonation formation due to a temperature gradient*, Combustion Theory & Modelling, 6 (2002), pp. 553–594.

[56] A. Legay, J. Chessa, and T. Belytschko, *An Eulerian Lagrangian method for fluid structure interaction based on level sets*, Computer Methods in Applied Mechanics & Engineering, 195 (2006), pp. 2070–2087.

[57] T. G. Liu, B. C. Khoo, and K. S. Yeo, *Ghost fluid method for strong shock impacting on material interface*, Journal of Computational Physics, 190 (2003), pp. 651–681.

[58] T. P. Liu, *The Riemann problem for general systems of conservation laws*, Journal of Differential Equations, 18 (1975), pp. 218–234.

[59] X. D. Liu, S. Osher, and T. Chan, *Weighted essentially non oscillatory schemes*, Journal of Computational Physics, 115 (1994), pp. 200–212.

[60] A. N. Malyshev and E. I. Romenski, *Hyperbolic Equations for Heat Transfer. Global Solvability of the Cauchy Problem*, Sibirskii Matematicheskii Zhurnal, 27 (1984), pp. 128–134.

[61] A. McAdams, A. Selle, R. Tamstorf, J. Teran, and E. Sifakis, *Computing the Singular Value Decomposition of 3 x 3 matrices with minimal branching and elementary floating point operations*, University of Wisconsin Madison, (2011).

[62] L. Michael and N. Nikiforakis, *A hybrid formulation for the numerical simulation of condensed phase explosives*, Journal of Computational Physics, 316 (2016), pp. 193–217.

[63] L. Michael and N. Nikiforakis, *Coupling of elastoplastic solid models with condensed phase explosives formulations*, (submitted), (2016).

[64] C. Michler, S. J. Hulshoff, E. H. van Brummelen, and R. de Borst, *A monolithic approach to fluid structure interaction*, Computers & Fluids, 33 (2004), pp. 839–848.

[65] G. H. Miller, *An iterative Riemann solver for systems of hyperbolic conservation laws, with application to hyperelastic solid mechanics*, Journal of Computational Physics, 193 (2004), pp. 198–225.

[66] M. Morduchow and P. A. Libby, *On a Complete Solution of the One Dimensional Flow Equations of a Viscous, Heat Conducting, Compressible Gas*, tech. rep., Polytechnic Institute of Brooklyn, 1949.

[67] S. Osher and R. Fedkiw, *Level Set Methods and Dynamic Implicit Surfaces*, Springer, 2002.

[68] I. Peshkov and E. Romenski, *A hyperbolic model for viscous Newtonian flows*, Continuum Mechanics & Thermodynamics, 28 (2016), pp. 85–104.

[69] F. D. Pin, S. Idelsohn, E. Onate, and R. Aubry, *The ALE/Lagrangian Particle Finite Element Method: A new approach to computation of free surface flows and fluid object interactions*, Computers & Fluids, 36 (2007), pp. 27–38.

[70] T. Ren, J. Hu, T. Xiong, and J. M. Qiu, *Runge Kutta central discontinuous Galerkin BGK method for the Navier Stokes equations*, Journal of Computational Physics, 274 (2014), pp. 592–610.

[71] E. Romenski, D. Drikakis, and E. Toro, *Conservative models and numerical methods for compressible two phase flow*, Journal of Scientific Computing, 42 (2010), pp. 68–95.

[72] E. Romenski, A. D. Resnyansky, and E. F. Toro, *Conservative Hyperbolic Formulation for Compressible Two Phase Flow with Different Phase Pressures and Temperatures*, Quarterly of Applied Mathematics, 65 (2007), pp. 259–279.

[73] E. I. Romenski, *Hyperbolic Equations of Maxwell's Nonlinear Model of Elastoplastic Heat Conducting Media*, Sibirskii Matematicheskii Zhurnal, 30 (1988), pp. 135–159.

[74] R. Rossi and E. Oñate, *Analysis of some partitioned algorithms for fluid structure interaction*, Engineering Computations, 27 (2010), pp. 20–56.

[75] P. B. Ryzhakov, R. Rossi, S. R. Idelsohn, and E. Onate, *A monolithic Lagrangian approach for fluid structure interaction problems*, Computational Mechanics, 46 (2010), pp. 883–899.

[76] S. K. Sambasivan and H. S. UdayKumar, *Ghost Fluid Method for Strong Shock Interactions Part 1: Fluid Fluid Interfaces*, AIAA Journal, 47 (2009), pp. 2907–2922.

[77] S. Schoch, K. Nordin Bates, and N. Nikiforakis, *An Eulerian algorithm for coupled simulations of elastoplastic solids and condensed phase explosives*, Journal of Computational Physics, 252 (2013), pp. 163–194.

[78] M. Short, *On the Critical Conditions for the Initiation of a Detonation in a Nonuniformly Perturbed Reactive Fluid*, SIAM Journal on Applied Mathematics, 57 (1997), pp. 1242–1280.

[79] G. A. Sod, *A survey of several finite difference methods for systems of nonlinear hyperbolic conservation laws*, Journal of Computational Physics, 27 (1978), pp. 1–31.

[80] K. Sverdrup, *Numerical Solutions of the Multidimensional HPR Equations using Finite Volume Methods with Splitting Schemes*, Master's Thesis, University of Cambridge, (2016).

[81] H. Terashima and G. Tryggvason, *A front tracking / ghost fluid method for fluid interface in compressible flow*, Journal of Computational Physics, 228 (2009), pp. 4012–4037.

[82] E. F. Toro, *Riemann Solvers and Numerical Methods for Fluid Dynamics: A Practical Introduction*, Springer, 2009.

[83] J. von Neumann, *Theory of Detonation Waves*, tech. rep., Institute for Advanced Study, 1942.

[84] S. P. Wang, M. H. Anderson, J. G. Oakley, M. L. Corradini, and R. Bonazza, *A thermodynamically consistent and fully conservative treatment of contact discontinuities for compressible multicomponent flows*, Journal of Computational Physics, 195 (2004), pp. 528–559.

[85] Y. B. Zeldovich, *On the Theory of the Propagation of Detonation in Gaseous Systems*, Journal of Experimental & Theoretical Physics, 10 (1940), pp. 542–568.

6 Appendix

6.1 Appendix

The following quantities are defined for brevity's sake:

$$\Psi_{ij} = \rho v_i v_j - \sigma_{ij} \tag{162a}$$

$$\Phi_{ij}^k = \rho v_k \psi_{ij} - v_m \frac{\partial \sigma_{mk}}{\partial A_{ij}} \tag{162b}$$

$$\Omega_i = v_i \left(E - E_1 \right) - \frac{\sigma_{im} v_m + q_i}{\rho} \tag{162c}$$

$$\Gamma = \gamma - 1 \tag{162d}$$

$$\Upsilon = \Gamma \left(\|\boldsymbol{v}\|^2 + \alpha^2 \|\boldsymbol{J}\|^2 + E_1 - E \right) \tag{162e}$$

Take the following ordering of primitive variables:

$$\boldsymbol{P} = \left(\begin{array}{cccccccccccccccc} \rho & p & A_{11} & A_{21} & A_{31} & A_{12} & A_{22} & A_{32} & A_{13} & A_{23} & A_{33} & v_1 & v_2 & v_3 & J_1 & J_2 & J_3 \end{array} \right)^T \quad (163)$$

The GPR system can be written in the following form, where the components of $\boldsymbol{M}$ and $\boldsymbol{S_p}$ are given on the following pages:

$$\frac{\partial \boldsymbol{P}}{\partial t} + \boldsymbol{M} \cdot \nabla \boldsymbol{P} = \boldsymbol{S_p} \quad (164)$$

6.2   Jacobian of Distortion ODEs

The Jacobian of the source function is used to speed up numerical integration of the ODE. It is derived thus:

$$\frac{\partial \operatorname{dev}(G)_{ij}}{\partial A_{mn}} = \delta_{in} A_{mj} + \delta_{jn} A_{mi} - \frac{2}{3} \delta_{ij} A_{mn} \quad (165)$$

Thus:

$$
\begin{aligned}
\frac{\partial \left(A \operatorname{dev}(G) \right)_{ij}}{\partial A_{mn}} &= \frac{\partial A_{it}}{\partial A_{mn}} \operatorname{dev}(G)_{tj} + A_{it} \frac{\partial \operatorname{dev}(G)_{tj}}{\partial A_{mn}} \quad (166) \\
&= \delta_{im}\delta_{tn} \left(A_{kt} A_{kj} - \frac{1}{3} A_{kl} A_{kl} \delta_{tj} \right) + A_{it} \left(\delta_{tn} A_{mj} + \delta_{jn} A_{mt} - \frac{2}{3} \delta_{tj} A_{mn} \right) \\
&= \delta_{im} A_{kn} A_{kj} - \frac{1}{3} \delta_{im} \delta_{jn} A_{kl} A_{kl} + A_{in} A_{mj} + \delta_{jn} A_{ik} A_{mk} - \frac{2}{3} A_{ij} A_{mn}
\end{aligned}
$$

Thus:

$$
\begin{aligned}
J_A &\equiv \frac{-3}{\tau_1} \frac{\partial \left(\det(A)^{\frac{5}{3}} A \operatorname{dev}(G) \right)_{ij}}{\partial A_{mn}} \quad (167) \\
&= \frac{-3}{\tau_1} \det(A)^{\frac{5}{3}} \left(\frac{5}{3} \left(A \operatorname{dev}(G) \right)_{ij} A_{mn}^{-T} + A_{in} A_{mj} + \delta_{jn} G'_{im} + \delta_{im} G_{jn} - \frac{1}{3} \delta_{im} \delta_{jn} A_{kl} A_{kl} - \frac{2}{3} A_{ij} A_{mn} \right) \\
&= \frac{1}{\tau_1} \det(A)^{\frac{5}{3}} \left(-5 \left(A \operatorname{dev}(G) \right) \otimes A^{-T} + 2 A \otimes A - 3 \left(A \otimes A \right)^{1,3} + \|A\|_F^2 \left(I \otimes I \right)^{2,3} - 3 \left(G' \otimes I + I \otimes G \right)^{2,3} \right)
\end{aligned}
$$

where $G' = A A^T$ and $X^{a,b}$ refers to tensor X with indices a, b transposed.

$$
M_1 =
\begin{pmatrix}
v_1 & 0 & 0 & 0 & 0 & 0 & 0 & 0 & 0 & 0 & 0 & \rho & 0 & 0 & 0 & 0 & 0 \\[4pt]
0 & v_1 & 0 & 0 & 0 & 0 & 0 & 0 & 0 & 0 & 0 & \gamma p & 0 & 0 & \Gamma\alpha^2 T & 0 & 0 \\[4pt]
0 & 0 & v_1 & 0 & 0 & 0 & 0 & 0 & 0 & 0 & 0 & A_{11} & A_{12} & A_{13} & 0 & 0 & 0 \\[4pt]
0 & 0 & 0 & v_1 & 0 & 0 & 0 & 0 & 0 & 0 & 0 & A_{21} & A_{22} & A_{23} & 0 & 0 & 0 \\[4pt]
0 & 0 & 0 & 0 & v_1 & 0 & 0 & 0 & 0 & 0 & 0 & A_{31} & A_{32} & A_{33} & 0 & 0 & 0 \\[4pt]
0 & 0 & 0 & 0 & 0 & v_1 & 0 & 0 & 0 & 0 & 0 & 0 & 0 & 0 & 0 & 0 & 0 \\[4pt]
0 & 0 & 0 & 0 & 0 & 0 & v_1 & 0 & 0 & 0 & 0 & 0 & 0 & 0 & 0 & 0 & 0 \\[4pt]
0 & 0 & 0 & 0 & 0 & 0 & 0 & v_1 & 0 & 0 & 0 & 0 & 0 & 0 & 0 & 0 & 0 \\[4pt]
0 & 0 & 0 & 0 & 0 & 0 & 0 & 0 & v_1 & 0 & 0 & 0 & 0 & 0 & 0 & 0 & 0 \\[4pt]
0 & 0 & 0 & 0 & 0 & 0 & 0 & 0 & 0 & v_1 & 0 & 0 & 0 & 0 & 0 & 0 & 0 \\[4pt]
0 & 0 & 0 & 0 & 0 & 0 & 0 & 0 & 0 & 0 & v_1 & 0 & 0 & 0 & 0 & 0 & 0 \\[4pt]
-\dfrac{\sigma_{11}}{\rho^2} & \dfrac{1}{\rho} & -\dfrac{1}{\rho}\dfrac{\partial\sigma_{11}}{\partial A_{11}} & -\dfrac{1}{\rho}\dfrac{\partial\sigma_{11}}{\partial A_{21}} & -\dfrac{1}{\rho}\dfrac{\partial\sigma_{11}}{\partial A_{31}} & -\dfrac{1}{\rho}\dfrac{\partial\sigma_{11}}{\partial A_{12}} & -\dfrac{1}{\rho}\dfrac{\partial\sigma_{11}}{\partial A_{22}} & -\dfrac{1}{\rho}\dfrac{\partial\sigma_{11}}{\partial A_{32}} & -\dfrac{1}{\rho}\dfrac{\partial\sigma_{11}}{\partial A_{13}} & -\dfrac{1}{\rho}\dfrac{\partial\sigma_{11}}{\partial A_{23}} & -\dfrac{1}{\rho}\dfrac{\partial\sigma_{11}}{\partial A_{33}} & v_1 & 0 & 0 & 0 & 0 & 0 \\[8pt]
-\dfrac{\sigma_{21}}{\rho^2} & 0 & -\dfrac{1}{\rho}\dfrac{\partial\sigma_{21}}{\partial A_{11}} & -\dfrac{1}{\rho}\dfrac{\partial\sigma_{21}}{\partial A_{21}} & -\dfrac{1}{\rho}\dfrac{\partial\sigma_{21}}{\partial A_{31}} & -\dfrac{1}{\rho}\dfrac{\partial\sigma_{21}}{\partial A_{12}} & -\dfrac{1}{\rho}\dfrac{\partial\sigma_{21}}{\partial A_{22}} & -\dfrac{1}{\rho}\dfrac{\partial\sigma_{21}}{\partial A_{32}} & -\dfrac{1}{\rho}\dfrac{\partial\sigma_{21}}{\partial A_{13}} & -\dfrac{1}{\rho}\dfrac{\partial\sigma_{21}}{\partial A_{23}} & -\dfrac{1}{\rho}\dfrac{\partial\sigma_{21}}{\partial A_{33}} & 0 & v_1 & 0 & 0 & 0 & 0 \\[8pt]
-\dfrac{\sigma_{31}}{\rho^2} & 0 & -\dfrac{1}{\rho}\dfrac{\partial\sigma_{31}}{\partial A_{11}} & -\dfrac{1}{\rho}\dfrac{\partial\sigma_{31}}{\partial A_{21}} & -\dfrac{1}{\rho}\dfrac{\partial\sigma_{31}}{\partial A_{31}} & -\dfrac{1}{\rho}\dfrac{\partial\sigma_{31}}{\partial A_{12}} & -\dfrac{1}{\rho}\dfrac{\partial\sigma_{31}}{\partial A_{22}} & -\dfrac{1}{\rho}\dfrac{\partial\sigma_{31}}{\partial A_{32}} & -\dfrac{1}{\rho}\dfrac{\partial\sigma_{31}}{\partial A_{13}} & -\dfrac{1}{\rho}\dfrac{\partial\sigma_{31}}{\partial A_{23}} & -\dfrac{1}{\rho}\dfrac{\partial\sigma_{31}}{\partial A_{33}} & 0 & 0 & v_1 & 0 & 0 & 0 \\[8pt]
-\dfrac{T}{\rho^2} & \dfrac{T}{\rho(p+p_\infty)} & 0 & 0 & 0 & 0 & 0 & 0 & 0 & 0 & 0 & 0 & 0 & 0 & v_1 & 0 & 0 \\[4pt]
0 & 0 & 0 & 0 & 0 & 0 & 0 & 0 & 0 & 0 & 0 & 0 & 0 & 0 & 0 & v_1 & 0 \\[4pt]
0 & 0 & 0 & 0 & 0 & 0 & 0 & 0 & 0 & 0 & 0 & 0 & 0 & 0 & 0 & 0 & v_1
\end{pmatrix}
$$

$$
M_2 =
\begin{pmatrix}
v_2 & 0 & 0 & 0 & 0 & 0 & 0 & 0 & 0 & 0 & 0 & 0 & \rho & 0 & 0 & 0 \\[4pt]
0 & v_2 & 0 & 0 & 0 & 0 & 0 & 0 & 0 & 0 & 0 & 0 & \gamma p & 0 & 0 & \Gamma\alpha^2 T \\[4pt]
0 & 0 & v_2 & 0 & 0 & 0 & 0 & 0 & 0 & 0 & 0 & 0 & 0 & 0 & 0 & 0 \\[4pt]
0 & 0 & 0 & v_2 & 0 & 0 & 0 & 0 & 0 & 0 & 0 & 0 & 0 & 0 & 0 & 0 \\[4pt]
0 & 0 & 0 & 0 & v_2 & 0 & 0 & 0 & 0 & 0 & 0 & 0 & 0 & 0 & 0 & 0 \\[4pt]
0 & 0 & 0 & 0 & 0 & v_2 & 0 & 0 & 0 & 0 & 0 & A_{11} & A_{12} & A_{13} & 0 & 0 \\[4pt]
0 & 0 & 0 & 0 & 0 & 0 & v_2 & 0 & 0 & 0 & 0 & A_{21} & A_{22} & A_{23} & 0 & 0 \\[4pt]
0 & 0 & 0 & 0 & 0 & 0 & 0 & v_2 & 0 & 0 & 0 & A_{31} & A_{32} & A_{33} & 0 & 0 \\[4pt]
0 & 0 & 0 & 0 & 0 & 0 & 0 & 0 & v_2 & 0 & 0 & 0 & 0 & 0 & 0 & 0 \\[4pt]
0 & 0 & 0 & 0 & 0 & 0 & 0 & 0 & 0 & v_2 & 0 & 0 & 0 & 0 & 0 & 0 \\[4pt]
0 & 0 & 0 & 0 & 0 & 0 & 0 & 0 & 0 & 0 & v_2 & 0 & 0 & 0 & 0 & 0 \\[6pt]
-\dfrac{\sigma_{12}}{\rho^2} & 0 & -\dfrac{1}{\rho}\dfrac{\partial\sigma_{12}}{\partial A_{11}} & -\dfrac{1}{\rho}\dfrac{\partial\sigma_{12}}{\partial A_{21}} & -\dfrac{1}{\rho}\dfrac{\partial\sigma_{12}}{\partial A_{31}} & -\dfrac{1}{\rho}\dfrac{\partial\sigma_{12}}{\partial A_{12}} & -\dfrac{1}{\rho}\dfrac{\partial\sigma_{12}}{\partial A_{22}} & -\dfrac{1}{\rho}\dfrac{\partial\sigma_{12}}{\partial A_{32}} & -\dfrac{1}{\rho}\dfrac{\partial\sigma_{12}}{\partial A_{13}} & -\dfrac{1}{\rho}\dfrac{\partial\sigma_{12}}{\partial A_{23}} & -\dfrac{1}{\rho}\dfrac{\partial\sigma_{12}}{\partial A_{33}} & v_2 & 0 & 0 & 0 & 0 \\[6pt]
-\dfrac{\sigma_{22}}{\rho^2} & \dfrac{1}{\rho} & -\dfrac{1}{\rho}\dfrac{\partial\sigma_{22}}{\partial A_{11}} & -\dfrac{1}{\rho}\dfrac{\partial\sigma_{22}}{\partial A_{21}} & -\dfrac{1}{\rho}\dfrac{\partial\sigma_{22}}{\partial A_{31}} & -\dfrac{1}{\rho}\dfrac{\partial\sigma_{22}}{\partial A_{12}} & -\dfrac{1}{\rho}\dfrac{\partial\sigma_{22}}{\partial A_{22}} & -\dfrac{1}{\rho}\dfrac{\partial\sigma_{22}}{\partial A_{32}} & -\dfrac{1}{\rho}\dfrac{\partial\sigma_{22}}{\partial A_{13}} & -\dfrac{1}{\rho}\dfrac{\partial\sigma_{22}}{\partial A_{23}} & -\dfrac{1}{\rho}\dfrac{\partial\sigma_{22}}{\partial A_{33}} & 0 & v_2 & 0 & 0 & 0 \\[6pt]
-\dfrac{\sigma_{32}}{\rho^2} & 0 & -\dfrac{1}{\rho}\dfrac{\partial\sigma_{32}}{\partial A_{11}} & -\dfrac{1}{\rho}\dfrac{\partial\sigma_{32}}{\partial A_{21}} & -\dfrac{1}{\rho}\dfrac{\partial\sigma_{32}}{\partial A_{31}} & -\dfrac{1}{\rho}\dfrac{\partial\sigma_{32}}{\partial A_{12}} & -\dfrac{1}{\rho}\dfrac{\partial\sigma_{32}}{\partial A_{22}} & -\dfrac{1}{\rho}\dfrac{\partial\sigma_{32}}{\partial A_{32}} & -\dfrac{1}{\rho}\dfrac{\partial\sigma_{32}}{\partial A_{13}} & -\dfrac{1}{\rho}\dfrac{\partial\sigma_{32}}{\partial A_{23}} & -\dfrac{1}{\rho}\dfrac{\partial\sigma_{32}}{\partial A_{33}} & 0 & 0 & v_2 & 0 & 0 \\[6pt]
-\dfrac{T}{\rho^2} & \dfrac{T}{\rho(p+p_\infty)} & 0 & 0 & 0 & 0 & 0 & 0 & 0 & 0 & 0 & 0 & 0 & 0 & v_2 & 0 \\[6pt]
0 & 0 & 0 & 0 & 0 & 0 & 0 & 0 & 0 & 0 & 0 & 0 & 0 & 0 & 0 & v_2
\end{pmatrix}
$$

$$M_3 =$$

$$
\begin{pmatrix}
v_3 & 0 & 0 & 0 & 0 & 0 & 0 & 0 & 0 & 0 & 0 & 0 & 0 & \rho & 0 & 0 & 0 & 0 \\[4pt]
0 & v_3 & 0 & 0 & 0 & 0 & 0 & 0 & 0 & 0 & 0 & 0 & 0 & \gamma p & 0 & 0 & 0 & \Gamma\alpha^2 T \\[4pt]
0 & 0 & v_3 & 0 & 0 & 0 & 0 & 0 & 0 & 0 & 0 & A_{11} & 0 & 0 & 0 & 0 & 0 & 0 \\[4pt]
0 & 0 & 0 & v_3 & 0 & 0 & 0 & 0 & 0 & 0 & 0 & A_{21} & 0 & 0 & 0 & 0 & 0 & 0 \\[4pt]
0 & 0 & 0 & 0 & v_3 & 0 & 0 & 0 & 0 & 0 & 0 & A_{31} & 0 & 0 & 0 & 0 & 0 & 0 \\[4pt]
0 & 0 & 0 & 0 & 0 & v_3 & 0 & 0 & 0 & 0 & 0 & 0 & A_{12} & 0 & 0 & 0 & 0 & 0 \\[4pt]
0 & 0 & 0 & 0 & 0 & 0 & v_3 & 0 & 0 & 0 & 0 & 0 & A_{22} & 0 & 0 & 0 & 0 & 0 \\[4pt]
0 & 0 & 0 & 0 & 0 & 0 & 0 & v_3 & 0 & 0 & 0 & 0 & A_{32} & 0 & 0 & 0 & 0 & 0 \\[4pt]
0 & 0 & 0 & 0 & 0 & 0 & 0 & 0 & v_3 & 0 & 0 & 0 & 0 & A_{13} & 0 & 0 & 0 & 0 \\[4pt]
0 & 0 & 0 & 0 & 0 & 0 & 0 & 0 & 0 & v_3 & 0 & 0 & 0 & A_{23} & 0 & 0 & 0 & 0 \\[4pt]
0 & 0 & 0 & 0 & 0 & 0 & 0 & 0 & 0 & 0 & v_3 & 0 & 0 & A_{33} & 0 & 0 & 0 & 0 \\[4pt]
-\dfrac{\sigma_{13}}{\rho^2} & 0 & -\dfrac{1}{\rho}\dfrac{\partial\sigma_{13}}{\partial A_{11}} & -\dfrac{1}{\rho}\dfrac{\partial\sigma_{13}}{\partial A_{21}} & -\dfrac{1}{\rho}\dfrac{\partial\sigma_{13}}{\partial A_{31}} & -\dfrac{1}{\rho}\dfrac{\partial\sigma_{13}}{\partial A_{12}} & -\dfrac{1}{\rho}\dfrac{\partial\sigma_{13}}{\partial A_{22}} & -\dfrac{1}{\rho}\dfrac{\partial\sigma_{13}}{\partial A_{32}} & -\dfrac{1}{\rho}\dfrac{\partial\sigma_{13}}{\partial A_{13}} & -\dfrac{1}{\rho}\dfrac{\partial\sigma_{13}}{\partial A_{23}} & -\dfrac{1}{\rho}\dfrac{\partial\sigma_{13}}{\partial A_{33}} & v_3 & 0 & 0 & 0 & 0 & 0 & 0 \\[10pt]
-\dfrac{\sigma_{23}}{\rho^2} & 0 & -\dfrac{1}{\rho}\dfrac{\partial\sigma_{23}}{\partial A_{11}} & -\dfrac{1}{\rho}\dfrac{\partial\sigma_{23}}{\partial A_{21}} & -\dfrac{1}{\rho}\dfrac{\partial\sigma_{23}}{\partial A_{31}} & -\dfrac{1}{\rho}\dfrac{\partial\sigma_{23}}{\partial A_{12}} & -\dfrac{1}{\rho}\dfrac{\partial\sigma_{23}}{\partial A_{22}} & -\dfrac{1}{\rho}\dfrac{\partial\sigma_{23}}{\partial A_{32}} & -\dfrac{1}{\rho}\dfrac{\partial\sigma_{23}}{\partial A_{13}} & -\dfrac{1}{\rho}\dfrac{\partial\sigma_{23}}{\partial A_{23}} & -\dfrac{1}{\rho}\dfrac{\partial\sigma_{23}}{\partial A_{33}} & 0 & v_3 & 0 & 0 & 0 & 0 & 0 \\[10pt]
-\dfrac{\sigma_{33}}{\rho^2} & \dfrac{1}{\rho} & -\dfrac{1}{\rho}\dfrac{\partial\sigma_{33}}{\partial A_{11}} & -\dfrac{1}{\rho}\dfrac{\partial\sigma_{33}}{\partial A_{21}} & -\dfrac{1}{\rho}\dfrac{\partial\sigma_{33}}{\partial A_{31}} & -\dfrac{1}{\rho}\dfrac{\partial\sigma_{33}}{\partial A_{12}} & -\dfrac{1}{\rho}\dfrac{\partial\sigma_{33}}{\partial A_{22}} & -\dfrac{1}{\rho}\dfrac{\partial\sigma_{33}}{\partial A_{32}} & -\dfrac{1}{\rho}\dfrac{\partial\sigma_{33}}{\partial A_{13}} & -\dfrac{1}{\rho}\dfrac{\partial\sigma_{33}}{\partial A_{23}} & -\dfrac{1}{\rho}\dfrac{\partial\sigma_{33}}{\partial A_{33}} & 0 & 0 & v_3 & 0 & 0 & 0 & 0 \\[10pt]
0 & 0 & 0 & 0 & 0 & 0 & 0 & 0 & 0 & 0 & 0 & 0 & 0 & 0 & v_3 & 0 & 0 & 0 \\[4pt]
0 & 0 & 0 & 0 & 0 & 0 & 0 & 0 & 0 & 0 & 0 & 0 & 0 & 0 & 0 & v_3 & 0 & 0 \\[4pt]
0 & 0 & 0 & 0 & 0 & 0 & 0 & 0 & 0 & 0 & 0 & 0 & 0 & 0 & 0 & 0 & v_3 & 0 \\[4pt]
-\dfrac{T}{\rho^2} & \dfrac{T}{\rho(p+p_\infty)} & 0 & 0 & 0 & 0 & 0 & 0 & 0 & 0 & 0 & 0 & 0 & 0 & 0 & 0 & 0 & v_3
\end{pmatrix}
$$

$$
\boldsymbol{S_p} = \frac{1}{\theta_1\left(\tau_1\right)}
\begin{pmatrix}
0 \\
\left(\gamma-1\right)\rho\,\|\psi\|_F^2 \\
0 \\
0 \\
0 \\
-\psi_{11} \\
-\psi_{21} \\
-\psi_{31} \\
-\psi_{12} \\
-\psi_{22} \\
-\psi_{32} \\
-\psi_{13} \\
-\psi_{23} \\
-\psi_{33} \\
0 \\
0 \\
0
\end{pmatrix}
+ \frac{1}{\theta_2\left(\tau_2\right)}
\begin{pmatrix}
0 \\
\left(\gamma-1\right)\rho\,\|\boldsymbol{H}\|^2 \\
0 \\
0 \\
0 \\
0 \\
0 \\
0 \\
0 \\
0 \\
0 \\
0 \\
0 \\
0 \\
-H_1 \\
-H_2 \\
-H_3
\end{pmatrix}
$$

6.3   Jacobian of Thermal Impulse ODEs

As demonstrated in 4.3.2, we have:

$$\frac{dJ_i}{dt} = \frac{J_i}{2}\left(-a + b\left(J_1^2 + J_2^2 + J_3^2\right)\right) \tag{168}$$

where

$$a = \frac{2\rho_0}{\tau_2 T_0 \rho c_v}\left(E - E_{2A}\left(A\right) - E_3\left(\boldsymbol{v}\right)\right) \tag{169a}$$

$$b = \frac{\rho_0 \alpha^2}{\tau_2 T_0 \rho c_v} \tag{169b}$$

Thus, the Jacobian of the thermal impulse ODEs is:

$$\begin{pmatrix} \frac{b}{2}\left(3J_1^2 + J_2^2 + J_3^2\right) - \frac{a}{2} & bJ_1J_2 & bJ_1J_3 \\ bJ_1J_2 & \frac{b}{2}\left(J_1^2 + 3J_2^2 + J_3^2\right) - \frac{a}{2} & bJ_2J_3 \\ bJ_1J_3 & bJ_2J_3 & \frac{b}{2}\left(J_1^2 + J_2^2 + 3J_3^2\right) - \frac{a}{2} \end{pmatrix} \tag{170}$$